



Thesis by publication for the degree
Doctor of Natural Sciences (Dr. rer. nat.)

***Towards understanding the signal
formation in polar snow, firn and
ice using X-ray computed
tomography***

CHRISTOPH FLORIAN SCHALLER

Submitted: 19 December 2017

Colloquium: 07 February 2018

Supervisor: Prof. Dr. Olaf Eisen, University of Bremen

Second assessor: Prof. Dr. Frank Wilhelms, University of Göttingen

Name / Name: Christoph Florian Schaller Date / Date: 18.12.2017

Anschrift / Address: Rheinstr. 52, 27570 Bremerhaven

Erklärung / Affirmation

Ich versichere, dass / I affirm that

1. die Dissertation ohne unerlaubte fremde Hilfe angefertigt wurde /
I wrote the present thesis independently and without illicit assistance from third parties,
2. keine anderen als die von mir angegebenen Quellen und Hilfsmittel benutzt wurden und /
I used no sources other than those indicated nor aids other than those permissible,
3. die den benutzten Werken wörtlich oder inhaltlich entnommenen Stellen als solche kenntlich gemacht wurden. /
I appropriately referenced any text or content from other sources

Bremerhaven, den / on this day 18.12.2017

Christoph Schaller

(Unterschrift / Signature)

Zusammenfassung

Eisbohrkerne aus den Polargebieten stellen ein einzigartiges Archiv des Klimasystems der Erde dar. Allerdings kann die Repräsentativität dieser Eiskerne aufgrund der komplexen logistischen Rahmenbedingungen nicht auf direktem Wege untersucht werden. Möglich ist allerdings die Analyse der räumlichen Variabilität in polarem Schnee und Firn. In Kombination mit einem verbesserten Verständnis der Bildung paläoklimatischer Signale in Eiskernen mit zunehmender Tiefe, können diese Ergebnisse zu einer Abschätzung der Repräsentativität herangezogen werden. In der vorliegenden Arbeit werden röntgentomographische Messungen genutzt um Stratigraphie und Mikrostruktur von polarem Schnee und Firn zerstörungsfrei zu untersuchen. So werden Beiträge zu beiden Teilgebieten dieses indirekten Ansatzes geliefert.

Neue Methoden zur Beprobung der Schneeeauflage und der Identifikation kohärenter Signale in räumlich verteilten Datensätzen werden vorgestellt. Diese werden angewandt um die räumliche Variabilität auf der lokalen (Schachtstudien in Grönland und der Ostantarktis, bis zu 100 m Entfernung) ebenso wie der regionalen Skala (Traverse durch Nordgrönland, 450 km) zu untersuchen. Der Algorithmus zur Ähnlichkeitsbestimmung wird anhand zufällig erzeugter Profile mit den statistischen Eigenschaften der Originaldaten validiert. Zweidimensionale Röntgentomographie dient als Indikator für die Schnee- und Firnstratigraphie, die Datierung erfolgt anhand des $\delta^{18}\text{O}$ -Signals.

Die Ergebnisse belegen eine signifikante regionale Komponente der Dichteschichtung, welche über hunderte Kilometer nachweisbar ist. Lokal zeigt sich ein starker richtungsabhängiger Einfluss des Windes mit erhöhter Homogenität entlang der vorherrschenden Windrichtung. Da Dichte ein wichtiger Eingangsparameter für die Fernerkundung und Abschätzungen der Massenbilanz der Oberfläche ist, besteht Bedarf an repräsentativen Profilen und Mittelwerten der Dichte. Ein solches Profil wird für die obersten zwei Meter der Schneeeauflage in Nordgrönland bereitgestellt. Für flächige Signale auf der lokalen Skala (z. B. altimetrische Messungen) werden derartige Abschätzungen durch die richtungsabhängigen Einflüsse auf die Variabilität deutlich erschwert.

Da die Dichteschichtung massiv durch Schmelzen der Schneeoberfläche beeinflusst wird, werden Schmelzlagen aus dem warmen grönländischen Sommer des Jahres 2012 gesondert betrachtet. Die ausgeprägte Heterogenität dieses Schmelzens hat nicht nur großen Einfluss auf die Fernerkundung (da sie als Reflektoren für elektromagnetische Wellen agieren), sondern verkompliziert auch die Interpretation von Schmelzlagen in einzelnen Eiskernen.

Methodische Fortschritte in der dreidimensionalen Computertomographie ermöglichen die Erstellung eines ersten umfassenden Datensatzes direkter Mikrostrukturmessungen im Firn. Drei Eiskerne, die verschiedene Extreme der auftretenden Temperaturen und Akkumulationsraten abdecken, werden für den gesamten Bereich des Lufteinschlusses analysiert. Der zugrundeliegende Einschlussprozess ist ein bestimmender Faktor für den Altersunterschied zwischen eingeschlossener Luft und umliegendem Eis, der bis zu mehreren 1.000 Jahren betragen kann. Die exakte Bestimmung dieses Werts ist daher von besonderer Bedeutung für die Untersuchung von paläoklimatischen Phasenzusammenhängen.

Mit Hilfe des Datensatzes wird nachgewiesen, dass es sich bei der kritischen Porosität des Porenabschlusses um eine klimaunabhängige Konstante handelt. Dieses Erkenntnis wird durch Perkolationsstheorie gestützt. Die Berücksichtigung der Ergebnisse hat nennenswerten Einfluss auf die Datierung der Gasphase – Abweichungen von anderen Klimaproxies reduzieren sich um bis zu mehr als 1.000 Jahre. Ergänzend wird gezeigt, warum vorherige Studien irreführende Resultate lieferten.

Abstract

Polar ice cores act as a unique archive of the Earth's climate system. However, due to logistic constraints, the representativity of these ice-core records cannot be estimated directly. One possible remedy is to analyze the spatial variability in polar snow and firn and combine the results with an improved understanding of the formation of paleoclimatic ice-core signals and their evolution with depth. Here, X-ray computed tomography is applied as a non-destructive method that yields information on stratigraphy and microstructure in polar snow and firn. The results are used to contribute to both subtopics of this indirect approach for estimating representativity.

New methods for sampling the snowpack as well as the detection and alignment of coherent signals in spatially-distributed datasets are presented. They are applied to analyze spatial variability in the snowpack both on the local (trench studies in Greenland and East Antarctica, distances up to 100 m) and the regional scale (450 km traverse through North Greenland). The matching algorithm is validated using randomly generated profiles with the same statistical properties as the original data. Snow and firn density as markers of stratigraphy are determined by two-dimensional radiosopic imaging, the water-isotopic $\delta^{18}\text{O}$ signal is used for age dating.

The results show that regionally a significant share of the stratigraphic density signal persists over hundreds of kilometers. Locally, there is a strong directional influence of the wind with a much larger homogeneity of the snowpack along the main wind direction. As density is an important input parameter for remote sensing and surface-mass-balance estimates, representative profiles or mean values of snow and firn density are required. Such a profile is provided for the upper two meters of the North Greenland snowpack. On the local scale, the estimation of representative densities for certain areas of interest (such as the footprint of an altimeter) is complicated by the directional dependence of the stratigraphic variability.

As the density layering is significantly impacted by melting of the snow surface, melt features dating to the warm Greenlandic summer of 2012 are analyzed in detail. A large heterogeneity of these features is quantified, which does not only affect remote measurements (where ice layers act as reflectors for electromagnetic waves) but also strongly influences the ability to interpret single-core melt records.

Methodological advances in the three-dimensional computed tomography of polar firn allow the creation of a first extensive dataset of direct firn-microstructure measurements. Three ice cores that represent different extremes of the temperature and accumulation ranges are analyzed throughout the lock-in zone, the depth range where pores are sealed from the atmosphere. The fundamental lock-in process is a determining factor for the gas-age-ice-age difference, which can be on the order of several 1,000 years. Thus, accurate estimates of this value are of particular importance for the interpretation of phase relationships between ice and gas records.

The dataset is used to show that the critical porosity of pore enclosure is a climate-independent constant, a finding that is corroborated by percolation theory. Incorporation of this result significantly influences the dating of trace-gas records, reducing mismatches with other climate proxies by up to more than 1,000 years. Furthermore, it is demonstrated why previous measurements yielded misleading results.

Contents

1	List of publications	1
2	Motivation	2
3	Scientific background	4
3.1	X-ray computed tomography	4
3.2	Firn densification and gas enclosure	4
3.3	Density stratigraphy of polar snow and firn	5
3.4	The influence of melting	5
4	The author's main contributions	7
4.1	Methodology	7
4.1.1	Snow sampling	7
4.1.2	2-D radioscopy using the AWI-Ice-CT	7
4.1.3	Wiggle matching	9
4.1.4	3-D firn-microstructure analysis	9
4.2	Results	10
4.2.1	Spatial variability of the snowpack	10
4.2.2	Melt layers	11
4.2.3	Firn microstructure	11
4.3	Implications	11
4.3.1	Signal formation in the snowpack	11
4.3.2	Paleoclimatic interpretations	11
4.3.3	Remote measurements and surface melting	12
5	Outlook	13
5.1	2.5-D – a new AWI-Ice-CT method?	13
5.2	Spatial variability of chemical signals in the snow	14
5.3	Alpine snow versus polar snow	14
5.4	Gas enclosure and firn sintering	15
5.5	Snowpack modeling	15
5.6	Data and code availability	16
	References	17
	Acknowledgments	25
	Appendix	26
	Publication I	26
	Publication II	39
	Publication III	49

1 List of publications

This thesis is based on the following three publications, which can be found in the Appendix in journal format. The author contributions are pointed out using the respective paragraph from each manuscript.

Publication I

Schaller, C. F., Freitag, J., Kipfstuhl, S., Laepple, T., Steen-Larsen, H. C., and Eisen, O.: A representative density profile of the North Greenland snowpack, *The Cryosphere*, 10, 1991–2002, <https://doi.org/10.5194/tc-10-1991-2016>, 2016

Author contributions. SK took the samples and initiated the analysis process. HCSL was involved in the field planning and helped interpret the results with his expertise in the Greenland snowpack. JF originally established the CT method, supervised and evaluated the isotope measurements and regularly discussed preliminary results with the main author. OE helped to relate the results to the literature and provided insights on alternative methods. TL recommended underlining the results with randomly generated data and suggested possible approaches. CS coordinated the CT measurements, evaluated and analyzed the combined data and prepared this manuscript. It was reviewed by all coauthors.

Publication II

Schaller, C. F., Freitag, J., and Eisen, O.: Critical porosity of gas enclosure in polar firn independent of climate, *Climate of the Past*, 13, 1685–1693, <https://doi.org/10.5194/cp-13-1685-2017>, 2017

Author contributions. JF was responsible for the development of the AWI-Ice-CT and pointed out the opportunity for this study to CS. 3-D measurements were carried out by JF for RECAP_S2 and CS for B49 and B53. The segmentation of the 3-D datasets and the evaluation of microstructural parameters were performed by CS, who researched and programmed the necessary algorithms. The results and their implications were discussed and related to the literature by all coauthors. CS prepared the initial manuscript, which was reviewed and improved by all coauthors.

Publication III

Schaller, C. F., Kipfstuhl, S., Steen-Larsen, H. C., Freitag, J., and Eisen, O.: On the influence of polar snowpack stratigraphy on the interpretation of ice-core and altimetry data, *Journal of Geophysical Research: Earth Surface*, under review, 2017

Author contributions. This study was designed by JF, SK, HCSL and CS. Wall sampling was conducted by SK and CS. CS took the snow cores, supervised the CT measurements, evaluated the melt record, densities and AWS data as well as researched and programmed the necessary algorithms. The results were discussed and related to the literature by all coauthors. CS prepared the initial manuscript, which was improved by reviews from all coauthors.

2 Motivation

Climate change is no longer only of interest to scientists and politicians – it has become an omnipresent topic in daily life and the media. In the context of global warming, the prediction of potential consequences (such as a rise in sea level) and their impact on economy, environment and society is of particular importance. The Intergovernmental Panel on Climate Change (IPCC) acts as an expert group to regularly provide policy-makers with assessment reports of the related scientific advances, inter alia presenting possible future scenarios [IPCC, 2014].

Both, the decay of the West Antarctic ice sheet (WAIS) and the Greenland ice sheet (GrIS) were named "tipping points" in the Earth system and may cause sea level rises of up to 5 and 7 m within the next 300 years [Lenton *et al.*, 2008]. Worryingly, only one of the ten warmest years recorded for Greenland since 1961 occurred before 2000 and the extent of surface melting is steadily growing in the recent years [McGrath *et al.*, 2013]. The trend culminated in the extreme summer of 2012 when melt was recorded for 98.6% of the ice sheet's extent [Nghiem *et al.*, 2012]. As also the Arctic sea ice is rapidly declining in extent and thickness [Stroeve *et al.*, 2014], the Arctic climate can no longer be considered to be in a steady state [Bhatt *et al.*, 2014].

While ice dating to the previous warm period, the Eemian interglacial (126,000 to 115,000 years ago), was found at multiple locations in Greenland [e.g. NEEM community members, 2013], the oldest dated ice at the WAIS divide is only as old as 67,800 years [Buizert *et al.*, 2015] and thus originates from the last glacial. In combination with other indicators, such as biological evidence for a trans-Antarctic seaway [Barnes and Hillenbrand, 2010] and sediment samples recovered from underneath the WAIS [Scherer *et al.*, 1998], this suggests a collapse of the (vast majority of the) WAIS during the Eemian interglacial [Steig *et al.*, 2015]. As a consequence, the retreat and mass loss of both ice sheets are carefully monitored [Rignot *et al.*, 2014; Doyle *et al.*, 2015].

In order to interpret present-day observations, accurate reconstruction of the climatic evolution in the past is necessary. Ice cores act as a unique source of paleoclimatic information as the ice and the enclosed air provide various continuous records of past atmospheric conditions [Legrand and Mayewski, 1997]. As a consequence, one of the main goals of the International Partnerships in Ice Core Sciences (IPICS) is the recovery of the "Oldest-Ice" core, providing a climatic record of the last 1.5 million years [Fischer *et al.*, 2013]. In comparison, the oldest existing ice-core, drilled in the scope of the European Project for Ice Coring in Antarctica (EPICA), spans 800,000 years [EPICA community members, 2004].

The storage of paleoclimatic information in polar ice and the enclosed air is largely influenced by the transformation of snow to ice ("firnification"). The transport of air within the porous snow and firn [Colbeck, 1989; Severinghaus *et al.*, 2001] as well as the trapping of gas bubbles [Schwander and Stauffer, 1984] are controlled by firn densification [Herron and Langway, 1980; Freitag *et al.*, 2013a]. In this context, a quantity of particular interest is the age difference between enclosed air and surrounding ice (up to 7,000 years within the existing records [Bender *et al.*, 2006]). Accurate estimates of this value are required to relate the gas- and ice-records [Parrenin *et al.*, 2012]. At the same time, snow and firn stratigraphy strongly affect remote measurements in the polar regions [Rutter *et al.*, 2014; Nilsson *et al.*, 2015] and the conversion of volume to mass is the largest source of uncertainty for altimetry-based estimates of mass changes [Shepherd *et al.*, 2012].

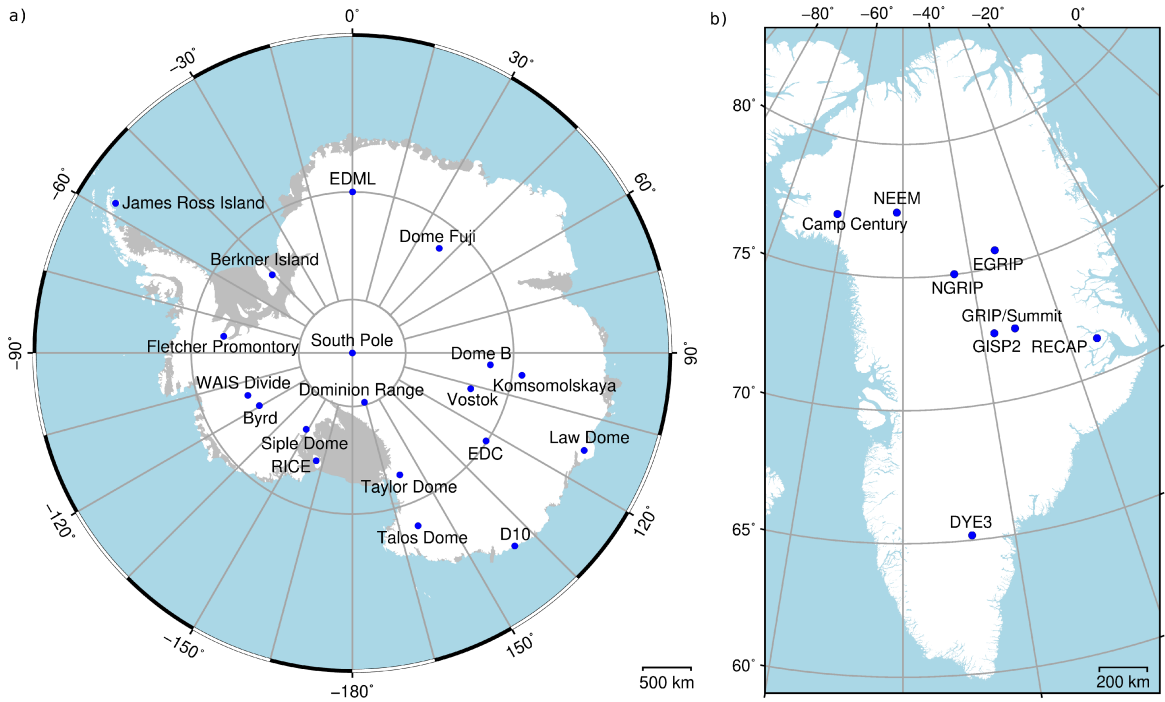


Figure 1: Overview of a) Antarctic and b) Greenlandic ice cores spanning at least 14,000 years, thereby extending to the last glacial. For Antarctica, ice sheets (white) and ice shelves (gray) were distinguished. The map scales were adjusted to a) 80°S and b) 70°N.

Remote-sensing techniques (such as airborne radio-echo sounding) reveal continuous isochronal reflectors within the ice-column over hundreds of kilometers allowing the connection of individual ice cores [Steinhage *et al.*, 2013]. However, tracing of isochrones is often impeded by the influence of ice flow, surface processes (buried dunes or erosion) and subglacial features [Cavitt *et al.*, 2016]. Taking into account the sparsity of existing polar ice cores (see Fig. 1), these techniques are certainly very instrumental in decreasing dating uncertainties and linking ice-core records. Nevertheless, they do not yield information about the actual signal composition in an ice core.

As drilling in the remote polar regions is logistically complex, direct analysis of the representativity of single-core records (for example via ice-core arrays) is not possible. Thus, it remains unclear how large the contributions of local, regional and global signals to a specific ice-core record are [e.g. Muench *et al.*, 2016]. In particular, due to significant differences in the climatic conditions (such as temperature, accumulation rate, altitude, wind, coastal influence, ...) the composition of the depositional signal and thus also the representativity of single-core records do not only depend on the location, but are subject to change over time.

In contrast, the drilling of snow- and firn-core arrays (at certain sites as well as along traverses) is feasible and provides the opportunity to analyze the variability of the resulting records. This information, in combination with an improved understanding of the signal formation in the snowpack and its evolution with depth may allow the estimation of the representativity of ice-core records. To this end, the process of pore enclosure is investigated in detail (Publication II). In addition, signal composition and spatial variability within the snowpack are studied both on the local (Publication I) and the regional scale (Publication III).

3 Scientific background

3.1 X-ray computed tomography

X-ray computed tomography (X-CT) was already used for various glaciological applications [Schnee-*beli and Sokratov*, 2004; *Obbard et al.*, 2009; *Gregory et al.*, 2014]. The AWI-Ice-CT, a computer tomograph in a cold lab at the Alfred Wegener Institute, Helmholtz Center for Polar and Marine Research (AWI) [as first presented in *Freitag et al.*, 2013b], provides unique opportunities for non-destructive X-ray tomographic measurements of 1 m firn- and ice-core segments. For 3-D scans over the full core diameter (up to 10 cm), resolutions down to 15 μm can be achieved. Precisions of this order are necessary for the accurate segmentation of the three-dimensional pore structures in firn and ice (Fig. 2). However, the necessary measurement durations easily exceed 24 hours.

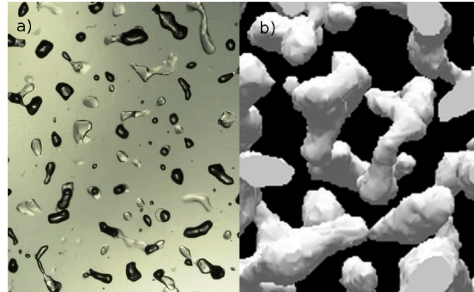


Figure 2: a) Photograph and b) 3-D X-CT image of air enclosures in polar ice.

In contrast, simple 2-D radioscopic images of 1 m segments at a resolution of approximately 100 μm (see Fig. 6b) can be obtained within 15 minutes (including sample preparation, documentation and automated data evaluation). The resulting gray-scale images do not only provide a qualitative impression of the stratigraphy, but also allow the determination of absolute density values. As X-rays are attenuated as they pass through matter, a calibration curve can be fit to the gray values of pure-ice samples of known geometry. The attenuation follows an exponential law (Eq. 1), where I_0 denotes the initial intensity and I the remaining intensity after passing the distance x in a material with absorption coefficient A .

$$I = I_0 e^{-Ax} \quad (1)$$

3.2 Firn densification and gas enclosure

Air is only enclosed in polar ice at a certain depth – the firn–ice transition (50–120 m, depending on the local conditions such as accumulation rate and temperature) [Schwander and Stauffer, 1984]. While near the surface, air in the pore space is still rapidly mixed with the atmosphere (convective zone), air transport is dominated by diffusion further down in the firn column (diffusive zone) [Sowers et al., 1992]. As a result, the enclosed air is always younger than the surrounding ice and has a certain age distribution for each depth. The mean gas-age–ice-age difference (Δage) can be up to 7,000 years under glacial conditions [Bender et al., 2006]. It is of particular importance for the interpretation of phase relationships between paleoclimatic information stored in air and ice.

The entrapment of air is caused by pore closure due to firn densification. In a certain depth range, the lock-in zone, pores are gradually sealed until the respective horizontal layers in the firn become impermeable at a critical porosity [Schwander et al., 1993]. Air-content measurements of deep ice samples suggest a temperature dependence of this value [Martinerie et al., 1992]. Knowledge of the critical porosity is required in

order to estimate the Δ age for past and present conditions using models of firn densification [Herron and Langway, 1980; Freitag et al., 2013a] and firn-air transport [Severinghaus and Battle, 2006; Mitchell et al., 2015].

While such modeled chronologies show good agreement with $\delta^{15}\text{N}$ of N_2 (as a proxy for firn height [Sowers et al., 1992]) for high accumulation sites [Schwander et al., 1997], there is a mismatch of up to 2,000 years in Δ age for the East Antarctic plateau [Bender et al., 2006; Parrenin et al., 2012]. Several possible explanations, such as impurity effects on firn densification [Breant et al., 2017], a larger convective zone under glacial conditions [ruled out by Capron et al., 2013] or inaccuracies in the reconstructions of past temperatures and accumulation rates from the water isotopic composition [Landaï et al., 2006] were discussed in previous studies.

3.3 Density stratigraphy of polar snow and firn

The vertical density variability in the firn was observed to be depth-dependent [Hoerhold et al., 2011]. A seasonal cycle in density develops with depth, which was attributed to the influence of impurity concentrations (particularly Ca^{2+}) on the densification [Hoerhold et al., 2012; Freitag et al., 2013a]. Knowledge of the density stratigraphy is required for remote-sensing applications [e.g. Picard et al., 2013], where it is a large source of uncertainty. For example, the error in retrieved snow height approaches 50% when stratigraphy is neglected [Durand et al., 2011].

The spatial variability of the snowpack is strongly affected by wind-driven redistribution of snow [Libois et al., 2014]. The resulting stratigraphic noise has a particularly strong influence for low accumulation sites, overprinting a seasonal density cycle in the snow [Laepfle et al., 2016]. Polar snow surfaces are often characterized by horizontal undulations as dunes formed along the main wind direction separate individual snow fields [Birnbaum et al., 2010]. Burial of surface features increases the spatial variability of the density stratigraphy [Proksch et al., 2015].

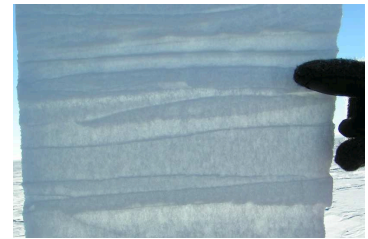


Figure 3: Example of snow stratigraphy at Kohnen station, East Antarctica. Picture courtesy of S. Kipfstuhl.

3.4 The influence of melting

Warm conditions (particularly temperatures above the freezing point) can cause polar snowpacks and ice sheets to heat up until the surface begins to melt. The wetting decreases the albedo of the snow, which triggers a positive feedback [Box et al., 2012]. Depending on the surrounding conditions, the melt water can either run off or be retained or refrozen in the snow and firn below. Different mechanisms for melt water percolating through snow and firn were identified. While homogeneous wetting front migration is dominant in snow and firn near the freezing point, heterogeneous infiltration (often along pipe structures [Pfeffer and Humphrey, 1996]) is prevalent in subfreezing firn [Parry et al., 2007]. Melt experiments in West Antarctica have shown that lateral flow along crust layers and subsequent refreezing of melt water leads to the formation of near-surface melt layers [Das and Alley, 2005]. Several modeling studies have worked towards a quantification of refreezing based on energy balance [Colbeck, 1975; Pfeffer et al., 1990]. However, these models lack verification with in-situ data [as

reviewed by *Reijmer et al.*, 2012]. Furthermore, they are not able to represent the complex three-dimensional percolation patterns observed in the field [e.g. *Humphrey et al.*, 2012]. Regional climate models suggest that approximately 50% of annual melt water is refrozen in Greenland [*Ettema et al.*, 2009].

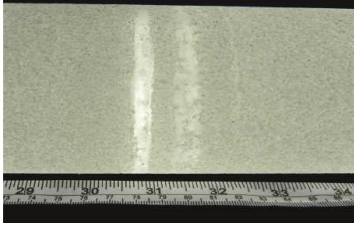


Figure 4: Melt layers in the NEEM ice core [North Greenland, *Orsi et al.*, 2015].

In the summer of 2012, advection of warm air from the south [*Fettweis et al.*, 2013] in combination with low-level liquid clouds [*Bennartz et al.*, 2013] caused the surface of the Greenland ice sheet to melt across 98.6% of its extent [*Nghiem et al.*, 2012]. As such events recur, a frequency record of melt layers (indicating extremely warm summers) is created in the ice [*Langway and Shoji*, 1990; *Alley and Anandakrishnan*, 1995]. These days, remote-sensing allows the detection of surface melting using passive microwave data [*Tedesco*, 2007; *Hall et al.*, 2013]. While for regions of high melt frequency (e.g. South Greenland) satellite-derived melting was linked to shallow-core data [*Rowe et al.*, 1995], the effects of single melt events on snowpack

stratigraphy at cold sites are less well-known. For example, the (presumably) last "extreme" melt event in 1889 is observed in most Greenlandic ice cores [*Clausen et al.*, 1988], but there is no consistent spatial pattern in the existence and volume of the observed melt features.

4 The author's main contributions

4.1 Methodology

4.1.1 Snow sampling

In Publication I, the liner method is introduced as a new and efficient technique for sampling the snowpack. It allows the recovery of high-quality snow cores from the field for advanced lab-based analyses. To preserve the structure of the snowpack (which is usually disturbed by drilling), a carbon-fiber tube of 1 m length with sharp edges (also called "liner", see Fig. 5) is pushed or carefully hammered into the snow until its top is parallel to the surface. A snow pit is excavated next to the liner to cut off the snow at its bottom and retrieve it from the pit wall. The process can be iterated to an arbitrary depth with the main limiting factor being the necessity for excavation. For transport, the tube openings are sealed using matching plastic bags. Occasionally, compaction of the snow in the vertical direction during tube insertion (indicated by a lowered snow surface inside the tube compared to the surroundings) requires removal and parallel reinsertion of the liner.



Figure 5: Sampling a trench wall with the liner technique.

The technique is applicable for regional sampling, e.g. along traverses (Publication I), as well as local studies. In Publication III, a Westa rotary plow mounted in front of a Pistenbully is used for trench excavations to conduct an extensive study of the small-scale spatial variability of the snowpack.

4.1.2 2-D radioscopy using the AWI-Ice-CT

As the structure of the snow cores is best preserved as long as they remain within the carbon-fiber tubes, a sample holder for measuring them in the AWI-Ice-CT was constructed. It consists of Delrin[®] to minimize X-ray scattering. At the bottom, slots for pure-ice cylinders of known diameter were included. Detection of this calibration unit in the resulting 2-D images (see also Fig. 6b) allows the automatic determination of an accurate calibration curve for every single scan. The effect of the carbon-fiber tube being part of the scan is corrected for using empty-tube measurements.

Significant improvements in both quality and time efficiency of the 2-D measurement and analysis process at the AWI-Ice-CT have to be seen as an important contribution of the author. To make his work easily accessible for others, he programmed a cross-platform Graphical User Interface (GUI, >10,000 lines of C/C++ code, see Fig. 6a) that has become the standard software for working with the AWI-Ice-CT. A (non-exhaustive) overview of the included features and improvements is provided in Table 1. In particular, the 2-D Image, density profile and reference bag density are available before the next scan has finished and thus allow immediate validation of each measurement (Fig. 6b).

CT Tool Feature	Previous solution
GUI-accessible database structure for all AWI-Ice-CT measurements	Unspecified folder structure
Printable protocols from within the tool, metafiles assigned to each measurement	Handwritten protocols
2-D Image reconstruction from a stack of raw detector images	ImageJ macro
Automated creation of density profiles for each scan	Semi-automated creation of gray value profiles in ImageJ
Automated calibration for every single measurement (incl. calibration sample detection and curve fitting)	Calibration curve based on scan of pure-ice samples, verified with one ice cube in every measurement
Automated compounding of density profiles (incl. correction for cutting effects at the transitions)	Manual compounding of gray value profiles, collective conversion to density
Semi-automated break correction based on 2-D images	Manual break correction of density profile
Automated tube correction based on empty tube being part of the scan (if feasible, otherwise using a prescribed empty tube profile)	Constant correction factor
Fully parallelized analysis	-
Manageable queue for analysis tasks to be performed	-

Table 1: Feature overview of the AWI CT Tool in comparison with previous approaches.

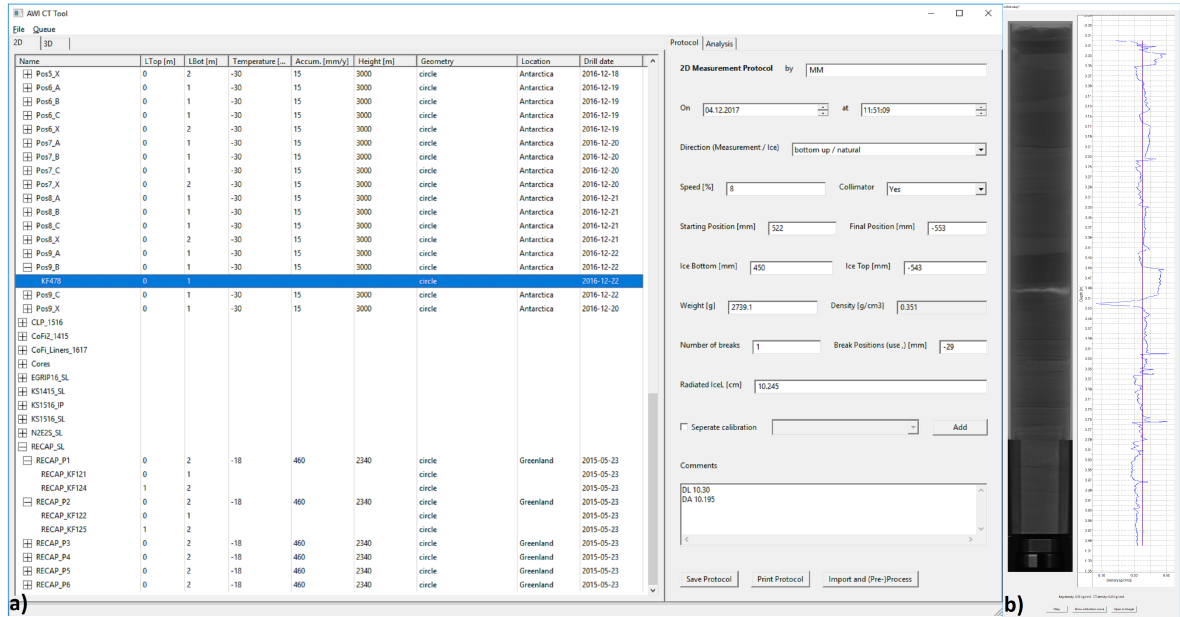


Figure 6: a) Main GUI and b) Validation module (with 2-D image on the left and density profile on the right) of the AWI CT Tool. The calibration unit can be seen at the bottom of the scan.

4.1.3 Wiggle matching

In order to allow for a better comparison between snow- and firn-core profiles from different locations, a method for the detection of coherent signals is required. The main challenge of this analysis is dealing with the stratigraphic variability – the representation of a deposition event (forming a certain "layer" in the snowpack) is highly variable on the regional as well as the local scale. Reasons for that range from surface variability over wind-driven redistribution of snow to different accumulation patterns depending on the atmospheric configuration [Fisher *et al.*, 1985].

Standard approaches (such as maximizing the cross-correlation using a constant offset and a scaling factor) lack the complexity to handle this natural variability. As a consequence, a robust fitting algorithm called Dynamic Time Warping (DTW) was adapted from acoustic signal processing. It allows the alignment of profiles with continuously changing shifts and is described in detail in Publication I. The basic idea is illustrated in Fig. 7. Feature matching will always increase the covariance between records [Haam and Huybers, 2010]. However, surrogate density profiles (with similar statistical properties as the original data) can be used to test the significance of this increase in similarity.



Figure 7: Alignment of two profiles using the DTW algorithm [Criel and Tsiporkova, 2006].

4.1.4 3-D firn-microstructure analysis

The microstructural evolution of firn with depth is expected to strongly influence pore enclosure and thus the paleoclimatic signal in ice-core gas records [Schwander and Stauffer, 1984; Severinghaus *et al.*, 2001]. However, no direct measurements of firn microstructure were available to analyze the underlying processes prior to Publication II.

Distinguishing between closed and open pores in the vicinity of the firn-ice transition requires both a sufficiently high resolution ($<30\ \mu\text{m}$) and a certain sample size (to eliminate the effect of cut pores at the sample surface [Martinerie *et al.*, 1990] and have a statistically representative number of pores left). As standard microCTs and indirect air-content measurements are unable to meet both requirements at the same time, Publication II features the first extensive dataset of direct firn-microstructure measurements throughout the lock-in zone. It was obtained using the AWI-Ice-CT.

As the measurement campaign conducted in the scope of Publication II was unprecedented in size amongst users of the AWI-Ice-CT, the author created a semi-automated chain for data acquisition, processing and archiving. Approximately 400 sections of interest (mostly homogeneous layers) were scanned at the chosen resolution of $25\ \mu\text{m}$ with each measurement consisting of 3,000 radioscopic images (40 GB of raw data). These are used to reconstruct a single three-dimensional gray value image (25 GB), which subsequently has to be segmented into ice and air. As simple approaches (such as using a fixed threshold) are unable to account for small changes in illumination or scattering (e.g. induced by fluctuations in ice-core geometry), a more sophisticated yet efficient segmentation algorithm was adapted for the specific application (detection of the pore space within the firn down to the smallest channels) [Nguyen *et al.*, 2011]. In addition to the plain segmentation, the algorithm also differentiates between closed and open pores and yields multiple parameters of interest such as pore volumes, anisotropies and pore coordination numbers. The scripts for queuing CT measurements (otherwise these have to be started individually), data processing and archival were made available to other users of the AWI-Ice-CT.

4.2 Results

4.2.1 Spatial variability of the snowpack

The liner method was applied both regionally (along a 450 km traverse in North Greenland, Publication I, 2 m profiles) and locally (for one site in Greenland and one site in East Antarctica, Publication III, up to 5 m depth) to learn about the representativity and spatial variability of density stratigraphy in the snowpack. Regionally, tracing of individual layers using the adapted DTW algorithm shows that a significant part of the shared variability persists over hundreds of kilometers. This allows the construction of a representative density profile for the North Greenland snowpack. Dating of the $\delta^{18}\text{O}$ signal enables the deduction of annual accumulation rates and the investigation of interannual variabilities. Finally, the relations of $\delta^{18}\text{O}$ with both density and accumulation rate are analyzed.

Locally, a strong directional influence of the wind on the small-scale variability of the snowpack is quantified. While along the main wind direction a larger homogeneity of the snowpack is measurable for up to 100 m (depending on the site conditions), imprints and burial of surface features dominate the signal in the orthogonal direction. For the vertical variability of the density signal in the top 5 m, the results indicate the evolution of a seasonal cycle with depth.

4.2.2 Melt layers

All analyzed snow cores from Greenland contain signs of melting dating to the summer of 2012 [Nghiem *et al.*, 2012], providing the opportunity to analyze both the regional (Publication I) and local (Publication III) variability of these melt features. Their positioning agrees very well with the DTW-based depth alignment of the traverse snow cores. Locally, a mapping of the melt features along two orthogonal trench walls reveals a considerable spatial variability on the small scale. The existence of distinct melt pipes, penetrating several years of accumulation with no significant horizontal redistribution, indicates deep infiltration of melt (and potentially rain) water in cold Greenlandic plateau firn.

4.2.3 Firn microstructure

In Publication II, firn microstructure throughout the lock-in zone is analyzed for three ice cores representing different extremes of the temperature and accumulation ranges. It is shown that the critical porosity of pore enclosure is a climate-independent constant. This is in agreement with percolation theory as a framework for bubble trapping in porous media. The results are solidified by showing why previous measurements suggested a climatic dependence [Martinerie *et al.*, 1992; Gregory *et al.*, 2014].

4.3 Implications

4.3.1 Signal formation in the snowpack

The successful matching of density and isotope profiles along a 450 km-traverse (Publication I) shows that signal formation over North Greenland seems to be governed by non-local processes. An important factor may be the dominance of a certain atmospheric configuration where air masses (and thus precipitation) move in from the West [Chen *et al.*, 1997]. However, the local component in the density layering (e.g. layer thickness, average density) is not to be underestimated and has to be accounted for to achieve such alignment.

The strong local influence of surface structure and wind-driven redistribution of snow (Publication III) shows the importance of understanding the dominant deposition mechanisms under very low-accumulation conditions, where the height of surface features can easily exceed the annual accumulation. While today such conditions are mainly observed on the East Antarctic plateau, they were far more widespread during glacials [e.g. in Greenland, Schwander *et al.*, 1997].

4.3.2 Paleoclimatic interpretations

For the different sites along the traverse (Publication I), a positive linear relation of annual accumulation rate and average $\delta^{18}\text{O}$ was deduced. However, there seems to be a (presumably temperature-dependent) offset between the years. This may indicate that the simple relations between $\delta^{18}\text{O}$ and accumulation rate and temperature, that are commonly used in paleoclimatic reconstructions from deep ice cores [e.g. Parrenin *et al.*, 2012], may not hold for different climatic conditions, particularly glacials. Deviations of these relations were previously discussed as potential reasons for dating mismatches [Landaïs *et al.*, 2006].

Incorporation of a constant critical porosity (Publication II) in firn-air models can be used to explain more than 1,000 years of the 2,000-year mismatch between modeled Δage and $\delta^{15}\text{N}$ for the Vostok ice core [Bender *et al.*, 2006]. Furthermore, the density layering of the firn in the lock-in zone was identified as an important factor for pore enclosure, in particular for the air content (e.g. due to sealing effects). Layering is known to change with climatic conditions, but is not well-represented in current firn models. Accounting for a stronger layering during glacials [Bendel *et al.*, 2013] may further reduce the remaining mismatch. It will also benefit the understanding of the air-content signal, which seems to be anti-correlated with insolation [Raynaud *et al.*, 2007]. However, the underlying physical mechanisms are unknown [Eicher *et al.*, 2016].

4.3.3 Remote measurements and surface melting

The directional dependence of the stratigraphic variability on the local scale (Publication III) also affects the interpretation of areal signals (e.g. from altimetry). However, the conversion of volume to mass requires representative density profiles, which are the largest source of uncertainty for surface mass balance estimates to date [Shepherd *et al.*, 2012]. A regionally representative profile for the upper two meters of the North Greenland snowpack (including estimates of uncertainty) is provided in Publication I. An improved understanding of spatial density variability and its evolution with depth will further benefit the creation and accuracy of these profiles.

Melt features are a second source of uncertainty for remote-sensing signals – they act as reflectors for electromagnetic waves and increase the amount of volume scattering. However, their large spatial heterogeneity (Publication III) complicates the necessary corrections. Furthermore, it raises strong doubts about the representativity of single ice-core melt records, in particular for sites where melt is scarce. The effect can be reduced by stacking multiple melt records, still individual events may either be overestimated or missed completely.

Refreezing, retention and runoff of the resulting melt water are important factors for mass-balance estimates and the frequency of widespread surface melting is expected to increase in a warming climate [McGrath *et al.*, 2013]. Rainfall was observed on the Greenlandic plateau in the summer of 2012 [Nilsson *et al.*, 2015]. However, rain at higher altitudes of the polar ice sheets is currently not represented in regional climate models or reanalysis data [Tedesco *et al.*, 2013]. Its influence on the surface energy budget is unclear [Fausto *et al.*, 2016].

5 Outlook

5.1 2.5-D – a new AWI-Ice-CT method?

At the moment, 2-D radioscopic measurements with the AWI-Ice-CT are only using about 1% of the available raw information. Single projections are recorded as X-ray source and detector move along the ice core in parallel, with the detector covering an angle of $\pm 7.5^\circ$. However, solely up to six rows in the center of each projection (compared to a total number of 500 rows) are compounded to obtain the final 2-D image. Even though a significant share of the information may be redundant (as basically the same ice is penetrated at a different angle), tilted crusts and transitions between layers are blurred in the horizontal 2-D image while being clearly visible at angles closer to their own orientation. Thus, the raw data may be used to obtain a better impression of the three-dimensional layering in snow and firn. The basic idea was tested for selected core segments (with distinct layering) and is described in Algorithm 1. Under the assumption of homogeneous layers separated by sufficiently sharp transitions, the output of Algorithm 1 can be used to generate images of layered snow and firn cores (e.g. Fig. 8) and improved density profiles with sharper transitions between individual layers.

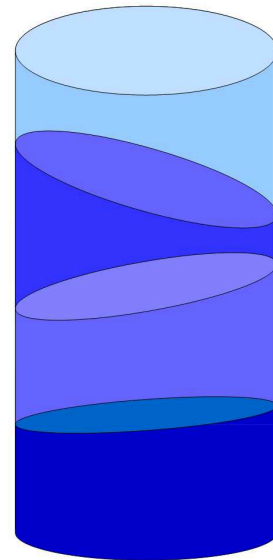


Figure 8: A layered firn core – sample output of the 2.5-D algorithm.

Algorithm 1 2.5-D CT – Basic algorithm

1. Generate 2-D images for a fixed set of penetration angles (e.g. -7.5° to 7.5° at steps of 0.5°).
 2. For each angle:
 - 2.1. Apply an edge detection filter (e.g. Scharr operator).
 - 2.2. Determine the gradients in gray value orthogonal to the detected edge pixels (as a measure of edge "strength").
 - 2.3. Use non-maximum-suppression to uniquely determine the strongest (1 pixel thick) path in the vicinity of each detected transition.
 3. Order all detected edges by strength.
 4. Starting with the strongest edge, add edges that do not intersect with another edge in the set of final edges to the set, until there is no edge with a strength above a certain threshold.
-

5.2 Spatial variability of chemical signals in the snow

While density mainly affects pore enclosure and thus the gas record, the chemical composition in the ice phase is another source of paleoclimatic information [Legrand and Mayewski, 1997]. Measurements of water isotopes (δD , $\delta^{18}\text{O}$ and D_{excess}) and impurity content (Ca^{2+} , K^+ , Mg^{2+} , Na^+ , NH_4^+ , Br^- , Cl^- , F^- , MSA^- , NO_3^- and SO_4^{2-}) were conducted for a subset of the East Antarctic snow cores presented in Publication III in the scope of a bachelor's thesis [Sander, 2017]. The analyzed profiles lie orthogonal to the main wind direction and their similarity in chemical composition seems to oscillate in agreement with the results for the density. However, due to the uneven spacing and a lack of comparison with the variations along other directions, further investigations will be necessary in the scope of ongoing and future projects. As only the chemical analyses require cutting or melting, the majority of cores remained in the carbon-fiber tubes and awaits further processing while stored at -27°C . The chemical composition of one 5 m profile from Greenland was analyzed and linked to snow microstructure in a second bachelor's thesis [Schaidt, 2017]. The author was involved with the supervision of both projects.

5.3 Alpine snow versus polar snow

The author once participated in and twice co-supervised the "Glaciological field trip to the Austrian Alps", organized by POLMAR and the University of Bremen. Amongst others, the students conducted measurements of density and $\delta^{18}\text{O}$ to study their spatial variability while learning methods of state-of-the-art field glaciology.

However, comparison with the results for polar snowpacks is not straightforward as wet snow conditions dominate the study site, Vernagtferner (Fig. 9), in July. Furthermore, the retrieval of non-disturbed snow samples from the field was not feasible, so the sampling was limited to density cutting (weighing a known volume of snow) and retrieving molten snow samples for waterisotopic analysis. There is an ongoing master's project that deals with the detailed evaluation of these data. If comparison with polar studies was desired, sampling the snow and firn in the accumulation zone of a high-altitude site (such as Colle Gnifetti [Wagenbach and Geis, 1989] or Mt. Ortles [Gabrielli et al., 2016]) would be advisable. These sites would also allow for samples to be taken in frozen condition.

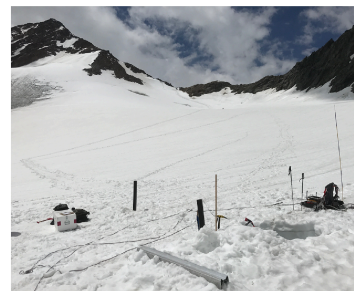


Figure 9: The study site on Vernagtferner in July 2017.

5.4 Gas enclosure and firn sintering

Following up on Publication II, it might be interesting to conduct sintering experiments for (natural as well as artificial) firn samples at different temperatures and pressures (representing different depths and thus accumulation rates). Such controlled conditions in combination with regular X-CT scans would provide a unique opportunity to study the influence of the surrounding conditions on firn sintering and gas enclosure in more detail. This way, both the existence of a universal critical porosity of gas enclosure could be verified and the slope of the relation of closed and total porosity might be parametrized.

A second interesting continuation would be a quantification of closed bubbles and microbubbles in shallow firn. Recent air-content measurements suggest that there already is a significant amount of enclosed air way above the lock-in zone [Kobashi *et al.*, 2015]. In case these bubbles do not open up again due to firn densification, their incorporation in firn air models would significantly broaden the resulting gas-age distribution.

Finally, there is a joint German-French proposal for a new firn model in order to determine the impact of layering on air entrapment and the gas record. A combination of recent advances regarding the influence of firn microstructure (Publication II) and impurities [Freitag *et al.*, 2013a; Breant *et al.*, 2017] on firn densification may not only allow for further reduction of existing mismatches (such as Δage versus $\delta^{15}\text{N}$ [Bender *et al.*, 2006]), but also for a better understanding of signal formation in the gas phase. Here, estimates of the gas-age distribution and the effects of physical properties of the firn on the gas record (e.g. air content and diffusion) will be of particular importance.

5.5 Snowpack modeling

Most candidate sites for the IPICS "Oldest-Ice" core [Fischer *et al.*, 2013] lie far up on the East Antarctic plateau, where accumulation rates are lower than 10 cm snow per year. At the same time the surface roughness can easily exceed 20 cm and there is a strong influence of wind, snow drift and erosion. The formation of signals in the snowpack and their evolution with depth under these conditions is not well-understood. As commonly used snowpack models [e.g. Lehning *et al.*, 1999; Vionnet *et al.*, 2012] originate from alpine applications (such as avalanche forecasting), they are focused on other processes and do not represent all relevant quantities. Instead of adjusting these models to polar conditions, it may be worthwhile to develop and establish a stand-alone snowpack model for polar low-accumulation sites. Existing datasets, in particular traverse and trench studies as conducted within the Coldest Firn (CoFi) project (e.g. Fig. 10), should allow the determination and (empirical) quantification of the dominant processes.

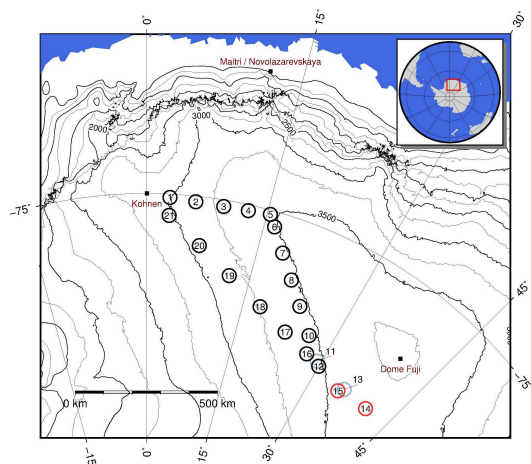


Figure 10: CoFi traverse 2016/17. Snow cores were retrieved from all sites, Firn cores were drilled at sites 12, 14 and 15, a trench study was conducted at site 12. Map courtesy of A. Weinhart.

5.6 Data and code availability

The scripts and algorithms presented here as well as in the listed publications were made available to Dr. Johannes Freitag as the person responsible for the AWI-Ice-CT. All datasets generated by the author were transferred to the AWI-Ice-CT storage system (that automatically runs an weekly backup on tape) and all raw data were archived on hssrv2, a central storage system at AWI. Data related to the listed publications was made available via PANGAEA[®]:

Schaller, C. F.; Freitag, J.; Kipfstuhl, S.; Laepple, T.; Steen-Larsen, H. C.; Eisen, O. (2016): NEEM to EGRIP traverse – density and d18O of the surface snow (2 m profiles). *PANGAEA*, <https://doi.org/10.1594/PANGAEA.867875>

Schaller, C. F.; Freitag, J.; Eisen, O. (2017): Firn microstructure in the lock-in zone for three polar ice cores. *PANGAEA*, <https://doi.org/10.1594/PANGAEA.879577>

Schaller, C. F.; Kipfstuhl, S.; Steen-Larsen, H. C.; Freitag, J.; Eisen, O. (2017): Spatial variability of density stratigraphy and melt features for two polar snowpacks in Greenland and East Antarctica. *PANGAEA*, <https://doi.org/10.1594/PANGAEA.884003>

References

- Alley, R. B., and S. Anandakrishnan (1995), Variations in melt-layer frequency in the GISP2 ice core: implications for Holocene summer temperatures in central Greenland, *Ann. Glaciol.*, *21*, 64–70, doi:10.1017/S0260305500015615.
- Barnes, D. K. A., and C.-D. Hillenbrand (2010), Faunal evidence for a late quaternary trans-Antarctic seaway, *Glob. Change Biol.*, *16*(12), 3297–3303, doi:10.1111/j.1365-2486.2010.02198.x.
- Bendel, V., K. J. Ueltzhoeffer, J. Freitag, S. Kipfstuhl, W. F. Kuhs, C. S. Garbe, and S. H. Faria (2013), High-resolution variations in size, number and arrangement of air bubbles in the EPICA DML (Antarctica) ice core, *J. Glaciol.*, *59*(217), 972–980, doi:10.3189/2013JoG12J245.
- Bender, M. L., G. Floch, J. Chappellaz, M. Suwa, J.-M. Barnola, T. Blunier, G. Dreyfus, J. Jouzel, and F. Parrenin (2006), Gas age-ice age differences and the chronology of the Vostok ice core, 0–100 ka, *J. Geophys. Res.*, *111*(D21115), doi:10.1029/2005JD006488.
- Bennartz, R., M. D. Shupe, D. D. Turner, V. P. Walden, K. Steffen, C. J. Cox, M. S. Kurlie, N. B. Miller, and C. Pettersen (2013), July 2012 Greenland melt extent enhanced by low-level liquid clouds, *Nature*, *496*(7443), 83–86, doi:10.1038/nature12002.
- Bhatt, U. S., D. A. Walker, J. E. Walsh, E. C. Carmack, K. E. Frey, W. N. Meier, S. E. Moore, F.-J. W. Parmentier, E. Post, V. E. Romanovsky, and W. R. Simpson (2014), Implications of Arctic Sea Ice Decline for the Earth System, *Annu. Rev. Environ. Resour.*, *39*(1), 57–89, doi:10.1146/annurev-environ-122012-094357.
- Birnbaum, G., J. Freitag, R. Brauner, G. Koenig-Langlo, E. Schulz, S. Kipfstuhl, H. Oerter, C. H. Reijmer, E. Schlosser, S. H. Faria, and others (2010), Strong-wind events and their influence on the formation of snow dunes: observations from Kohnen station, Dronning Maud Land, Antarctica, *J. Glaciol.*, *56*(199), 891–902, doi:10.3189/002214310794457272.
- Box, J. E., X. Fettweis, J. C. Stroeve, M. Tedesco, D. K. Hall, and K. Steffen (2012), Greenland ice sheet albedo feedback: thermodynamics and atmospheric drivers, *Cryosphere*, *6*(4), 821–839, doi:10.5194/tc-6-821-2012.
- Breant, C., P. Martinerie, A. Orsi, L. Arnaud, and A. Landais (2017), Modelling firn thickness evolution during the last deglaciation: constraints on sensitivity to temperature and impurities, *Clim. Past*, *13*(7), 833–853, doi:10.5194/cp-13-833-2017.
- Buizert, C., K. M. Cuffey, J. P. Severinghaus, D. Baggenstos, T. J. Fudge, E. J. Steig, B. R. Markle, M. Winstrup, R. H. Rhodes, E. J. Brook, T. A. Sowers, G. D. Clow, H. Cheng, R. L. Edwards, M. Sigl, J. R. McConnell, and K. C. Taylor (2015), The WAIS Divide deep ice core WD2014 chronology – Part 1: Methane synchronization (68–31 ka BP) and the gas age–ice age difference, *Clim. Past*, *11*(2), 153–173, doi:10.5194/cp-11-153-2015.
- Capron, E., A. Landais, D. Buiron, A. Cauquoin, J. Chappellaz, M. Debret, J. Jouzel, M. Leuenberger, P. Martinerie, V. Masson-Delmotte, R. Mulvaney, F. Parrenin, and F. Prie (2013), Glacial–interglacial dynamics of Antarctic firn columns: comparison

- between simulations and ice core air- $\delta^{15}\text{N}$ measurements, *Clim. Past*, *9*(3), 983–999, doi:10.5194/cp-9-983-2013.
- Cavitte, M. G. P., D. D. Blankenship, D. A. Young, D. M. Schroeder, F. Parrenin, E. Lemeur, J. A. Macgregor, and M. J. Siegert (2016), Deep radiostratigraphy of the East Antarctic plateau: connecting the Dome C and Vostok ice core sites, *J. Glaciol.*, *62*(232), 323–334, doi:10.1017/jog.2016.11.
- Chen, Q.-S., D. H. Bromwich, and L. Bai (1997), Precipitation over Greenland retrieved by a dynamic method and its relation to cyclonic activity, *J. Clim.*, *10*(5), 839–870.
- Clausen, H., N. Gundestrup, S. Johnsen, R. Bindshadler, and J. Zwally (1988), Glaciological Investigations in the Crete Area, Central Greenland: A Search for a new Deep-Drilling Site, *Ann. Glaciol.*, *10*, 10–15, doi:10.1017/S0260305500004080.
- Colbeck, S. C. (1975), A theory for water flow through a layered snowpack, *Water Resour. Res.*, *11*(2), 261–266, doi:10.1029/WR011i002p00261.
- Colbeck, S. C. (1989), Air movement in snow due to windpumping, *J. Glaciol.*, *35*(120), 209–213.
- Criel, J., and E. Tsiporkova (2006), Gene Time Expression Warper: a tool for alignment, template matching and visualization of gene expression time series, *Bioinformatics*, *22*(2), 251–252, doi:10.1093/bioinformatics/bti787.
- Das, S. B., and R. B. Alley (2005), Characterization and formation of melt layers in polar snow: observations and experiments from West Antarctica, *J. Glaciol.*, *51*(173), 307–312, doi:10.3189/172756505781829395.
- Doyle, S. H., A. Hubbard, R. S. W. van de Wal, J. E. Box, D. van As, K. Scharrer, T. W. Meierbachtol, P. C. J. P. Smeets, J. T. Harper, E. Johansson, R. H. Mottram, A. B. Mikkelsen, F. Wilhelms, H. Patton, P. Christoffersen, and B. Hubbard (2015), Amplified melt and flow of the Greenland ice sheet driven by late-summer cyclonic rainfall, *Nat. Geosci.*, *8*(8), 647–653, doi:10.1038/ngeo2482.
- Durand, M., E. J. Kim, S. A. Margulis, and N. P. Molotch (2011), A First-Order Characterization of Errors From Neglecting Stratigraphy in Forward and Inverse Passive Microwave Modeling of Snow, *IEEE Geosci. Remote Sens. Lett.*, *8*(4), 730–734, doi:10.1109/LGRS.2011.2105243.
- Eicher, O., M. Baumgartner, A. Schilt, J. Schmitt, K. Schwander, T. F. Stocker, and H. Fischer (2016), Climatic and insolation control on the high-resolution total air content in the NGRIP ice core, *Clim. Past*, *12*(10), 1979–1993, doi:10.5194/cp-12-1979-2016.
- EPICA community members (2004), Eight glacial cycles from an Antarctic ice core, *Nature*, *429*(6992), 623–628, doi:10.1038/nature02599.
- Ettrema, J., M. R. van den Broeke, E. van Meijgaard, W. J. van de Berg, J. L. Bamber, J. E. Box, and R. C. Bales (2009), Higher surface mass balance of the Greenland ice sheet revealed by high-resolution climate modeling, *Geophys. Res. Lett.*, *36*(12), doi:10.1029/2009GL038110.

- Fausto, R. S., D. van As, J. E. Box, W. Colgan, P. L. Langen, and R. H. Mottram (2016), The implication of nonradiative energy fluxes dominating Greenland ice sheet exceptional ablation area surface melt in 2012, *Geophys. Res. Lett.*, *43*(6), 2649–2658, doi:10.1002/2016GL067720.
- Fettweis, X., E. Hanna, C. Lang, A. Belleflamme, M. Erpicum, and H. Gallee (2013), Important role of the mid-tropospheric atmospheric circulation in the recent surface melt increase over the Greenland ice sheet, *Cryosphere*, *7*(1), 241–248, doi:10.5194/tc-7-241-2013.
- Fischer, H., J. Severinghaus, E. Brook, E. Wolff, M. Albert, O. Alemany, R. Arthern, C. Bentley, D. Blankenship, J. Chappellaz, T. Creyts, D. Dahl-Jensen, M. Dinn, M. Frezzotti, S. Fujita, H. Gallee, R. Hindmarsh, D. Hudspeth, G. Jugie, K. Kawamura, V. Lipenkov, H. Miller, R. Mulvaney, F. Parrenin, F. Pattyn, C. Ritz, J. Schwander, D. Steinhage, T. van Ommen, and F. Wilhelms (2013), Where to find 1.5 million yr old ice for the IPICS "Oldest-Ice" ice core, *Clim. Past*, *9*(6), 2489–2505, doi:10.5194/cp-9-2489-2013.
- Fisher, D. A., N. Reeh, and H. Clausen (1985), Stratigraphic noise in time series derived from ice cores, *Ann. Glaciol.*, *7*, 76–83, doi:10.3189/S0260305500005942.
- Freitag, J., S. Kipfstuhl, T. Laepple, and F. Wilhelms (2013a), Impurity-controlled densification: a new model for stratified polar firn, *J. Glaciol.*, *59*(218), 1163–1169, doi:10.3189/2013JoG13J042.
- Freitag, J., S. Kipfstuhl, and T. Laepple (2013b), Core-scale radiosopic imaging: a new method reveals density–calcium link in Antarctic firn, *J. Glaciol.*, *59*(218), 1009–1014, doi:10.3189/2013JoG13J028.
- Gabrielli, P., C. Barbante, G. Bertagna, M. Berto, D. Binder, A. Carton, L. Carturan, F. Cazorzi, G. Cozzi, G. Dalla Fontana, M. Davis, F. De Blasi, R. Dinale, G. Draga, G. Dreossi, D. Festi, M. Frezzotti, J. Gabrieli, S. P. Galos, P. Ginot, P. Heidenwolf, T. M. Jenk, N. Kehrwald, D. Kenny, O. Magand, V. Mair, V. Mikhalenko, P. N. Lin, K. Oeggl, G. Piffer, M. Rinaldi, U. Schotterer, M. Schwikowski, R. Seppi, A. Spolaor, B. Stenni, D. Tonidandel, C. Uglietti, V. Zagorodnov, T. Zanoner, and P. Zennaro (2016), Age of the Mt. Ortles ice cores, the Tyrolean Iceman and glaciation of the highest summit of South Tyrol since the Northern Hemisphere Climatic Optimum, *Cryosphere*, *10*(6), 2779–2797, doi:10.5194/tc-10-2779-2016.
- Gregory, S. A., M. R. Albert, and I. Baker (2014), Impact of physical properties and accumulation rate on pore close-off in layered firn, *Cryosphere*, *8*(1), 91–105, doi:10.5194/tc-8-91-2014.
- Haam, E., and P. Huybers (2010), A test for the presence of covariance between time-uncertain series of data with application to the Dongge Cave speleothem and atmospheric radiocarbon records, *Paleoceanography*, *25*(2), PA2209, doi:10.1029/2008PA001713.
- Hall, D. K., J. C. Comiso, N. E. DiGirolamo, C. A. Shuman, J. E. Box, and L. S. Koenig (2013), Variability in the surface temperature and melt extent of the Greenland ice sheet from MODIS, *Geophys. Res. Lett.*, *40*(10), 2114–2120, doi:10.1002/grl.50240.
- Herron, M. M., and C. C. Langway (1980), Firn Densification: An Empirical Model, *J. Glaciol.*, *25*(93), 373–385, doi:10.1017/S0022143000015239.

- Hoerhold, M., T. Laepple, J. Freitag, M. Bigler, H. Fischer, and S. Kipfstuhl (2012), On the impact of impurities on the densification of polar firn, *Earth Planet. Sci. Lett.*, *325–326*, 93–99, doi:10.1016/j.epsl.2011.12.022.
- Hoerhold, M. W., S. Kipfstuhl, F. Wilhelms, J. Freitag, and A. Frenzel (2011), The densification of layered polar firn, *J. Geophys. Res. Earth Surf.*, *116*(F1001), doi: 10.1029/2009JF001630.
- Humphrey, N. F., J. T. Harper, and W. T. Pfeffer (2012), Thermal tracking of meltwater retention in Greenland’s accumulation area, *J. Geophys. Res.*, *117*(F01010), doi: 10.1029/2011JF002083.
- IPCC (2014), *Climate change 2014: Synthesis report. Contribution of Working Groups I, II and III to the Fifth Assessment Report of the Intergovernmental Panel on Climate Change [Core Writing Team, R.K. Pachauri and L.A. Meyer (eds.)]*, Intergovernmental Panel on Climate Change, Geneva, Switzerland.
- Kobashi, T., T. Ikeda-Fukazawa, M. Suwa, J. Schwander, T. Kameda, J. Lundin, A. Hori, H. Motoyama, M. Doering, and M. Leuenberger (2015), Post-bubble close-off fractionation of gases in polar firn and ice cores: effects of accumulation rate on permeation through overloading pressure, *Atmospheric Chem. Phys.*, *15*(24), 13,895–13,914, doi:10.5194/acp-15-13895-2015.
- Laepple, T., M. Hoerhold, T. Muench, J. Freitag, A. Wegner, and S. Kipfstuhl (2016), Layering of surface snow and firn at Kohlen Station, Antarctica: Noise or seasonal signal?, *J. Geophys. Res. Earth Surf.*, *121*(10), 1849–1860, doi:10.1002/2016JF003919.
- Landais, A., J. Barnola, K. Kawamura, N. Caillon, M. Delmotte, T. Van Ommen, G. Dreyfus, J. Jouzel, V. Masson-Delmotte, B. Minster, J. Freitag, M. Leuenberger, J. Schwander, C. Huber, D. Etheridge, and V. Morgan (2006), Firn-air $\delta^{15}\text{N}$ in modern polar sites and glacial–interglacial ice: a model-data mismatch during glacial periods in Antarctica?, *Quat. Sci. Rev.*, *25*(1–2), 49–62, doi:10.1016/j.quascirev.2005.06.007.
- Langway, C. C., and H. Shoji (1990), Past Temperature Record From The Analysis of Melt Features In The Dye 3, Greenland, Ice Core, *Ann. Glaciol.*, *14*, 343–344, doi:10.1017/S0260305500009095.
- Legrand, M., and P. Mayewski (1997), Glaciochemistry of polar ice cores: A review, *Rev. Geophys.*, *35*(3), 219–243, doi:10.1029/96RG03527.
- Lehning, M., P. Bartelt, B. Brown, T. Russi, U. Stoeckli, and M. Zimmerli (1999), SNOWPACK model calculations for avalanche warning based upon a new network of weather and snow stations, *Cold Reg. Sci. Technol.*, *30*(1–3), 145–157, doi:10.1016/S0165-232X(99)00022-1.
- Lenton, T. M., H. Held, E. Kriegler, J. W. Hall, W. Lucht, S. Rahmstorf, and H. J. Schellnhuber (2008), Tipping elements in the Earth’s climate system, *Proc Natl. Acad. Sci.*, *105*(6), 1786–1793.
- Libois, Q., G. Picard, L. Arnaud, S. Morin, and E. Brun (2014), Modeling the impact of snow drift on the decameter-scale variability of snow properties on the Antarctic Plateau, *J. Geophys. Res.*, *119*(20), 11,662–11,681, doi:10.1002/2014JD022361.

- Martinerie, P., V. Y. Lipenkov, and D. Raynaud (1990), Correction of air-content measurements in polar ice for the effect of cut bubbles at the surface of the sample, *J. Glaciol.*, *36*(124), 299–303.
- Martinerie, P., D. Raynaud, D. M. Etheridge, J.-M. Barnola, and D. Mazaudier (1992), Physical and climatic parameters which influence the air content in polar ice, *Earth Planet. Sci. Lett.*, *112*(1–4), 1–13.
- McGrath, D., W. Colgan, N. Bayou, A. Muto, and K. Steffen (2013), Recent warming at Summit, Greenland: Global context and implications, *Geophys. Res. Lett.*, *40*(10), 2091–2096, doi:10.1002/grl.50456.
- Mitchell, L. E., C. Buizert, E. J. Brook, D. J. Breton, J. Fegyveresi, D. Baggenstos, A. Orsi, J. Severinghaus, R. B. Alley, M. Albert, R. H. Rhodes, J. R. McConnell, M. Sigl, O. Maselli, S. Gregory, and J. Ahn (2015), Observing and modeling the influence of layering on bubble trapping in polar firn, *J. Geophys. Res.*, *120*(6), 2558–2574, doi:10.1002/2014JD022766.
- Muench, T., S. Kipfstuhl, J. Freitag, H. Meyer, and T. Laepple (2016), Regional climate signal vs. local noise: a two-dimensional view of water isotopes in Antarctic firn at Kohnen Station, Dronning Maud Land, *Clim. Past*, *12*(7), 1565–1581, doi:10.5194/cp-12-1565-2016.
- NEEM community members (2013), Eemian interglacial reconstructed from a Greenland folded ice core, *Nature*, *493*(7433), 489–494, doi:10.1038/nature11789.
- Nghiem, S. V., D. K. Hall, T. L. Mote, M. Tedesco, M. R. Albert, K. Keegan, C. A. Shuman, N. E. DiGirolamo, and G. Neumann (2012), The extreme melt across the Greenland ice sheet in 2012, *Geophys. Res. Lett.*, *39*(20), doi:10.1029/2012GL053611.
- Nguyen, T. T., T. N. Tran, T. A. Willemsz, H. W. Frijlink, T. Ervasti, J. Ketolainen, and K. van der Voort Maarschalk (2011), A density based segmentation method to determine the coordination number of a particulate system, *Chem. Eng. Sci.*, *66*(24), 6385–6392, doi:https://doi.org/10.1016/j.ces.2011.08.044.
- Nilsson, J., P. Vallelonga, S. B. Simonsen, L. S. Sorensen, R. Forsberg, D. Dahl-Jensen, M. Hirabayashi, K. Goto-Azuma, C. S. Hvidberg, H. A. Kjaer, and K. Satow (2015), Greenland 2012 melt event effects on CryoSat-2 radar altimetry, *Geophys. Res. Lett.*, *42*(10), 3919–3926, doi:10.1002/2015GL063296.
- Obbard, R. W., G. Troderman, and I. Baker (2009), Imaging brine and air inclusions in sea ice using micro-X-ray computed tomography, *J. Glaciol.*, *55*(194), 1113–1115, doi:10.3189/002214309790794814.
- Orsi, A. J., K. Kawamura, J. M. Fegyveresi, M. A. Headly, R. B. Alley, and J. P. Severinghaus (2015), Differentiating bubble-free layers from melt layers in ice cores using noble gases, *J. Glaciol.*, *61*(227), 585–594, doi:10.3189/2015JoG14J237.
- Parrenin, F., S. Barker, T. Blunier, J. Chappellaz, J. Jouzel, A. Landais, V. Masson-Delmotte, J. Schwander, and D. Veres (2012), On the gas-ice depth difference (Δ depth) along the EPICA Dome C ice core, *Clim. Past*, *8*(4), 1239–1255, doi:10.5194/cp-8-1239-2012.

- Parry, V., P. Nienow, D. Mair, J. Scott, B. Hubbard, K. Steffen, and D. Wingham (2007), Investigations of meltwater refreezing and density variations in the snowpack and firn within the percolation zone of the Greenland ice sheet, *Ann. Glaciol.*, *46*(1), 61–68.
- Pfeffer, W. T., and N. F. Humphrey (1996), Determination of timing and location of water movement and ice-layer formation by temperature measurements in sub-freezing snow, *J. Glaciol.*, *42*(141), 292–304, doi:10.1017/S002214300004159.
- Pfeffer, W. T., T. H. Illangasekare, and M. F. Meier (1990), Analysis and Modeling of Melt-Water Refreezing in Dry Snow, *J. Glaciol.*, *36*(123), 238–246, doi:10.3189/S002214300009497.
- Picard, G., L. Brucker, A. Roy, F. Dupont, M. Fily, A. Royer, and C. Harlow (2013), Simulation of the microwave emission of multi-layered snowpacks using the Dense Media Radiative transfer theory: the DMRT-ML model, *Geosci. Model Dev.*, *6*(4), 1061–1078, doi:10.5194/gmd-6-1061-2013.
- Proksch, M., H. Loewe, and M. Schneebeli (2015), Density, specific surface area, and correlation length of snow measured by high-resolution penetrometry, *J. Geophys. Res. Earth Surf.*, *120*(2), 346–362, doi:10.1002/2014JF003266.
- Raynaud, D., V. Lipenkov, B. Lemieux-Dudon, P. Duval, M.-F. Loutre, and N. Lhomme (2007), The local insolation signature of air content in Antarctic ice. A new step toward an absolute dating of ice records, *Earth Planet. Sci. Lett.*, *261*(3-4), 337–349, doi:10.1016/j.epsl.2007.06.025.
- Reijmer, C. H., M. R. van den Broeke, X. Fettweis, J. Ettema, and L. B. Stap (2012), Refreezing on the Greenland ice sheet: a comparison of parameterizations, *Cryosphere*, *6*(4), 743–762, doi:10.5194/tc-6-743-2012.
- Rignot, E., J. Mouginot, M. Morlighem, H. Seroussi, and B. Scheuchl (2014), Widespread, rapid grounding line retreat of Pine Island, Thwaites, Smith, and Kohler glaciers, West Antarctica, from 1992 to 2011, *Geophys. Res. Lett.*, *41*(10), 3502–3509, doi:10.1002/2014GL060140.
- Rowe, C. M., M. R. Anderson, T. L. Mote, and K. C. Kuivinen (1995), Indications of melt in near-surface ice-core stratigraphy: comparisons with passive-microwave melt signals over the Greenland ice sheet, *Ann. Glaciol.*, *21*, 59–63, doi:10.1017/S0260305500015603.
- Rutter, N., M. Sandells, C. Derksen, P. Toose, A. Royer, B. Montpetit, A. Langlois, J. Lemmetyinen, and J. Pulliainen (2014), Snow stratigraphic heterogeneity within ground-based passive microwave radiometer footprints: Implications for emission modeling, *J. Geophys. Res. Earth Surf.*, *119*(3), 550–565, doi:10.1002/2013JF003017.
- Sander, M. (2017), Räumliche Spurenstoffanalyse in polarem Schnee in Dronning Maud Land, Bachelor’s thesis, Georg-August-Universitaet Göttingen.
- Schaidt, M. (2017), Aufbau und Zusammensetzung der Schneedecke in Grönland, Bachelor’s thesis, Georg-August-Universitaet Göttingen.
- Scherer, R. P., A. Aldahan, S. Tulaczyk, G. Possnert, E. Engelhardt, and B. Kamb (1998), Pleistocene Collapse of the West Antarctic Ice Sheet, *Science*, *281*(5373), 82–85, doi:10.1126/science.281.5373.82.

- Schneebeli, M., and S. A. Sokratov (2004), Tomography of temperature gradient metamorphism of snow and associated changes in heat conductivity, *Hydrol. Process.*, *18*(18), 3655–3665, doi:10.1002/hyp.5800.
- Schwander, J., and B. Stauffer (1984), Age difference between polar ice and the air trapped in its bubbles, *Nature*, *311*(5981), 45–47, doi:10.1038/311045a0.
- Schwander, J., J.-M. Barnola, C. Andrie, M. Leuenberger, A. Ludin, D. Raynaud, and B. Stauffer (1993), The age of the air in the firn and the ice at Summit, Greenland, *J. Geophys. Res.*, *98*(D2), 2831–2838.
- Schwander, J., T. Sowers, J.-M. Barnola, T. Blunier, A. Fuchs, and B. Malaize (1997), Age scale of the air in the summit ice: Implication for glacial-interglacial temperature change, *J. Geophys. Res.*, *102*(D16), 19,483–19,493, doi:10.1029/97JD01309.
- Severinghaus, J., and M. Battle (2006), Fractionation of gases in polar ice during bubble close-off: New constraints from firn air Ne, Kr and Xe observations, *Earth Planet. Sci. Lett.*, *244*(1-2), 474–500, doi:10.1016/j.epsl.2006.01.032.
- Severinghaus, J. P., A. Grachev, and M. Battle (2001), Thermal fractionation of air in polar firn by seasonal temperature gradients, *Geochem. Geophys.*, *2*(7).
- Shepherd, A., E. R. Ivins, G. A. V. R. Barletta, M. J. Bentley, S. Bettadpur, K. H. Briggs, D. H. Bromwich, R. Forsberg, N. Galin, M. Horwath, S. Jacobs, I. Joughin, M. A. King, J. T. M. Lenaerts, J. Li, S. R. M. Ligtenberg, A. Luckman, S. B. Luthcke, M. McMillan, R. Meister, G. Milne, J. Mouginot, A. Muir, J. P. Nicolas, J. Paden, A. J. Payne, H. Pritchard, E. Rignot, H. Rott, L. S. Sorensen, T. A. Scambos, B. Scheuchl, E. J. O. Schrama, B. Smith, A. V. Sundal, J. H. van Angelen, W. J. van de Berg, M. R. van den Broeke, D. G. Vaughan, I. Velicogna, J. Wahr, P. L. Whitehouse, D. J. Wingham, D. Yi, D. Young, and H. J. Zwally (2012), A Reconciled Estimate of Ice-Sheet Mass Balance, *Science*, *338*(6111), 1183–1189, doi:10.1126/science.1228102.
- Sowers, T., M. Bender, D. Raynaud, and Y. S. Korotkevich (1992), $\delta^{15}\text{N}$ of N_2 in air trapped in polar ice: A tracer of gas transport in the firn and a possible constraint on ice age-gas age differences, *J. Geophys. Res.*, *97*(D14), 15,683–15,697, doi:10.1029/92JD01297.
- Steig, E. J., K. Huybers, H. A. Singh, N. J. Steiger, Q. Ding, D. M. W. Frierson, T. Popp, and J. W. C. White (2015), Influence of West Antarctic Ice Sheet collapse on Antarctic surface climate, *Geophys. Res. Lett.*, *42*(12), 4862–4868, doi:10.1002/2015GL063861.
- Steinhage, D., S. Kipfstuhl, U. Nixdorf, and H. Miller (2013), Internal structure of the ice sheet between Kohnen station and Dome Fuji, Antarctica, revealed by airborne radio-echo sounding, *Ann. Glaciol.*, *54*(64), 163–167, doi:10.3189/2013AoG64A113.
- Stroeve, J. C., T. Markus, L. Boisvert, J. Miller, and A. Barrett (2014), Changes in Arctic melt season and implications for sea ice loss: Stroeve et al.: Arctic melt season changes, *Geophys. Res. Lett.*, *41*(4), 1216–1225, doi:10.1002/2013GL058951.
- Tedesco, M. (2007), Snowmelt detection over the Greenland ice sheet from SSM/I brightness temperature daily variations, *Geophys. Res. Lett.*, *34*(2), doi:10.1029/2006GL028466.

- Tedesco, M., X. Fettweis, T. Mote, J. Wahr, P. Alexander, J. E. Box, and B. Wouters (2013), Evidence and analysis of 2012 Greenland records from spaceborne observations, a regional climate model and reanalysis data, *Cryosphere*, *7*(2), 615–630, doi:10.5194/tc-7-615-2013.
- Vionnet, V., E. Brun, S. Morin, A. Boone, S. Faroux, P. Le Moigne, E. Martin, and J.-M. Willemet (2012), The detailed snowpack scheme Crocus and its implementation in SURFEX v7.2, *Geosci. Model Dev.*, *5*(3), 773–791, doi:10.5194/gmd-5-773-2012.
- Wagenbach, D., and K. Geis (1989), The Mineral Dust Record in a High Altitude Alpine Glacier (Colle Gnifetti, Swiss Alps), in *Paleoclimatology and Paleometeorology: Modern and Past Patterns of Global Atmospheric Transport*, edited by M. Leinen and M. Sarnthein, pp. 543–564, Springer Netherlands, Dordrecht, doi:10.1007/978-94-009-0995-3_23.

Acknowledgments

There are several people without whom this thesis would probably not exist. The arrangement of the following paragraphs is no judgment of the importance of their contributions.

It was Prof. Dr. Olaf Eisen and his commitment to scientific outreach (in my case in the form of the AWI-Eisblog) that attracted my attention when I was looking for an inspiring PhD topic. He encouraged me to apply for a PhD scholarship for a glaciological subject of my choice and agreed to act as my supervisor, even though I did not choose one of the topics in his working group. Throughout the three years of my PhD, he was always there to provide advice and back me up when needed. I particularly enjoyed our joint mountaineering experiences. Finally, it was him who introduced me to ..

.. Dr. Johannes Freitag, who presented me with the opportunity to work with the AWI-Ice-CT. He was able to raise my enthusiasm for our studies to a level at which I still feel very attached to the CT lab although I am leaving. It was a pleasure and an enriching experience to share an office with you as well as ..

.. Alexander Weinhart and Tetsuro Taranczewski, my co-PhDs. We spent a considerable amount of time together – not only in the office, but also doing sports and enjoying our lives. It was great to share impressions and troubles with you and I wish you all the best for your remaining time at AWI. May our team spirit not be forgotten. It was not only you, but also ..

.. Melissa Mengert, Julia Martin, Sophie Ehrhardt and Julia Goedecke, who made the CT lab an awesome workplace. In the isolation of the ground floor, we enjoyed cookies and cake even more often than ..

.. the AWI glaciology group, that provided a very stimulating environment to work in. There are too many people to list here, but those that I enjoyed coffee breaks, discussions and joint activities with will know. Within the ice-core working group, I want to thank ..

.. Prof. Dr. Frank Wilhelms, for his willingness to review this thesis and supporting me in various administrative matters. However, ..

.. Dr. Sepp Kipfstuhl and I did not only have to endure collaboration in Bremerhaven, but also in the field. Our joint expeditions to Greenland and Antarctica were an amazing experience and I learned a lot from you. Anyway, I am sure you already knew years ago.

I am very grateful to the German National Merit Foundation (Studienstiftung des deutschen Volkes e.V.) for funding my PhD project. Interaction with other PhDs, also via POLMAR and the Helmholtz Juniors, was very helpful in coping with the challenges of a PhD.

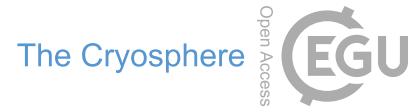
Credits for proofreading go to the current CT crew. Copernicus Publications and the American Geophysical Union kindly permitted the reprinting of the appended papers.

Appendix

Publication I

Schaller, C. F., Freitag, J., Kipfstuhl, S., Laepple, T., Steen-Larsen, H. C., and Eisen, O.: A representative density profile of the North Greenland snowpack, *The Cryosphere*, 10, 1991–2002, <https://doi.org/10.5194/tc-10-1991-2016>, 2016

The Cryosphere, 10, 1991–2002, 2016
www.the-cryosphere.net/10/1991/2016/
doi:10.5194/tc-10-1991-2016
© Author(s) 2016. CC Attribution 3.0 License.



A representative density profile of the North Greenland snowpack

Christoph Florian Schaller¹, Johannes Freitag¹, Sepp Kipfstuhl¹, Thomas Laepple², Hans Christian Steen-Larsen³, and Olaf Eisen^{1,4}

¹Alfred Wegener Institute, Helmholtz Centre for Polar and Marine Research, Bremerhaven, Germany

²Alfred Wegener Institute, Helmholtz Centre for Polar and Marine Research, Potsdam, Germany

³Centre for Ice and Climate, Niels Bohr Institute, University of Copenhagen, Copenhagen, Denmark

⁴Department of Geosciences, University of Bremen, Bremen, Germany

Correspondence to: Christoph Florian Schaller (christoph.schaller@awi.de)

Received: 28 April 2016 – Published in The Cryosphere Discuss.: 10 May 2016

Revised: 7 August 2016 – Accepted: 22 August 2016 – Published: 7 September 2016

Abstract. Along a traverse through North Greenland in May 2015 we collected snow cores up to 2 m depth and analyzed their density and water isotopic composition. A new sampling technique and an adapted algorithm for comparing data sets from different sites and aligning stratigraphic features are presented. We find good agreement of the density layering in the snowpack over hundreds of kilometers, which allows the construction of a representative density profile. The results are supported by an empirical statistical density model, which is used to generate sets of random profiles and validate the applied methods. Furthermore we are able to calculate annual accumulation rates, align melt layers and observe isotopic temperatures in the area back to 2010. Distinct relations of $\delta^{18}\text{O}$ with both accumulation rate and density are deduced. Inter alia the depths of the 2012 melt layers and high-resolution densities are provided for applications in remote sensing.

1 Introduction

In the context of global warming, the Greenland ice sheet has been identified as a so-called “tipping point” of climate change (Lenton et al., 2008). The sea level rise caused by its decay may have a severe impact on human society as well as ecological systems. Thus the difference in accumulation across the interior of the ice sheet and seasonal melting, runoff and calving at its borders, the so-called mass balance, has been in the focus of recent scientific activities in the Arctic region. The applied methods for its determination range from satellite remote sensing (e.g., Zwally et al., 2011)

to regional climate modeling (e.g., Fettweis, 2007) and to large-scale climate simulations constrained by weather station data and ice core records (e.g., Hanna et al., 2011). Even though first accumulation and density measurements had already been carried out in 1952–1954 (Bull, 1958) using accumulation stakes and Rammsonde measurements at a few points alongside the gravity survey of the British North Greenland Expedition, large-scale studies such as Benson (1962) are still very rare. To obtain accumulation maps of Greenland such as Bales et al. (2009), diverse data sets from ice cores, snow pits and weather stations have to be collected over several years. Recently Hawley et al. (2014) conducted a ground-penetrating radar survey alongside a traverse of about 1000 km length, supported by a few snow pits and shallow cores for bulk densities and chemical profiling. Koenig et al. (2016) used airborne snow radar to determine accumulation rates from 2009 to 2012 along flight paths of more than 10 000 km.

In summer 2012, there were 2 very warm days with temperatures above 0 °C almost all over Greenland, causing substantial melt layers (Nghiem et al., 2012). Although this was a very rare event induced by a special weather situation (Benjamin et al., 2013), the newly formed ice layers strongly influenced the physical properties of snow and firn (Nilsson et al., 2015).

We introduce a new and efficient technique for sampling the snowpack along traverses, which allows for additional lab-based measurements to gain high-resolution profiles of physical snow properties such as density. Furthermore we adapt an algorithm from speech recognition to align these spatially distributed data sets and provide further insight into

Published by Copernicus Publications on behalf of the European Geosciences Union.

1992

Table 1. Measurement sites along the traverse, see also Fig. 1. The missing liner numbers (e.g., N2E_01) result from multiple samples being taken at some locations. Nonetheless, only one profile per location was used for this study.

Site	Longitude	Latitude	Traverse kilometer
NEEM (N2E_02)	51.06914° W	77.444337° N	0.00
N2E_03	50.11° W	77.3669° N	24.80
N2E_04	49.23077° W	77.25429° N	49.66
N2E_05	48.170872° W	77.120098° N	79.76
N2E_06	47.13806° W	76.98195° N	109.73
N2E_07	46.14227° W	76.84788° N	138.90
N2E_08	45.27375° W	76.71337° N	165.57
N2E_09	44.78786° W	76.52426° N	190.03
N2E_10	44.09225° W	76.40034° N	212.78
N2E_11	43.06116° W	76.32535° N	241.07
N2E_12	42.051636° W	76.248888° N	269.01
N2E_14	41.16026° W	76.1777° N	293.92
N2E_15	40.29929° W	76.10455° N	318.25
N2E_16	39.31873° W	76.01559° N	346.32
N2E_17	38.46937° W	75.93539° N	370.88
N2E_19	37.69747° W	75.85845° N	393.48
N2E_20	36.54374° W	75.70614° N	429.25
EGRIP (N2E_22)	35.985618° W	75.629343° N	446.83

their development with changing surrounding conditions. The method is tested with randomly generated sets of density profiles with the same statistical properties as the original measurements. As an application we present data gained along a 450 km traverse in North Greenland, deduce relations of the individual parameters (density, $\delta^{18}\text{O}$ and accumulation rate) and show additional values of interest such as the depths of the 2012 melt layers.

2 Data acquisition and processing

In preparation for the upcoming East GRenland Ice core Project (EGRIP), the Danish Centre for Ice and Climate's dome and equipment had to be moved about 450 km from the previous drilling site, NEEM. Alongside this so-called "N2E" traverse in May 2015, several measurements of the upper part of the firn and the snow surface were taken. Amongst others, the upper 2 m of the snowpack was sampled using the "liner technique" described in detail below. Snow cores were taken approximately every 25 km at the sites shown in Fig. 1; detailed coordinates can be found in Table 1.

2.1 Liner technique

The sampling was done using carbon fiber tubes with sharp edges of 1 m length, 10 cm diameter and 1 mm wall thickness (called "liners"). To start off, the first liner was carefully pushed and hammered into the ground until its top was parallel to the snow surface. Nonetheless in a few cases the

C. F. Schaller et al.: North Greenland density profile

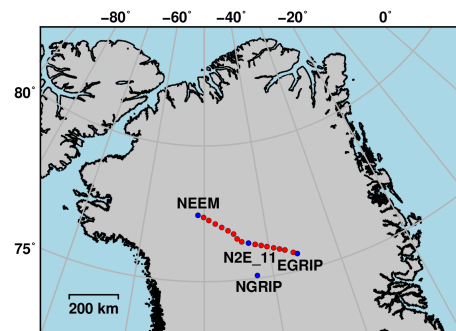


Figure 1. The N2E traverse route with the measurement sites according to Table 1.

snow core was slightly compacted by up to 2 cm in the vertical direction, visible as a reduction of the snow level inside the tube compared to the surroundings. Subsequently a snow pit of 1 m depth was dug next to the tube and the snow was cut off at its bottom using a metal plate or small saw. The tube was removed and its openings were sealed using matching plastic bags. Then the cutting surface was cleaned and the second liner was inserted right below the first one. Finally the pit had to be deepened to 2 m to once again cut off the snow and take the second liner. Theoretically the process described can be iterated up to an arbitrary depth. However, the area of the snow pit required increases significantly with every meter of depth gained. Sampling the upper 2 m took approximately 2 h per site.

2.2 X-ray tomography

The cores were transported to the Alfred Wegener Institute, Bremerhaven, in a frozen condition. All samples were analyzed in the AWI-Ice-CT (described in detail in Freitag et al., 2013), a unique X-ray computer tomograph (CT) in a cold lab, which allows micrometer-resolution density measurements of whole 1 m core segments in 2-D and 3-D. As part of the measurement procedure a sample holder for liners was constructed, which contains several pieces of pure ice of known geometry for calibration purposes. Amongst others, the effect of the carbon fiber tube being part of the scan was corrected for using empty tube measurements. Thus, the fragile snow cores do not have to be removed from the liners.

As the required measurement time increases with resolution, we chose to do 2-D scans with a pixel size of approximately 0.128 mm. Each of these scans takes about 3 min. However, 15 min m^{-1} are more realistic when including sample preparation and accurate documentation. Then, the raw measurement data are automatically processed by detecting the calibration unit and directly calculating densities from the CT images. Additionally, for each liner, the mean density is determined from the mass and geometry of the snow as an

C. F. Schaller et al.: North Greenland density profile

1993

independent comparison value. Figure 2 displays an example CT image with a zoomed section showing two melt layers in the snowpack aligned with the respective densities derived from 2-D analysis.

2.3 Isotope measurements

Finally, the snow was gently pushed out of the tubes and cut in samples with a vertical height of 1 cm for the 30 cm right below the surface and 2 cm otherwise. These samples were crushed and sealed in plastic bags. Finally water isotopes were measured using a Picarro L2130-i with a precision of $\sigma = 0.1\text{‰}$ for $\delta^{18}\text{O}$.

The snow was dated by determining and counting the maxima (summer) and minima (winter) in the seasonal $\delta^{18}\text{O}$ signal. Using the density data, accumulation rates at the different sites were calculated from the snow mass for the 3–5 years worth of accumulation contained in the top 2 m of the snowpack. In the present study, we only use winter-to-winter rates (separating years at the $\delta^{18}\text{O}$ minima) – summer-to-summer values were computed as a reference but do not show different behavior.

3 Mathematical methods

3.1 Automatic alignment of stratigraphic features

In order to efficiently analyze the data sets generated along the traverse, we investigated several ways to automatically detect coherent signals at the different sites. A well-known matching method is maximizing the cross-correlation. However, determining a constant shift in depth between two profiles is not suitable for our case as the accumulation rate, and thus the vertical spacing of layers, is subject to change going eastwards. Under the assumption of constant accumulation over time and no significant compaction in the top 2 m, one would expect a shift which linearly increases with depth and has a slope equal to the ratio of accumulation rates. Then again, local environmental conditions such as wind speed and direction influence the mass accumulated by a certain deposition event (Fisher et al., 1985). Therefore we aimed to align snow of the same origin and its properties with continuously changing shifts, a problem that has already been worked on at a lower vertical resolution for alpine snow (e.g., Hagenmuller and Pilloix, 2016).

The dynamic time warping (DTW) method, which was introduced in speech recognition in the 1970s (Itakura, 1975), provides an efficient algorithm for that purpose. It has already been applied in numerous fields, e.g., for the tracking of ice floes in synthetic aperture radar images (McConnell et al., 1991). For a detailed review of DTW, see Senin (2008).

The basic idea is to discretize the two data sets to be compared with the same step size l (resulting in two vectors S and T of length n and m) and then consecutively assign the values of one to another, whereby each value can be matched

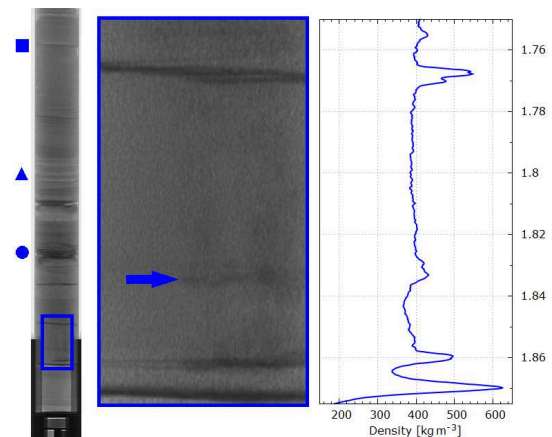


Figure 2. Example 2-D CT image of a 1 m liner (1–2 m depth) and a zoomed section showing two melt layers aligned with the respective densities. In the left image a distinct density layering (e.g., blue triangle), several melt layers (e.g., blue circle) and wind crusts (e.g., blue square) are visible. Above the lower zoomed melt layer a clear percolation pattern (blue arrow) can be seen on the right-hand side of the snow core.

with multiple values of the other data set. To find the best fit, one calculates a matrix \mathbf{D} , where $\mathbf{D}[i, j]$ indicates the error of the best path that leads to the i th element of the first data set being connected to the j th element of the second one.

The original algorithm starts by calculating the matrix in the upper left corner, fixing the first elements of both data sets to be linked with each other. Then it proceeds through the matrix by taking the path with the minimal error leading to the respective cell and adding the local error, i.e.,

$$\mathbf{D}[i, j] = \begin{cases} \infty & \text{for } i < 0 \text{ or } j < 0 \\ \|S[i] - T[0]\| & \text{for } i = 0 \text{ and } j = 0 \\ \|S[i] - T[j]\| + \min(\mathbf{D}[i, j-1], \mathbf{D}[i-1, j-1], \mathbf{D}[i-1, j]) & \text{else} \end{cases} \quad (1)$$

Finally, on arrival at cell $\mathbf{D}[n, m]$ it backtraces the path of minimal errors to $\mathbf{D}[0, 0]$, obtaining the best fit of the complete data sets in the given norm $\|\cdot\|$.

For our application – matching measurements of the upper 2 m of the snowpack – we do not aim to fit complete data sets, but rather allow for different offsets at the top and bottom. The former may be caused by variations of the snow surface due to current conditions, the latter by different accumulation rates, leading to data at the bottom of the liners not having any physical relation apart from being the deepest snow analyzed at the given location. To accomplish that, we expand the idea of Sakurai et al. (2007), introducing maximal surface and bottom index offsets s and b . Then we initialize \mathbf{D} by

$$\mathbf{D}[0, j] = \|S[0] - T[j]\| \text{ for } 0 \leq j \leq s \quad (2)$$

1994

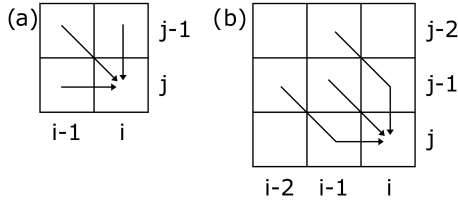


Figure 3. (a) Basic and (b) constrained stepping patterns for the DTW algorithm. Usage of cell $[i, j]$ indicates that the i th element of the first and the j th element of the second data set were matched. The basic pattern allows for a single value to be assigned to arbitrarily many values of the other data set, while for the constrained stepping, each value can only be identified with one or two others.

and

$$\underline{\mathbf{D}}[i, 0] = \|S[i] - T[0]\| \text{ for } 0 < i \leq s \quad (3)$$

before proceeding through the matrix. Finally instead of backtracing simply from $\underline{\mathbf{D}}[n, m]$, we end our fitting path at

$$\min \{ \underline{\mathbf{D}}[i, j] \mid (i = n \text{ and } m - b \leq j \leq m) \text{ or } (j = m \text{ and } n - b \leq i \leq n) \} \quad (4)$$

and search a trace back to any of the initialized elements. Thereby we find the best matching of subsets of S and T with a maximal shift of $s \cdot l$ at the top and $b \cdot l$ at the bottom. In between, we verify that a linearly increasing maximal shift is not exceeded.

The simple way we proceed through the matrix so far, often referred to as “stepping pattern”, is unrealistic for our case as a single value of one data set could be fit to arbitrarily many values of the other. Along the traverse we find the maximal ratio of the respective accumulation rates between two sites to be a little smaller than 2. Therefore, we apply constrained stepping as presented by Sakoe and Chiba (1978) such that each value of one data set can be fit to at most two values of the other. This is obtained by

$$\underline{\mathbf{D}}[i, j] = \begin{cases} \|S[i] - T[j]\| + \min(\underline{\mathbf{D}}[i, j-1], \underline{\mathbf{D}}[i-1, j-1], \underline{\mathbf{D}}[i-1, j]) & \text{for } i = 1 \text{ or } j = 1 \\ \|S[i] - T[j]\| + \min \left(\begin{array}{l} \|S[i-1] - T[j]\| + \underline{\mathbf{D}}[i-2, j-1] \\ \underline{\mathbf{D}}[i-1, j-1] \\ \|S[i] - T[j-1]\| + \underline{\mathbf{D}}[i-1, j-2] \end{array} \right) & \text{else} \end{cases} \quad (5)$$

Figure 3 illustrates the different patterns for proceeding through the matrix. Here, usage of cell $[i, j]$ refers to $S[i]$ being assigned to $T[j]$. In the aftermath, the backtracing has to occur according to the implemented stepping.

Finally, we do not only want to fit one type of data (e.g., densities) but combine the available information in the profiles to gain a robust picture of the developing stratigraphy along the traverse. In a first step, we match the $\delta^{18}\text{O}$ signal, which shows a clear seasonal behavior but almost no small-scale variations, as the high-frequency component is

C. F. Schaller et al.: North Greenland density profile

Table 2. Fitting parameters for our adaption of the DTW algorithm.

Property (step)	Step size (l)	Maximum surface offset (s)	Maximum bottom offset (b)
$\delta^{18}\text{O}$ (coarse)	3 cm	15 cm	75 cm
Density (fine)	0.1 cm	10 cm	10 cm

lost by diffusion. Then, we use the obtained depth assignment of the two different sites to resample the measured densities to a common depth scale. In a second step, we apply the algorithm to these densities at a much higher resolution to fine-tune our depth alignment according to small-scale stratigraphic features. As a norm we use the Euclidean distance divided by the path length (i.e., the root mean square error), which means that we have to keep track of the path lengths in a second matrix. Table 2 summarizes the final set of parameters. The maximum allowed offsets for the coarse fitting have been chosen according to the measured height of variations in the snow surface (e.g., dunes) and the maximum ratio of estimated accumulation rates. In the second step we allow for fine-tuning up to the maximum remaining shift, which was manually identified by aligning the vertical centers of the 2012 melt layers.

This method does not only allow us to compare data from two sites, but also to obtain a moving depth alignment by fitting the profiles to the first data set one by one. The result, a continuous image of the snow layering, can be compared with other indicators such as the melt layer positions. In addition, being able to align densities and stratigraphic features all along the traverse enables us to provide a representative density profile for the region. For its construction, we first use the continuous layering to transform all density curves to the first depth scale (NEEM) and average them. This, however, is not yet a representative density profile as all profiles now replicate the layering at NEEM; e.g., a layer that is very thin there but thicker at most sites would be considered thin. To overcome this, we calculate the mean shifts applied to the values that were aligned and thus averaged. On average, i.e., for constant accumulation rates, we would expect these shifts to go linear with depth for the layering to be representative. Thus we calculate a linear least squares regression and correct the depth accordingly.

Nonetheless, the depth scale still represents the accumulation rate at NEEM. To transfer the average profile to any location X in the sampling area of known accumulation (not necessarily one of the N2E sites), we need to calculate a linear rescaling factor f_X for the depth d_X that fulfills

$$d_{\text{NEEM}} = d_X \cdot f_X. \quad (6)$$

We expect f_X to be determined by the accumulation rate, or rather its ratio to the one at NEEM.

3.2 Significance testing and surrogate density profiles

Any alignment method will increase the covariance between records even if they are not related (Haam and Huybers, 2010). Therefore, to test the statistical significance of our density alignment, we generate sets of surrogate density profiles with similar statistical properties independently for each site and process them the same way as the original data. Alongside the artificial density profiles, the real $\delta^{18}\text{O}$ signals are used for the coarse fitting step.

The complexity of the density signal consisting of slow variations, sharp property changes as well as strong melt layer and wind-crust-related density spikes, inhibits the use of simple surrogate construction methods such as autoregressive processes. Instead we propose the following algorithm.

For each site, as a base curve, we identify the $\delta^{18}\text{O}$ component of the density signal by linear regression, using the same step size l_{low} as for the coarse ($\delta^{18}\text{O}$ -based) fitting step. This can be done because we rely on $\delta^{18}\text{O}$ to follow a seasonal cycle – otherwise water isotope dating would be impossible. Let ρ_{base} be the base density from $\delta^{18}\text{O}$, r_{low} the autocorrelation and σ_{base} the standard deviation of the fluctuations of the measured density (averaged to resolution l_{low}) around ρ_{base} for lag l_{low} . We start generating an artificial low-resolution density profile ρ_{low} by

$$\rho_{\text{low}}(z_i) = \rho_{\text{base}}(z_i) + \varepsilon_i \quad (7)$$

$$\varepsilon_i = \begin{cases} v_0 & \text{for } i = 0 \\ r_{\text{low}} \cdot \varepsilon_{i-1} + v_i & \text{else} \end{cases} \quad (8)$$

$$v \sim \mathcal{N}(0, \sigma_{\text{base}}), \quad (9)$$

where

$$z_i = z_0 + i \cdot l_{\text{low}}. \quad (10)$$

Here $v \sim \mathcal{N}(0, \sigma_{\text{base}})$ implies that the v_i are distributed normally with mean zero and standard deviation σ_{base} . In the following, $\mathcal{U}(0, 1)$ will represent a continuous uniform distribution for the interval $[0, 1]$. The inclusion of higher autocorrelation lengths is straightforward. r_{low} has to be replaced by the autocorrelation matrix, which is multiplied by a vector of the preceding ε_i . Second, on the fine scale (step size l_{high}), we have a look at the differences between the interpolated low-resolution density and the high-resolution density values from the measurements. As we find the distribution to be trimodal, we split the differences into three components – low amplitude variations within snow of similar properties (henceforth denoted “noise” even though they might partly have physical origin), fast and moderate amplitude changes in the density due to layering or wind crusts (“shocks”) and rapid high amplitude changes at melt layers (“melt”). Again, we compute the autocorrelation factor r_{high} for lag l_{high} . Nonetheless, this time, the standard deviations σ_{noise} , σ_{shocks} and σ_{melt} and the means μ_{shocks} and μ_{melt} have to be calculated separately. Furthermore we need to estimate

the probabilities P_{shocks} and P_{melt} of beginning a shock or a melt layer at a specific position. For this purpose, we determine the number of melt layers N_{melt} , the number of shocks N_{shocks} and the average distance to the previous shock d_{avg} . In addition, we denote the total number of data points by N and the distance to the last shock at a given position i by d_i . Finally, the basic model to generate a random density profile ρ_{high} is

$$\rho_{\text{high}}(z_i) = \rho_{\text{low}}(z_i) + \kappa_i \quad (11)$$

$$\kappa_i = \begin{cases} \phi_i & \text{for } i = 0 \text{ or } P > P_{\text{melt}} + P_{\text{shocks}} \\ \mathcal{N}(\mu_{\text{shocks}}, \sigma_{\text{shocks}}) & \text{for } i \neq 0 \text{ and } P_{\text{melt}} < P \leq P_{\text{melt}} + P_{\text{shocks}} \\ \mathcal{N}(\mu_{\text{melt}}, \sigma_{\text{melt}}) & \text{for } i \neq 0 \text{ and } P \leq P_{\text{melt}} \end{cases} \quad (12)$$

$$P_{\text{melt}} = \frac{N_{\text{melt}}}{N} \quad (13)$$

$$P_{\text{shocks}} = \frac{d_i}{d_{\text{avg}}} \cdot \frac{N_{\text{shocks}}}{N} \quad (14)$$

$$P \sim \mathcal{U}(0, 1) \quad (15)$$

$$\phi_i = \begin{cases} v_0 & \text{for } i = 0 \\ r_{\text{high}} \cdot \phi_{i-1} + v_i & \text{else} \end{cases} \quad (16)$$

$$v \sim \mathcal{N}(0, \sigma_{\text{base}}), \quad (17)$$

where

$$z_i = z_0 + i \cdot l_{\text{high}}. \quad (18)$$

The same approach as before can be used to expand to higher autocorrelation lengths. However, we use the model in the presented form as it already provides realistic density surrogates.

4 Results

4.1 Profile alignment

As an example of the matching process, we present a fit of data from N2E_11 to the first site (NEEM) in Fig. 4. The distance between the two locations is about 240 km, i.e., a little more than half of the total traverse length. First the $\delta^{18}\text{O}$ profiles are matched, yielding an approximately linearly increasing coarse shift. In the second step the densities are fine-tuned, which results in small shifts fluctuating around zero and never reaching the allowed maximum of 0.1 m. To provide an overview of the changing snow structure, we fitted all combinations of profiles from two sites and plotted the matrix of the root mean square errors (RMSEs) in Fig. 5. A remarkable change in the pattern of the fitting errors occurs between the fourth and fifth site along the traverse.

Figure 6 shows the continuous depth alignment obtained by fitting all liners along the traverse to the first site (NEEM). There were no notable differences when another location (e.g., EGRIP) was chosen as the reference or the fitting was done consecutively. For comparison, the melt layer positions detected during the CT measurements (cf. Table 3)

1996

C. F. Schaller et al.: North Greenland density profile

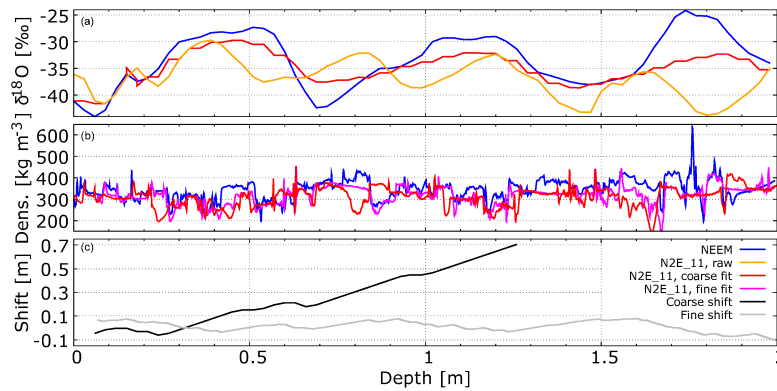


Figure 4. Alignment of the data from NEEM and N2E_11. **(a)** First, the raw $\delta^{18}\text{O}$ data from N2E_11 (orange) are fit to those of NEEM (blue) resulting in the red curve. **(b)** Then, the calculated (coarse) shifts are applied to the raw N2E_11 density data to obtain the red curve as an input for a second alignment with the raw NEEM density profile (blue). We end up with the pink curve as a final result. **(c)** The applied coarse (black) and fine (gray) shifts.

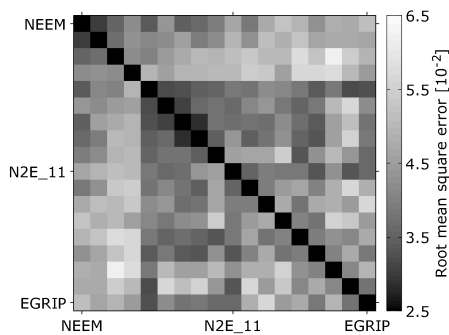


Figure 5. Root mean square matrix of the density alignment. The n th field in the m th row refers to the error of fitting data from the n th and m th liner. The darker the color, the lower the error and therefore the higher the agreement. The most notable change in snow structure can be observed between the fourth and the fifth column (or row).

have been included. In addition, selected density profiles are displayed. Using the previously calculated depth alignment, density records were stacked to obtain a representative density profile (Fig. 7). The gray area indicates a 1 standard deviation error band. Comparing the necessary rescaling factors (known from the construction of the stacked profile) to the ratio of accumulation rates, we apply linear least squares to find

$$f_X = 0.325 + 0.665 \cdot \frac{\dot{a}_{\text{NEEM}}}{\dot{a}_X}, \quad (19)$$

where \dot{a}_X denotes the mean annual accumulation rate at site X . The coefficient of determination is $R^2 = 0.82$.

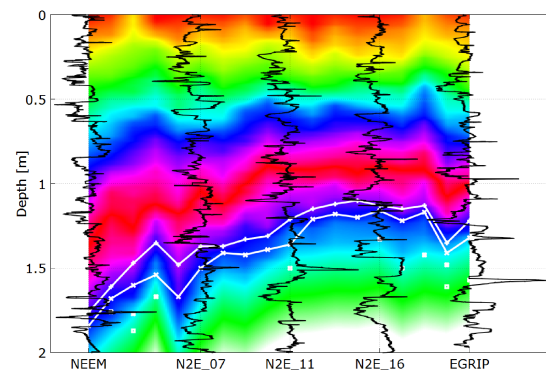


Figure 6. Continuous depth alignment, example density profiles and melt layers. A color map was applied uniformly at the first site (NEEM) and then transformed the same way as the depths were assigned. Thus snow within the same color band was matched during the fitting process. Linear interpolation was used between the sampled sites. In black, measured density profiles for the labeled locations are shown at the same scale, centered around their respective mean values. The white lines and points indicate the melt layer positions detected from the CT scans (cf. Table 3).

At the base resolution of 0.1 cm we find a mean shared variance of $R^2 = 0.56$ between the average and the individual density profiles. It can be increased by smoothing and obtains a maximum of $R^2 = 0.71$ when using a 4.3 cm moving average. In comparison, for 1000 randomly generated density data sets (e.g., Fig. 8), the respective stacked profiles share an average of $R^2 = 0.44$ with their components at base resolution. The maximum is $R^2 = 0.61$. We determine a p value (probability of finding such high R^2 by chance) of 0.015 for

C. F. Schaller et al.: North Greenland density profile

1997

Table 3. Melt layers, the water isotopic season of origin for the surrounding snow and mean annual accumulation rates for each site. The given depths indicate the vertical center of the respective melt layer. The upper two melt layers are always located in snow from summer 2012. For the lower ones, the season of origin for the surrounding snow is given, where S indicates summer and W winter. The accumulation rates are annual mean values for all available years at the particular location.

Site	Depth 1 [m]	Depth 2 [m]	Depth 3 [m]	Snow origin	Depth 4 [m]	Snow origin	Accumulation [kg m ⁻² a ⁻¹]
NEEM	1.76	1.84					224.69
N2E_03	1.61	1.68	1.76	S2012			193.8
N2E_04	1.47	1.60	1.77	W11/12	1.87	W11/12	205.04
N2E_05	1.35	1.54	1.67	W11/12			171.55
N2E_06	1.48	1.67					193.46
N2E_07	1.37	1.50					165.38
N2E_08	1.37	1.41					162.67
N2E_09	1.33	1.42					155.85
N2E_10	1.31	1.39					135.01
N2E_11	1.21	1.36	1.50	W11/12			137.58
N2E_12	1.15	1.21					124.73
N2E_14	1.12	1.18					117.30
N2E_15	1.10	1.20					126.78
N2E_16	1.13	1.16	1.33	W11/12			115.06
N2E_17	1.19	1.23	1.50	W11/12			129.88
N2E_19	1.13	1.17	1.42	S2011			132.16
N2E_20	1.35	1.41	1.48	W11/12	1.61	S2011	145.93
EGRIP	1.22	1.32	1.57	W11/12			139.57

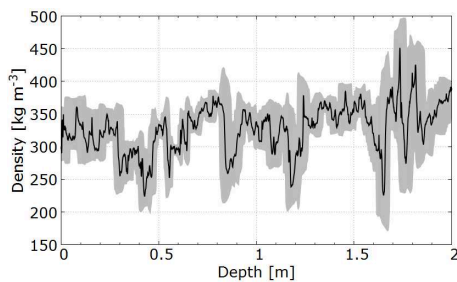


Figure 7. Representative density profile for the traverse region. The gray area indicates a 1 standard deviation error band in both x and y directions as there are uncertainties in the depth alignment as well as the averaged densities of all sites. Here, the depth scale was adjusted to the NEEM accumulation rate and has to be rescaled according to the accumulation rate for different sites.

the measured profiles within the distribution; i.e., the high shared variance of the measured profiles is statistically significant.

4.2 Raw densities, isotope extrema and accumulation rates

For all sites we find at least two melt layers in the snow isotopically dating back to the summer of 2012. In addition, some liners show melt layers which are surrounded by snow dating to winter 2011/2012 or summer 2011. For an overview

of all melt layers, see Table 3 or Fig. 6. From the raw density profiles, we obtain Fig. 9, which shows the average densities of the top meter and decimeter, which do not contain any prominent melt layers. The density in the top meter tends to decrease from the maximum of 332 kg m^{-3} at NEEM down to a minimum of 297 kg m^{-3} roughly 150 km from EGRIP before slightly increasing again. For 15 out of 18 sites the surface density is higher; nonetheless both parameters evolve similarly along the traverse.

Table 3 displays the mean annual accumulation rates along the traverse. Starting with a maximum of $225 \text{ kg m}^{-2} \text{ a}^{-1}$ at NEEM, the values steadily decrease down to the minimum of $115 \text{ kg m}^{-2} \text{ a}^{-1}$ about 100 km from EGRIP before increasing again to $140 \text{ kg m}^{-2} \text{ a}^{-1}$ at EGRIP. Comparing average values for the different years, there is neither a trend nor considerable variations in the accumulation rate (cf. Table 4). However, we observe much higher differences between successive years within the same core (average change $34.67 \text{ kg m}^{-2} \text{ a}^{-1}$), where we mainly see alternating behavior of high- and low-accumulation years.

Of the 5 years contained in our data, 2012 had the isotopically warmest summer for 83 % of the sites. At the three remaining locations (N2E_11, N2E_16 and EGRIP), the highest $\delta^{18}\text{O}$ values occur in 2014. For the winters, 2014/2015 was isotopically coldest in 51 % of the cases, 2011/2012 in 19 % and 2010/2011 in 30 %. Regarding annual $\delta^{18}\text{O}$ averages of all available sites (Table 4), we also find the highest $\delta^{18}\text{O}$ values for 2012.

1998

C. F. Schaller et al.: North Greenland density profile

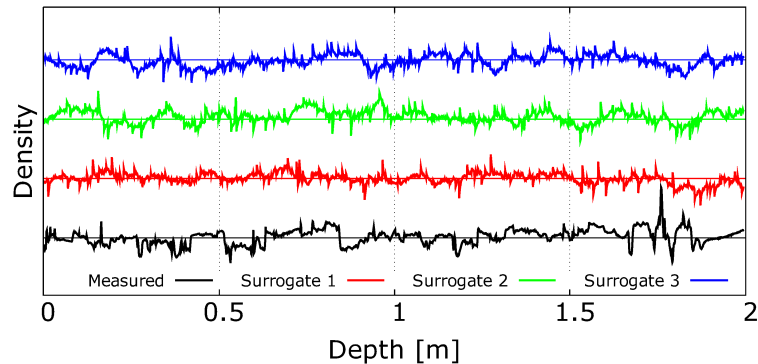


Figure 8. The measured density profile and three surrogates for the first site (NEEM). The artificial profiles are based on the seasonal $\delta^{18}\text{O}$ component of the density and have the same statistical properties as the original curve. Each profile is displayed at the same scale and has been centered around its mean.

Table 4. Mean deviations of the given year from the average local annual (winter-to-winter) accumulation rate and $\delta^{18}\text{O}$. For each year, data from all available sites were used.

Year	\dot{a} anomaly [$\text{kg m}^{-2} \text{a}^{-1}$]	$\delta^{18}\text{O}$ anomaly [‰]	Unavailable sites
2014	-2.66	-0.88	-
2013	5.26	-1.25	-
2012	3.20	3.64	NEEM, N2E_06
2011	-7.37	-2.31	NEEM, N2E_03–N2E_09

4.3 Linking accumulation, $\delta^{18}\text{O}$ and density

Comparing the annual average $\delta^{18}\text{O}$ values with the accumulation rates we obtain Fig. 10. Positive linear relations were fit to the data of 2012, 2013 and 2014 respectively, showing that within 1 year higher temperatures coincide with higher accumulation. The coefficient of determination is highest for 2012, while we have larger spreads for the other 2 years, in particular 2013.

To relate the density with the seasonal, low-frequency $\delta^{18}\text{O}$ signal at NEEM, we applied a 10 cm running mean to the stacked high-resolution density profile in Fig. 11. On average, snow with a high $\delta^{18}\text{O}$ value (considered summer snow) has a low density and the other way around. The only exception is the summer of 2012, where we find high-density values in summer, too.

5 Discussion

5.1 New methodology

The liner technique allows us to retrieve non-disturbed snow samples from the field and thereby conduct lab-based analysis (such as high-resolution density measurements) to gain

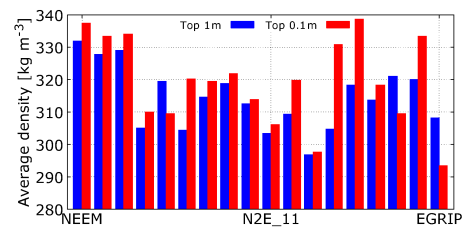


Figure 9. Average densities along the traverse through North Greenland (May 2015) in the top 1 and 0.1 m derived from CT data.

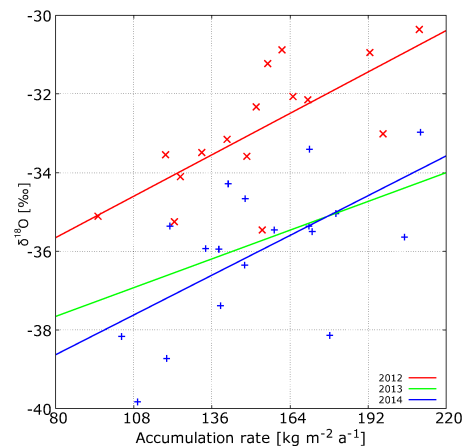


Figure 10. $\delta^{18}\text{O}$ signal vs. accumulation rate for the years 2012–2014. The lines were obtained by linear least squares fitting with coefficients of determination of $R^2 = 0.52$ for 2012, $R^2 = 0.27$ for 2013 and $R^2 = 0.37$ for 2014. The data points for 2013 show the largest spread and were omitted for clarity.

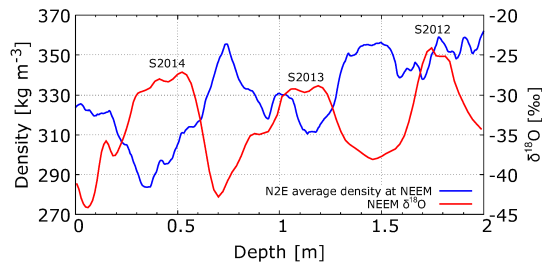


Figure 11. Comparison of the NEEM $\delta^{18}\text{O}$ signal with the stacked density profile on the NEEM depth scale smoothed using 10 cm running means. The summer maxima for 2012–2014 were marked.

further insight in the development of physical snow properties over large distances. This is a major improvement compared to previous methods, e.g., for measuring snow density, which was so far mainly done by weighing a known volume of snow where we have a trade-off of accuracy (bulk density) and resolution (density cutters). Both horizontal resolution and vertical depth can be adjusted to fit the needs of the respective study.

Figure 4 illustrates that we are able to align $\delta^{18}\text{O}$ and density data down to small stratigraphic features very well over a distance of over 200 km. Along the traverse, one observes a clear change in the RMSE (cf. Fig. 5) and thereby the snow structure at the fourth site, indicated by significantly different fitting errors. This coincides with the location where the ice divide was left eastwards and thereby the traverse entered a different accumulation regime in agreement with the drainage systems given by Zwally et al. (2011).

Furthermore the continuous depth alignment agrees very well with the melt layer positions detected during the CT measurements (Fig. 6). Stratigraphic features are still well aligned over the complete traverse distance of almost 450 km. We obtain a clear picture of the layering of the snowpack along the traverse. In comparison to radar measurements, which are limited to centimeter vertical resolution but can resolve annual layers down to 12 m (Hawley et al., 2006), we can give a much more precise picture and observe small-scale structures like wind crusts. In exchange we are limited to shallower depths – the maximum we plan to access in the near future is 6 m in a trench at the EGRIP drilling site.

For rescaling the stacked profile to any location in the area with known annual accumulation, we obtain a linear relation of the depth factor with the ratio of accumulation rates. This is plausible because, on average, we find linearly increasing shifts for the matching. Furthermore we do not observe significant densification in the upper 2 m of the snowpack, and therefore the depth of snow from the same deposition event is primarily determined by the accumulation rate. In addition, the relation has a high coefficient of determination for the applied linear least squares.

As the stratigraphy does not seem to change remarkably along the traverse apart from the effect of the decreasing accumulation rate, we consider the profile in Fig. 7 to be representative of the whole traverse region, potentially even most of North Greenland. For the given error band, there is an overlap of uncertainty in the depth alignment (x direction) with the uncertainty in density (y direction). The former is mainly caused by the variability of the snow mass accumulated from a single deposition event. Regarding the latter, the average density of the snowpack greatly varies as can be seen in Fig. 9. Thus, for the second meter, even though it is contained in the uncertainty band, we do not expect a straight line, but rather an alternation of high- and low-density layers similar to the upper meter.

A statistical test using surrogate density profiles shows that the high shared variance of the measured profiles is statistically significant ($p = 0.015$), even though the actual difference in numbers is quite small. This underlines that the density alignment provides additional information as we tried to use the most realistic surrogates (original $\delta^{18}\text{O}$ signal, seasonal cycle, three component stratigraphy model). Furthermore, a coefficient of determination of $R^2 = 0.56$ between the stacked and the individual profiles shows how much of the layering does reappear. Smoothing increases R^2 as it steadily transforms the profile to the low-resolution density curve that shows seasonal behavior (see Fig. 11) while smaller local variations vanish.

5.2 Temporal and regional variability of snow properties

The vast majority of melt layers are found in snow dating back to the very warm summer of 2012 (Nghiem et al., 2012). Moreover, above most of the melt layers within older snow, we find clear signs of percolation (cf. Fig. 2). Therefore we assume that 2012 was the only year in the period 2010–2015 with significant melt occurring in the observed area. From Fig. 9 we can infer that on the one hand, the average density of the snow in the top 2 m at a certain location can already be deduced from the surface density. On the other hand, the surface snow in May is among the denser ones within the year, thereby rather representing a spring or even winter signal than a summer one (compare Fig. 11). Furthermore we are able to visually identify many layers of homogeneous density, often clearly separated by wind crusts, which seem to contain snow from single deposition events.

For the accumulation rate (see Table 3), the 1964–2005 average of $220 \text{ kg m}^{-2} \text{ a}^{-1}$ determined from the NEEM ice core (Steen-Larsen et al., 2011) agrees very well with the $225 \text{ kg m}^{-2} \text{ a}^{-1}$ that we obtain from the corresponding snow liner. In addition, both accumulation maps from field measurements (Bales et al., 2009) and regional climate models (Fettweis, 2007) show the same behavior towards the east. While Table 4 shows no significant interannual changes in the average accumulation rate for the study area, we observe

2000

high fluctuations in the local annual values, a feature consistent with the strong influence of stratigraphic noise in single profiles (Münch et al., 2016). These can be explained by the accumulation of every year compensating previous local variations in the snow surface before new structures are introduced by wind-induced drift and dunes. Nonetheless, they also might partly originate from the uncertainty of separating the years only according to the $\delta^{18}\text{O}$ extrema.

In the majority of cases we find the highest isotopic summer temperatures and average $\delta^{18}\text{O}$ values for 2012, underlining the exceptional warmth of this year. The values for 2014 indicate that it was still warmer than the other contained years, in particular 2010, which was formerly regarded as very warm (Harper et al., 2012). The picture for the winters is less clear. Indeed, we assume that the isotopic signal of the fresh snow from winter 2014/2015 might still change.

5.3 Relations of density, $\delta^{18}\text{O}$ and accumulation rate

We find a positive linear relationship of annual mean $\delta^{18}\text{O}$ and accumulation rate (Fig. 10) with similar slopes for 2012 and 2014. This relation might partly originate from the changing surrounding conditions (e.g., elevation) along the traverse. The offset between the years could potentially be caused by the very high temperatures and the consequential surface melting in 2012 as we find the relation for 2013 to be a lot closer to 2014 than 2012. The dependence of the offset on the annual mean temperature (which is quite similar along the traverse) could explain why previous attempts to link both parameters by averaging data from several years (e.g., Weißbach et al., 2016) show results that are less clear.

We observe a clear anticorrelation of low-resolution density and $\delta^{18}\text{O}$ in Fig. 11. This agrees with the widely accepted conceptual model of Shimizu (1964), which states that snow has lower densities in summer and higher ones in winter. The main causes given are the increased packing due to stronger winds in winter and the larger size of precipitation particles in summer. For the summer of 2012, the high average densities are caused by the prominent melt layers, superimposing the original signal of the snow.

6 Summary and conclusions

We introduced the liner technique, which allows the very efficient retrieval of high-quality samples from the upper meters of the snowpack. To support this new sampling technique, we adapted a robust fitting algorithm from acoustic signal processing for the diverse data sets produced by such studies. This enables us to identify characteristic changes in the snowpack according to surrounding conditions as well as to generate continuous depth alignment using features from all available records.

To demonstrate their feasibility we applied the described methods to the upper 2 m of snow along a traverse in North

C. F. Schaller et al.: North Greenland density profile

Greenland. We obtain a record up to May 2015 of the depths of the 2012 melt layers and submillimeter-resolution densities. By combining these with $\delta^{18}\text{O}$ measurements, which indicate temperature, we are able to reconstruct accurate accumulation rates for the years 2010–2014 along a distance of about 400 km.

We combine isotope and density data as inputs for the matching algorithm. Thereby we are able to identify the different accumulation regimes along the traverse and resolve the continuous stratigraphy of the snow over the whole distance. This allows us to create a representative density profile for the study area, whose quality is proven by comparison with randomly generated data based on a statistical density model. The profile is available at a resolution of 0.1 cm and only has to be rescaled according to accumulation rate. Thus it is ready to act as a benchmark for snowpack models or be applied for the conversion of volume to mass and the detection of strong density gradients as potential reflectors in remote sensing (compare e.g., Hurkmans et al., 2014).

The success of fitting density and isotope profiles over hundreds of kilometers shows that even though there is a local component in the snow stratigraphy (e.g., layer thickness, average density), the general pattern is dominated by non-local processes in North Greenland. We assume that an important factor for that is the origin of weather and precipitation as air masses dominantly move in from the west to the east (Chen et al., 1997).

We observe large interannual accumulation variations locally but almost none on average, which can be explained by the smoothing of the surface by accumulation before new surface structures are caused by dunes and drift. The exceptionally warm summer of 2012 is clearly visible in the water isotope data; additionally 2014 shows the second highest summer values of $\delta^{18}\text{O}$ within the study period.

Relating the various snow properties, we find a distinct anticorrelation of smoothed density and $\delta^{18}\text{O}$ in accordance with previous literature. Furthermore we deduce a positive linear relation between $\delta^{18}\text{O}$ and accumulation rate, whose slope seems to be constant for the period considered, while the offset varies between the years, and thus might be temperature-dependent. This, however, poses the question as to whether models commonly used in the dating of deep ice cores (e.g., Parrenin et al., 2007, for the EPICA Dome C ice core) do correctly reconstruct accumulation rates from the $\delta^{18}\text{O}$ values, especially for times with significantly differing annual mean temperatures such as glacial.

Future work should include the automatic recognition of wind crusts and layering from CT images and the application of the described methods on different scales for both Antarctica and Greenland to gain further insight into the variability of physical properties in the snowpack.

7 Data and code availability

All measurement data will be uploaded to the open-access library PANGAEA[®]. If you are interested in using our implementation of the described algorithms, please contact the main author.

Author contributions. Sepp Kipfstuhl took the samples and initiated the analysis process. Hans Christian Steen-Larsen was involved in the field planning and helped interpret the results with his expertise in the Greenland snowpack. Johannes Freitag originally established the CT method, supervised and evaluated the isotope measurements and regularly discussed preliminary results with the main author. Olaf Eisen helped to relate the results to the literature and provided insights on alternative methods. Thomas Laepple recommended underlining the results with randomly generated data and suggested possible approaches. Christoph Schaller coordinated the CT measurements, evaluated and analyzed the combined data and prepared this manuscript. It was reviewed by all coauthors.

Acknowledgements. The main author wants to thank the German National Merit Foundation (Studienstiftung des deutschen Volkes e.V.) for funding his PhD project, York Schломann for conducting the isotope measurements and the CIC employees involved for organizing and supporting the traverse. We gratefully acknowledge the work of two anonymous referees and the editor, Joel Savarino.

The article processing charges for this open-access publication were covered by a research centre of the Helmholtz Association.

Edited by: J. Savarino

Reviewed by: two anonymous referees

References

- Bales, R. C., Guo, Q., Shen, D., McConnell, J. R., Du, G., Burkhart, J. F., Spikes, V. B., Hanna, E., and Cappelen, J.: Annual accumulation for Greenland updated using ice core data developed during 2000–2006 and analysis of daily coastal meteorological data, *J. Geophys. Res.*, 114, D06116, doi:10.1029/2008JD011208, 2009.
- Bennartz, R., Shupe, M. D., Turner, D. D., Walden, V. P., Steffen, K., Cox, C. J., Kulie, M. S., Miller, N. B., and Pettersen, C.: July 2012 Greenland melt extent enhanced by low-level liquid clouds, *Nature*, 496, 83–86, doi:10.1038/nature12002, 2013.
- Benson, C. S.: Stratigraphic studies in the snow and firn of the Greenland Ice sheet, *USA SIPRE Res. Rep.*, 70, 1–89, 1962.
- Bull, C.: Snow Accumulation in North Greenland, *J. Glaciol.*, 3, 237–248, 1958.
- Chen, Q.-S., Bromwich, D. H., and Bai, L.: Precipitation over Greenland Retrieved by a Dynamic Method and Its Relation to Cyclonic Activity, *J. Climate*, 10, 839–870, 1997.
- Fettweis, X.: Reconstruction of the 1979–2006 Greenland ice sheet surface mass balance using the regional climate model MAR, *The Cryosphere*, 1, 21–40, doi:10.5194/tc-1-21-2007, 2007.
- Fisher, D. A., Reeh, N., and Clausen, H. B.: Stratigraphic noise in the time series derived from ice cores, *Ann. Glaciol.*, 7, 76–83, 1985.
- Freitag, J., Kipfstuhl, S., and Laepple, T.: Core-scale radioscopic imaging: a new method reveals density-calcium link in Antarctic firn, *J. Glaciol.*, 59, 1009–1014, 2013.
- Haam, E. and Huybers, P.: A test for the presence of covariance between time-uncertain series of data with application to the Dongge Cave speleothem and atmospheric radiocarbon records, *Paleoceanography*, 25, PA2209, doi:10.1029/2008PA001713, 2010.
- Hagemuller, P. and Pilloix, T.: A New Method for Comparing and Matching Snow Profiles, Application for Profiles Measured by Penetrometers, *Front. Earth Sci.*, 4, 52, doi:10.3389/feart.2016.00052, 2016.
- Hanna, E., Huybrechts, P., Cappelen, J., Steffen, K., Bales, R. C., Burgess, E., McConnell, J. R., Steffensen, J. P., Van den Broeke, M., Wake, L., Bigg, G., Griffiths, M., and Savas, D.: Greenland Ice Sheet surface mass balance 1870 to 2010 based on Twentieth Century Reanalysis, and links with global climate forcing, *J. Geophys. Res.*, 116, D24121, doi:10.1029/2011JD016387, 2011.
- Harper, J., Humphrey, N., Pfeffer, W. T., Brown, J., and Fettweis, X.: Greenland ice-sheet contribution to sea-level rise buffered by meltwater storage in firn, *Nature*, 491, 240–243, doi:10.1038/nature11566, 2012.
- Hawley, R. L., Morris, E. M., Cullen, R., Nixdorf, U., Shepherd, A. P., and Wingham, D. J.: ASIRAS airborne radar resolves internal annual layers in the dry-snow zone of Greenland, *Geophys. Res. Lett.*, 33, L04502, doi:10.1029/2005GL025147, 2006.
- Hawley, R. L., Courville, Z. R., Kehrl, L. M., Lutz, E. R., Osterberg, E. C., Overly, T. B., and Wong, G. J.: Recent accumulation variability in northwest Greenland from ground-penetrating radar and shallow cores along the Greenland Inland Traverse, *J. Glaciol.*, 60, 375–382, doi:10.3189/2014JoG13J141, 2014.
- Hurkmans, R. T. W. L., Bamber, J. L., Davis, C. H., Joughin, I. R., Khvorostovsky, K. S., Smith, B. S., and Schoen, N.: Time-evolving mass loss of the Greenland Ice Sheet from satellite altimetry, *The Cryosphere*, 8, 1725–1740, doi:10.5194/tc-8-1725-2014, 2014.
- Itakura, F.: Minimum prediction residual principle applied to speech recognition, *IEEE T. Acoust. Speech*, 23, 67–72, 1975.
- Koenig, L. S., Ivanoff, A., Alexander, P. M., MacGregor, J. A., Fettweis, X., Panzer, B., Paden, J. D., Forster, R. R., Das, I., McConnell, J. R., Tedesco, M., Leuschen, C., and Gogineni, P.: Annual Greenland accumulation rates (2009–2012) from airborne snow radar, *The Cryosphere*, 10, 1739–1752, doi:10.5194/tc-10-1739-2016, 2016.
- Lenton, T. M., Held, H., Kriegler, E., Hall, J. W., Lucht, W., Rahmstorf, S., and Schellnhuber, H. J.: Tipping elements in the Earth's climate system, *P. Natl. Acad. Sci. USA*, 105, 1786–1793, 2008.
- McConnell, R., Kwok, R., Curlander, J., Kober, W., and Pang, S.: psi-s correlation and dynamic time warping: two methods for tracking ice floes in SAR images, *IEEE T. Geosci. Remote*, 29, 1004–1012, doi:10.1109/36.101377, 1991.
- Münch, T., Kipfstuhl, S., Freitag, J., Meyer, H., and Laepple, T.: Regional climate signal vs. local noise: a two-dimensional view

2002

- of water isotopes in Antarctic firn at Kohnen Station, Dronning Maud Land, *Clim. Past*, 12, 1565–1581, doi:10.5194/cp-12-1565-2016, 2016.
- Nghiem, S. V., Hall, D. K., Mote, T. L., Tedesco, M., Albert, M. R., Keegan, K., Shuman, C. A., DiGirolamo, N. E., and Neumann, G.: The extreme melt across the Greenland ice sheet in 2012, *Geophys. Res. Lett.*, 39, L20502, doi:10.1029/2012GL053611, 2012.
- Nilsson, J., Vallelonga, P., Simonsen, S. B., Sorensen, L. S., Forsberg, R., Dahl-Jensen, D., Hirabayashi, M., Goto-Azuma, K., Hvidberg, C. S., Kjaer, H. A., and Satow, K.: Greenland 2012 melt event effects on CryoSat-2 radar altimetry, *Geophys. Res. Lett.*, 42, 3919–3926, doi:10.1002/2015GL063296, 2015.
- Parrenin, F., Barnola, J.-M., Beer, J., Blunier, T., Castellano, E., Chappellaz, J., Dreyfus, G., Fischer, H., Fujita, S., Jouzel, J., Kawamura, K., Lemieux-Dudon, B., Loulergue, L., Masson-Delmotte, V., Narcisi, B., Petit, J.-R., Raisbeck, G., Raynaud, D., Ruth, U., Schwander, J., Severi, M., Spahni, R., Steffensen, J. P., Svensson, A., Udisti, R., Waelbroeck, C., and Wolff, E.: The EDC3 chronology for the EPICA Dome C ice core, *Clim. Past*, 3, 485–497, doi:10.5194/cp-3-485-2007, 2007.
- Sakoe, H. and Chiba, S.: Dynamic programming algorithm optimization for spoken word recognition, *IEEE T. Acoust. Speech*, 26, 43–49, doi:10.1109/TASSP.1978.1163055, 1978.
- Sakurai, Y., Faloutsos, C., and Yamamuro, M.: Stream monitoring under the time warping distance, *Proc. Int. Conf. Data*, 23, 1046–1055, doi:10.1109/ICDE.2007.368963, 2007.
- Senin, P.: Dynamic time warping algorithm review, Tech. rep., University of Hawaii, Honolulu, USA, 2008.
- Shimizu, H.: Glaciological Studies in West Antarctica 1960–1962, in: *Antarct. Res. Ser.*, edited by: Mellor, M., American Geophysical Union, Washington, D.C., 37–64, 1964.
- Steen-Larsen, H. C., Masson-Delmotte, V., Sjolte, J., Johnsen, S. J., Vinther, B. M., Breon, F.-M., Clausen, H. B., Dahl-Jensen, D., Falourd, S., Fettweis, X., Gallee, H., Jouzel, J., Kageyama, M., Lerche, H., Minster, B., Picard, G., Punge, H. J., Risi, C., Salas, D., Schwander, J., Steffen, K., Sveinbjornsdottir, A. E., Svensson, A., and White, J.: Understanding the climatic signal in the water stable isotope records from the NEEM shallow firn/ice cores in northwest Greenland, *J. Geophys. Res.*, 116, D06108, doi:10.1029/2010JD014311, 2011.
- Weißbach, S., Wegner, A., Opel, T., Oerter, H., Vinther, B. M., and Kipfstuhl, S.: Spatial and temporal oxygen isotope variability in northern Greenland – implications for a new climate record over the past millennium, *Clim. Past*, 12, 171–188, doi:10.5194/cp-12-171-2016, 2016.
- Zwally, H. J., Jun, L. I., Brenner, A. C., Beckley, M., Cornejo, H. G., DiMarzio, J., Giovinetto, M. B., Neumann, T. A., Robbins, J., Saba, J. L., Yi, D., and Wang, W.: Greenland ice sheet mass balance: distribution of increased mass loss with climate warming: 2003–07 versus 1992–2002, *J. Glaciol.*, 57, 88–102, 2011.

C. F. Schaller et al.: North Greenland density profile

Publication II

Schaller, C. F., Freitag, J., and Eisen, O.: Critical porosity of gas enclosure in polar firn independent of climate, *Climate of the Past*, 13, 1685–1693, <https://doi.org/10.5194/cp-13-1685-2017>, 2017

Clim. Past, 13, 1685–1693, 2017
<https://doi.org/10.5194/cp-13-1685-2017>
© Author(s) 2017. This work is distributed under
the Creative Commons Attribution 4.0 License.



Critical porosity of gas enclosure in polar firn independent of climate

Christoph Florian Schaller¹, Johannes Freitag¹, and Olaf Eisen^{1,2}

¹Alfred Wegener Institute, Helmholtz Centre for Polar and Marine Research, 27568 Bremerhaven, Germany

²Department of Geosciences, University of Bremen, 28359 Bremen, Germany

Correspondence to: Christoph Florian Schaller (christoph.schaller@awi.de)

Received: 14 July 2017 – Discussion started: 31 July 2017

Revised: 17 October 2017 – Accepted: 20 October 2017 – Published: 24 November 2017

Abstract. In order to interpret the paleoclimatic record stored in the air enclosed in polar ice cores, it is crucial to understand the fundamental lock-in process. Within the porous firn, bubbles are sealed continuously until the respective horizontal layer reaches a critical porosity. Present-day firn air models use a postulated temperature dependence of this value as the only parameter to adjust to the surrounding conditions of individual sites. However, no direct measurements of the firn microstructure could confirm these assumptions. Here we show that the critical porosity is a climate-independent constant by providing an extensive data set of micrometer-resolution 3-D X-ray computer tomographic measurements for ice cores representing different extremes of the temperature and accumulation ranges. We demonstrate why indirect measurements suggest a climatic dependence and substantiate our observations by applying percolation theory as a theoretical framework for bubble trapping. The incorporation of our results significantly influences the dating of trace gas records, changing gas-age–ice-age differences by up to more than 1000 years. This may further help resolve inconsistencies, such as differences between East Antarctic $\delta^{15}\text{N}$ records (as a proxy for firn height) and model results. We expect our findings to be the basis for improved firn air and densification models, leading to lower dating uncertainties. The reduced coupling of proxies and surrounding conditions may allow for more sophisticated reinterpretations of trace gas records in terms of paleoclimatic changes and will benefit the development of new proxies, such as the air content as a marker of local insolation.

1 Introduction

Air trapped in polar ice cores provides a unique opportunity for paleoclimatic studies (Legrand and Mayewski, 1997). In particular, it allows the reconstruction of the past chemical and isotopic composition of the atmosphere for up to 800 000 years (Jouzel et al., 2007; Loulergue et al., 2008). However, as bubbles are only isolated from the atmosphere at certain depth (the firn–ice transition – 50–120 m depending on the local conditions), the enclosed air is always younger than the surrounding ice. An accurate estimation of this gas-age–ice-age difference (Δage , up to 7000 years during glacial periods; Bender et al., 2006) is essential for the interpretation of ice-core records as otherwise phase relationships between ice and gas records cannot be determined correctly.

Thus, it is crucial to understand the fundamental processes in the porous firn (Schwander and Stauffer, 1984) – diffusion of air through the open pore space (Trudinger et al., 1997; Fabre et al., 2000) and the entrapment of air by pore closure due to firn densification, which is the main focus of this study. In a depth range referred to as the “lock-in zone”, gas enclosure within individual horizontal layers occurs at a critical porosity (Schwander et al., 1993). It is the only parameter in empirical relations of closed and total porosity (Schwander, 1989; Goujon et al., 2003) that are commonly used in present-day firn air models (Severinghaus and Battle, 2006; Mitchell et al., 2015). A temperature dependence of this value has been postulated (Raynaud and Lebel, 1979) and parametrized using air-content measurements (Martinerie et al., 1992). Nonetheless, the underlying microstructural processes are not well-understood and there is no confirmation of these assumptions by direct measurements of firn microstructure.

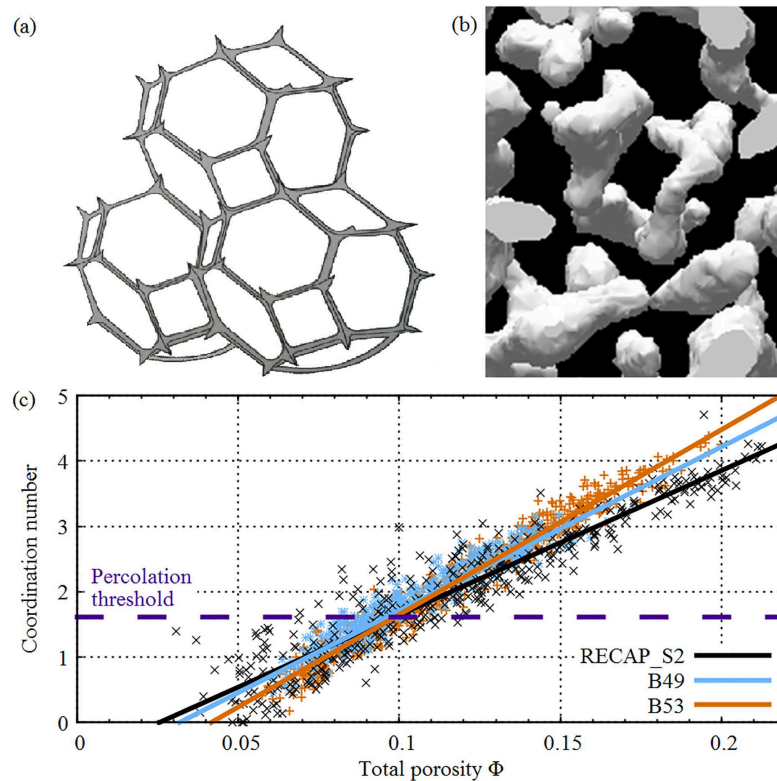


Figure 1. (a) A structure consisting of three packed tetrakaidecahedra. The white bodies represent ice crystals, the gray edges the pore network. (b) Example of a 3-D scan; the pore network is shown in white. (c) Coordination number versus total porosity for our measurements. The threshold for gas enclosure within a single layer as predicted by percolation theory has been marked.

Table 1. Details on the analyzed cores. Mean annual temperature is denoted by \bar{T} and an estimate of yearly accumulation by \dot{a} .

Drill site	Year	Elevation (m)	\bar{T} (°C)	\dot{a} (kg m ⁻² a ⁻¹)	Depth interval (m)	No. of data points
RECAP_S2 (Renland, Greenland) ¹	2015	2296	−18	460	49–73	246
B49 (Kohnen station, East Antarctica) ²	2012/13	2881	−44	65	73–90	303
B53 (Dome Fuji, East Antarctica) ²	2012/13	3726	−55	30	76–106	614

¹ Johnsen et al. (1992). ² Unpublished data, the accumulation rates are based on a preliminary volcanic layer dating.

The $\delta^{15}\text{N}$ of N_2 has been established as a proxy for firn height and thus an indirect constraint on Δage (Sowers et al., 1992). This relation has successfully been tested for high-accumulation sites, e.g., the last 40 000 years at Summit, Greenland (Schwander et al., 1997). On the contrary, there is a mismatch of up to 2000 years with model results for the East Antarctic plateau (Bender et al., 2006; Parrenin et al., 2012). These modeled chronologies are based on the current knowledge of bubble trapping in polar firn and are particularly sensitive to the critical porosity via the assumed temper-

ature dependence. Deviations from the simple relationships used to reconstruct past temperatures and accumulation rates from the water isotopic composition have been suggested as a possible explanation (Landais et al., 2006), while the hypothesis of a large glacial convective zone as an important factor has been ruled out (Capron et al., 2013). Recently, the inclusion of impurity effects has reduced the mismatch for East Antarctic sites; however, it reduces the agreement between modeled and measured $\delta^{15}\text{N}$ for high-accumulation sites (Breant et al., 2017).

Table 2. Results of least squares fitting our parametrization to the obtained data.

Data set	Φ_{crit}	λ_1	λ_2	b	R^2
RECAP_S2	0.1005	62.45	47.34	0.4816	0.9744
B49	0.0985	169.57	51.55	0.5797	0.9801
B53	0.1000	206.36	48.06	0.7072	0.9603

In this paper, we present the first extensive data set of direct firn microstructure measurements throughout the lock-in zone. We start off by using it to scrutinize the current knowledge of gas enclosure in polar firn and show why previous indirect measurements yielded different results. Then, we apply bond percolation theory (Enting, 1993) as a theoretical framework for our conclusions and demonstrate their agreement with other methods. Finally, we discuss changes in the dating and interpretation of trace-gas records that incorporation of our results in current firn air models will imply. The reduced coupling of proxies and surrounding conditions may allow for more sophisticated reinterpretations in terms of paleoclimatic changes and will benefit the development of new proxies, such as the air content as a marker of local insolation (Raynaud et al., 2007; Eicher et al., 2016).

2 Materials and methods

Firn microstructure throughout the lock-in zone has been deduced for ice cores from three locations (cf. Table 1) using a specifically designed X-ray microfocus computer tomograph in a cold lab (Freitag et al., 2013). For each 1 m core segment, we scanned a minimum number of five sections of approximately 4 cm height and the full core diameter (8–10 cm) with a focus on homogenous layers. One measurement consists of 3000 radioscopic images, which are used to tomographically reconstruct the 3-D microstructure at a resolution of approximately 25 μm (e.g., Fig. 1b). Consecutively, these reconstructions are segmented into ice and air using a two-step procedure consisting of a two-level Otsu's method (Otsu, 1979) followed by simple region growing for the ambiguous voxels. We adapted an existing algorithm (Nguyen et al., 2011) to determine the pore coordination number during the segmentation process. To eliminate the effect of cut pores at the surface of the sample (Martinerie et al., 1990), each data point (as referred to, e.g., in Table 1) corresponds to a layer of approximately 1 cm height and 6 cm diameter. Having the microstructure of the surrounding material in all directions at hand allows us to safely determine whether a pore is open or closed. For all measurements, the remaining cut pores were less than 0.1 % of the pore volume. For 10 repeat measurements of the same sample, both standard and maximum deviation of the total porosity are less than 1 %. Furthermore, the total porosities agree with those from bulk measurements and 2-D radioscopy with a maximum deviation of 3 %.

A well-known framework to model porous media is bond percolation theory (Broadbent and Hammersley, 1957). It enables us to predict the point at which a material becomes impermeable. The Kelvin structure (packed tetrakaidecahedra; see Fig. 1a) is space-filling with one of the lowest surface-area-to-volume ratios. It is well-studied and has for example been applied as a model for foam (Koehler et al., 1999). We use it to represent sintered ice grains. When packed, the grains align along a body-centered cubic lattice. Therefore, the air network corresponds to its dual lattice, which has a coordination number (average number of neighbors) of 4 when fully occupied. For this lattice, the fraction of channels occupied by air at gas enclosure, the so-called percolation threshold, is known to be 0.4031 (van der Marck, 1997). Thus, the predicted coordination number at the percolation threshold is $4 \cdot 0.4031 = 1.6124$. Notably, the influence of the chosen lattice is rather small (Wierman and Naor, 2003).

3 Results

Gas enclosure within a single layer occurs at the same critical porosity Φ_{crit} of about 0.1 for all cores (Fig. 2a). However, as indicated by the much steeper slope of the closed porosity, enclosure takes place in a significantly smaller porosity range for the East Antarctic cores compared to the coastal Greenland site. To fit our data, we derived a new local relation (Eq. 1) of closed porosity Φ_{cl} and total porosity Φ , where $b, \lambda_1, \lambda_2 \in \mathbb{R}_{\geq 0}$ and $b \leq 1$. The parameters of least squares fitting are given in Table 2.

$$\Phi_{\text{cl}} = \begin{cases} \Phi & \text{for } \Phi \leq \Phi_{\text{crit}} \\ \Phi_{\text{crit}} (b e^{-\lambda_1(\Phi - \Phi_{\text{crit}})} + (1 - b) e^{-\lambda_2(\Phi - \Phi_{\text{crit}})}) & \text{else} \end{cases} \quad (1)$$

Within the microstructure analysis for the B53 core, we also mimicked the sample properties (cylindrical shape, 5 cm diameter, 5 cm height) and the method (melting the sample under vacuum conditions, thus counting cut closed pores as part of the open pore space) as applied for Summit, Greenland (Schwander et al., 1993). This significantly changes the shape of the closed versus total porosity curve and yields results similar to previous studies (Fig. 2b). Then, by comparing with our original data (where cut pores are traced within a larger volume to determine whether they are open or closed), we determined the necessary correction factors for the effect of cut pores (Fig. 4).

For the coordination number (Fig. 1c) we observe a linear increase with total porosity for all three sites. At the critical porosity of about 0.1, we obtain very similar values of 1.65 ± 0.17 for B53, 1.7 ± 0.18 for B49 and 1.64 ± 0.24 for RECAP_S2 from linear regression.

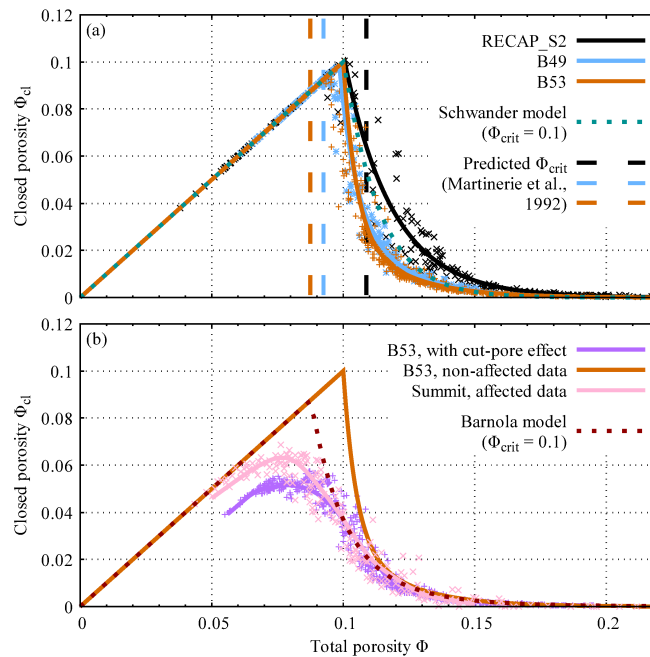


Figure 2. Closed versus total porosity for (a) the analyzed cores in comparison with commonly expected values and (b) B53 ignoring cut pores compared to previous results from Summit, Greenland (Schwander et al., 1993). The solid lines indicate least squares fits for the respective core, the short-dashed lines represent model results (Schwander, 1989; Goujon et al., 2003) for the given parameters, and the long-dashed lines mark the critical porosity values predicted by the previously observed temperature dependence (Martinerie et al., 1992).

4 Discussion

Even though the surrounding conditions differ significantly, we obtain the same critical porosity of about 0.1 for all cores (Fig. 2a, Table 2). In previous literature, average ice densities at air isolation were obtained from air-content measurements on deep ice samples (Martinerie et al., 1992). To allow for a better comparison with our results, we calculated the corresponding critical porosities (Fig. 3). For the gas enclosure within single layers, we do not observe the commonly assumed temperature dependence of Φ_{crit} . In contrast, we find strong evidence for a constant (and thus climate-independent) critical porosity.

In order to estimate the closed porosity in firn, previous studies relied on measuring the amount of air enclosed in a sample by melting it in a vacuum chamber. However, during vacuumization, air is not only removed from the open pore space but also cut closed pores, which is of particular importance for the more extensive pore network of the firn compared to deeper ice samples. The breaking of closed, but still fragile pores might even enhance this effect (Schwander and Stauffer, 1984). Nonetheless, to date, it has been neglected or only accounted for by multiplying with correction factors of up to 10% (first applied for firn in Appendix 2 of Mar-

tinierie et al., 1992; recently, Mitchell et al., 2015). Our estimation (Figs. 2b and 4) proves a serious underestimation of the cut-pore effect. This can be explained by a classical percolation phenomenon – near the percolation threshold, individual (clusters of) closed pores can be very large compared to single bubbles (Stauffer, 1979). Indeed, we observe extents of more than 1 cm near the critical porosity for all three cores.

In particular, our results confirm the existence of a critical porosity in contrast to recent assumptions of gas enclosure for a single layer occurring within a certain porosity range (Mitchell et al., 2015). Remarkably, for the correct critical porosity, the Schwander parametrization (Schwander, 1989) seems to approximately represent a site-independent average relation of closed and total porosity (cf. Fig. 2a). However, due to the lack of other parameters, it cannot fully reflect the behavior of polar firn. Therefore, we decided to derive a more complex exponential-decay relation (Eq. 1) to fit our results.

For all three cores, the observed coordination numbers at gas enclosure (Fig. 1c) are in agreement with the value predicted by percolation theory. We conclude that polar firn evolves towards the same “optimal” microstructure, driven by a universal percolation process (Enting, 1993). However,

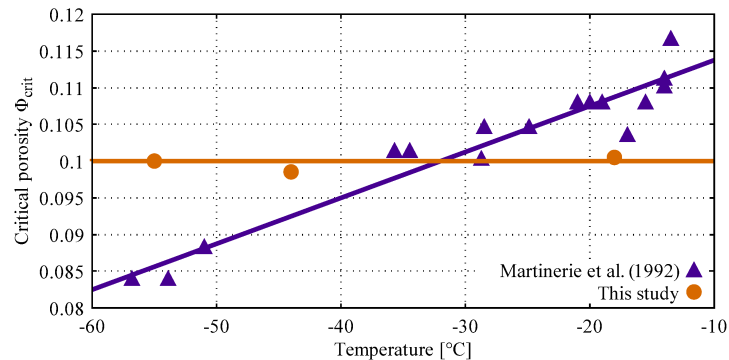


Figure 3. Critical porosity versus temperature. The given linear relation is commonly fit to the data of Martinerie et al. (1992), a study based on air-content measurements of 495 deep ice samples from 16 cores (with a minimum of only two measurements for one core). From their results, they reconstruct the average ice density at air isolation, which is equivalent to the porosities shown here. In contrast, we analyzed the microstructure of 1163 firn samples for three cores (see Table 1), allowing the direct determination of the critical porosity of gas enclosure within a single layer.

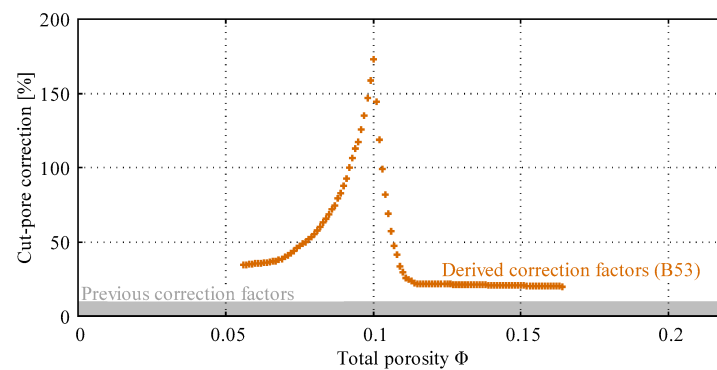


Figure 4. Necessary correction factors for the cut-pore effect assuming the B53 core would have been analyzed with the method used for Summit, Greenland (Schwander et al., 1993). The range of corrections applied in previous literature is indicated by the gray box.

the initial conditions differ as the firn is strongly influenced by the surrounding local conditions such as accumulation rate (affecting residence times at certain depth intervals) and temperature (as one of the main drivers for snow and firn metamorphism; Schneebeli and Sokratov, 2004).

The problem of understanding gas enclosure in polar firn has been tackled with different methods and from various perspectives such as firn microstructure, firn air transport and firn air pumpings. As a consequence, seemingly different definitions have been established for terminological frameworks such as the lock-in zone. The results of two firn air pumpings conducted at the RECAP drill site (T. Sowers, personal communication, 2017) and at Kohlen station, close to B49 (Weiler, 2008), in combination with high-resolution X-ray porosity measurements (Freitag et al., 2013) corroborate our microstructural findings. For both sites, the sharp decline in CO_2 , CH_4 and N_2O concentrations (interpreted as the on-

set of the lock-in zone according to firn air pumpings) coincides with the occurrence of the first significant (i.e., at least 1 cm thick) layer with a porosity below the critical value of 0.1. On the other hand, no more air can be pumped (bottom of the lock-in zone according to firn air pumpings) when there are no further layers with a total porosity larger than 0.1. In the firn air transport literature (e.g., Buizert and Severinghaus, 2016), the onset of the lock-in zone (also referred to as “lock-in depth”) is defined as the depth where molecular diffusion effectively ceases. According to percolation theory, this happens at the percolation threshold, i.e., the point when there is no longer a connected component of the order of the system size (Ghanbarian and Hunt, 2014). This corresponds to the first layer reaching a closed porosity of 100%, which is the onset of the lock-in zone in the microstructural sense. Regarding the bottom of the lock-in zone, it has been observed that due to vertical mixing, the air composition at a

1690

C. F. Schaller et al.: Gas enclosure in polar firn

certain depth no longer changes (definition according to gas transport) at the “close-off depth” (Buizert et al., 2012). It is defined as the depth at which all pores are closed (Witrant et al., 2012) and thereby also coincides with the bottom of the lock-in zone according to firn microstructure. Thus, the three definitions for the lock-in zone (according to firn microstructure, firn air transport and firn air pumpings) are equivalent. Furthermore, the limits of the lock-in zone are solely determined by the existence of significant layers above and below the critical porosity and thereby the (centimeter-scale) porosity variability.

While concepts such as gas enclosure (both in single layers and as a bulk property) occurring at a critical closed (Goujon et al., 2003) or open (Gregory et al., 2014) porosity have become widely accepted, they do not seem to agree with the results of our firn microstructure analysis and the previously discussed (conceptual) definitions of the lock-in zone. As a consequence, the refinement of these theories may greatly benefit the understanding of gas enclosure in polar firn. Notably, the critical closed porosity value of 37% identified by Jean-Marc Barnola using porosity measurements of several ice cores from Greenland and Antarctica (Goujon et al., 2003) corresponds to a total porosity of approximately 0.1 for the two data sets (Summit and B53) that are affected by the cut-pore effect (displayed in Fig. 2b).

Even though gas enclosure for a single layer occurs at the same critical porosity, sealed layers may have variable air contents. Above the close-off depth, we determine average coefficients of variation for the total porosity of 1.3% for B53, 1.8% for B49 and 2.5% for RECAP_S2. Higher porosity variability will lead to a larger amount of shallowly trapped pores, thereby increasing the air content V (Stauffer et al., 1985). In our case, the effect of shallow trapping can be estimated from the different slopes of the lock-in curves given in Fig. 2a, yielding possible increases in air content of about 2% for B49 and 8% for RECAP_S2 in comparison with B53. This implicitly assumes that closed and open porosity undergo the same compaction as the firn densifies and thus has to be interpreted as the maximum possible influence of shallow trapping. In addition, the lock-in zone extends over a depth range of approximately 7 m for B53, 9 m for B49 and 15 m for RECAP_S2. Larger lock-in zones are expected to cause enhanced sealing effects (i.e., permeable layers being sealed by impermeable ones above). This further increases the air content (Stauffer et al., 1985). However, the effect is hard to quantify as our measurements do not yield information about the spatial extent of horizontal layers, and it does not take into account pressure adjustment within the lock-in zone, which is happening on a much shorter timescale compared to diffusion (Buizert and Severinghaus, 2016). Nonetheless, it may explain the 8 and 27% larger air contents for B49 and RECAP_S2 (compared to B53), respectively, that V measurements for deep ice cores would predict according to the observed temperature dependence (Martinerie et al., 1992). In return, even though we do

not observe this temperature dependence for the gas enclosure within single layers, it is a signal that seems to originate from the lock-in zone, presumably as a consequence of a distinct density layering.

We conclude that V measurements may yield multiple-layer averages of pore volumes at gas enclosure. They should only be interpreted with great caution in regard to the sealing of single layers. The post-coring loss of enclosed air is an error source we can neither quantify nor rule out. For the Camp Century core, about 10% lower air contents were observed after 35 years of storage (Vinther et al., 2009), although a systematic error due to the different measurement setups is possible.

5 Implications

For the EDC core (East Antarctica), 86% of the variance in V cannot be explained by air pressure or temperature changes. An anticorrelation with local insolation was found and suggested as a new proxy (Raynaud et al., 2007). The same insolation signature was found for the V record of the NGRIP core (Greenland), but the underlying physical mechanisms are not yet resolved (Eicher et al., 2016). Based on our results, we rule out the idea of other properties influencing the porosity at gas enclosure for single layers as we do not even observe a temperature dependence. Instead, we suggest increased sealing effects and shallow trapping due to larger porosity variability of the layered snowpack as an explanation. Reasons for the enhanced layering may be changes in the atmospheric conditions, accumulation rate or impurity content, similar to the observed increase in layering during glacials (Augustin et al., 2004).

As indicated by $\delta^{15}\text{N}$ measurements as a proxy for firn height (Sowers et al., 1992), up-to-date firn air models seem to have difficulties to estimate past lock-in depths for the East Antarctic plateau (Landais et al., 2006; Capron et al., 2013) and to synchronize age dating of individual ice cores (Parrenin et al., 2012). We suggest that incorporation of our results will help to overcome these problems, as current approaches are based on temperature-dependent lock-in (Martinerie et al., 1992) and the Barnola model (Goujon et al., 2003). Exemplarily, we estimate the gas-age-ice-age difference for the Vostok ice core from the temperature (Jouzel et al., 1987) and accumulation rate (Parrenin et al., 2004) records using the Herron–Langway model (Herron and Langway, 1980). On average, excluding the temperature dependence of the critical porosity reduces the gas-age-ice-age difference by well over 10%. For the last glacial more than 1000 years of the 2000-year mismatch with $\delta^{15}\text{N}$ data (Bender et al., 2006) can be explained this way. We suggest a combination with the effect of impurities on firn densification (Freitag et al., 2013; Breant et al., 2017) as a promising approach to resolve the remaining mismatch. Other effects that are currently not well represented, such as stronger

C. F. Schaller et al.: Gas enclosure in polar firn

1691

layering during the glacials (Bendel et al., 2013), may further influence these values. We see this study as a catalyst for improved firn air and densification models, which will reduce dating uncertainties and allow for more sophisticated reinterpretations of the available trace gas records, in particular due to the reduced coupling to temperature.

Code and data availability. The data shown in the plots are available through the open-access library PANGAEA® (Schaller et al., 2017). If you are interested in using our implementation of the described algorithms or want to work with the raw data, please contact the main author.

Author contributions. JF was responsible for the development of the AWI ICE-CT and pointed out the opportunity for this study to CS. Three-dimensional measurements were carried out by JF for RECAP_S2 and CS for B49 and B53. The segmentation of the 3-D data sets and the evaluation of microstructural parameters was performed by CS, who researched and programmed the necessary algorithms. The results and their implications were discussed and related to the literature by all coauthors. CS prepared the initial manuscript, which was reviewed and improved by all coauthors.

Competing interests. The authors declare that they have no conflict of interest.

Acknowledgements. The authors want to acknowledge Sepp Kipfstuhl and Bo Vinther as those responsible for the drilling of B49/B53 and RECAP_S2, respectively, and Todd Sowers for providing an insight into the RECAP firn air data. The main author wants to thank the German National Merit Foundation (Studienstiftung des deutschen Volkes e.V.) for funding his PhD project. Last but not least, we are much obliged to Eric Wolff, Christo Buizert and an anonymous referee for their support in greatly improving this paper.

The article processing charges for this open-access publication were covered by a Research Centre of the Helmholtz Association.

Edited by: Eric Wolff

Reviewed by: Christo Buizert and one anonymous referee

References

- Augustin, L., Barbante, C., Barnes, P. R., et al.: Eight glacial cycles from an Antarctic ice core, *Nature*, 429, 623–628, 2004.
- Bendel, V., Ueltzhöffer, K. J., Freitag, J., Kipfstuhl, S., Kuhs, W. F., Garbe, C. S., and Faria, S. H.: High-resolution variations in size, number and arrangement of air bubbles in the EPICA DML (Antarctica) ice core, *J. Glaciol.*, 59, 972–980, <https://doi.org/10.3189/2013JoG12J245>, 2013.
- Bender, M. L., Floch, G., Chappellaz, J., Suwa, M., Barnola, J.-M., Blunier, T., Dreyfus, G., Jouzel, J., and Parrenin, F.: Gas age-ice age differences and the chronology of the Vostok ice core, 0–100 ka, *J. Geophys. Res.*, 111, D21115, <https://doi.org/10.1029/2005JD006488>, 2006.
- Breant, C., Martinerie, P., Orsi, A., Arnaud, L., and Landais, A.: Modelling firn thickness evolution during the last deglaciation: constraints on sensitivity to temperature and impurities, *Clim. Past*, 13, 833–853, <https://doi.org/10.5194/cp-13-833-2017>, 2017.
- Broadbent, S. R. and Hammersley, J. M.: Percolation processes: I. Crystals and mazes, *Mathematical Proceedings of the Cambridge Philosophical Society*, 53, 629–641, <https://doi.org/10.1017/S0305004100032680>, 1957.
- Buizert, C. and Severinghaus, J. P.: Dispersion in deep polar firn driven by synoptic-scale surface pressure variability, *The Cryosphere*, 10, 2099–2111, <https://doi.org/10.5194/tc-10-2099-2016>, 2016.
- Buizert, C., Martinerie, P., Petrenko, V. V., Severinghaus, J. P., Trudinger, C. M., Witrant, E., Rosen, J. L., Orsi, A. J., Rubino, M., Etheridge, D. M., Steele, L. P., Hogan, C., Laube, J. C., Sturges, W. T., Levchenko, V. A., Smith, A. M., Levin, I., Conway, T. J., Dlugokencky, E. J., Lang, P. M., Kawamura, K., Jenk, T. M., White, J. W. C., Sowers, T., Schwander, J., and Blunier, T.: Gas transport in firn: multiple-tracer characterisation and model intercomparison for NEEM, Northern Greenland, *Atmos. Chem. Phys.*, 12, 4259–4277, <https://doi.org/10.5194/acp-12-4259-2012>, 2012.
- Capron, E., Landais, A., Buiron, D., Cauquoin, A., Chappellaz, J., Debret, M., Jouzel, J., Leuenberger, M., Martinerie, P., Masson-Delmotte, V., Mulvaney, R., Parrenin, F., and Prie, F.: Glacial-interglacial dynamics of Antarctic firn columns: comparison between simulations and ice core air- $\delta^{15}\text{N}$ measurements, *Clim. Past*, 9, 983–999, <https://doi.org/10.5194/cp-9-983-2013>, 2013.
- Eicher, O., Baumgartner, M., Schilt, A., Schmitt, J., Schwander, K., Stocker, T. F., and Fischer, H.: Climatic and insolation control on the high-resolution total air content in the NGRIP ice core, *Clim. Past*, 12, 1979–1993, <https://doi.org/10.5194/cp-12-1979-2016>, 2016.
- Enting, I. G.: Statistics of firn closure: a simulation study, *J. Glaciol.*, 39, 133–142, 1993.
- Fabre, A., Barnola, J.-M., Arnaud, L., and Chappellaz, J.: Determination of gas diffusivity in polar firn: comparison between experimental measurements and inverse modeling, *Geophys. Res. Lett.*, 27, 557–560, 2000.
- Freitag, J., Kipfstuhl, S., and Laepple, T.: Core-scale radioscopic imaging: a new method reveals density-calcium link in Antarctic firn, *J. Glaciol.*, 59, 1009–1014, <https://doi.org/10.3189/2013JoG13J028>, 2013.
- Ghanbarian, B. and Hunt, A. G.: Universal scaling of gas diffusion in porous media, *Water Resour. Res.*, 50, 2242–2256, <https://doi.org/10.1002/2013WR014790>, 2014.
- Goujon, C., Barnola, J.-M., and Ritz, C.: Modeling the densification of polar firn including heat diffusion: Application to close-off characteristics and gas isotopic fractionation for Antarctica and Greenland sites, *J. Geophys. Res.*, 108, 4792, <https://doi.org/10.1029/2002JD003319>, 2003.
- Gregory, S. A., Albert, M. R., and Baker, I.: Impact of physical properties and accumulation rate on pore close-off in layered

1692

C. F. Schaller et al.: Gas enclosure in polar firn

- firn, *The Cryosphere*, 8, 91–105, <https://doi.org/10.5194/tc-8-91-2014>, 2014.
- Herron, M. M. and Langway, C. C.: Firn Densification: An Empirical Model, *J. Glaciol.*, 25, 373–385, <https://doi.org/10.3189/S0022143000015239>, 1980.
- Johnsen, S. J., Clausen, H. B., Dansgaard, W., Gundestrup, N. S., Hansson, M., Jonsson, P., Steffensen, J. P., and Sveinbjornsdottir, A. E.: A “deep” ice core from East Greenland, *Meddelelser Om Grønland: Geoscience*, 29, 1–22, 1992.
- Jouzel, J., Lorius, C., Petit, J. R., Genthon, C., Barkov, N. I., Kotlyakov, V. M., and Petrov, V. M.: Vostok ice core: a continuous isotope temperature record over the last climatic cycle (160,000 years), *Nature*, 329, 403–408, <https://doi.org/10.1038/329403a0>, 1987.
- Jouzel, J., Masson-Delmotte, V., Cattani, O., Dreyfus, G., Falourd, S., Hoffmann, G., Minster, B., Nouet, J., Barnola, J.-M., Chappellaz, J., Fischer, H., Gallet, J. C., Johnsen, S., Leuenberger, M., Loulergue, L., Luethi, D., Oerter, H., Parrenin, F., Raisbeck, G., Raynaud, D., Schilt, A., Schwander, J., Selmo, E., Souchez, R., Spahni, R., Stauffer, B., Steffensen, J. P., Stenni, B., Stocker, T. F., Tison, J. L., Werner, M., and Wolff, E. W.: Orbital and millennial antarctic climate variability over the past 800,000 years, *Science*, 317, 793–796, <https://doi.org/10.1126/science.1141038>, 2007.
- Koehler, S. A., Hilgenfeldt, S., and Stone, H. A.: Liquid Flow through Aqueous Foams: The Node-Dominated Foam Drainage Equation, *Phys. Rev. Lett.*, 82, 4232–4235, <https://doi.org/10.1103/PhysRevLett.82.4232>, 1999.
- Landais, A., Barnola, J., Kawamura, K., Caillon, N., Delmotte, M., Van Ommen, T., Dreyfus, G., Jouzel, J., Masson-Delmotte, V., Minster, B., Freitag, J., Leuenberger, M., Schwander, J., Huber, C., Etheridge, D., and Morgan, V.: Firn-air $\delta^{15}\text{N}$ in modern polar sites and glacial-interglacial ice: a model-data mismatch during glacial periods in Antarctica?, *Quaternary Sci. Rev.*, 25, 49–62, <https://doi.org/10.1016/j.quascirev.2005.06.007>, 2006.
- Legrand, M. and Mayewski, P.: Glaciochemistry of polar ice cores: A review, *Rev. Geophys.*, 35, 219–243, <https://doi.org/10.1029/96RG03527>, 1997.
- Loulergue, L., Schilt, A., Spahni, R., Masson-Delmotte, V., Blunier, T., Lemieux, B., Barnola, J.-M., Raynaud, D., Stocker, T. F., and Chappellaz, J.: Orbital and millennial-scale features of atmospheric CH_4 over the past 800,000 years, *Nature*, 453, 383–386, <https://doi.org/10.1038/nature06950>, 2008.
- Martinerie, P., Lipenkov, V. Y., and Raynaud, D.: Correction of air-content measurements in polar ice for the effect of cut bubbles at the surface of the sample, *J. Glaciol.*, 36, 299–303, 1990.
- Martinerie, P., Raynaud, D., Etheridge, D. M., Barnola, J.-M., and Mazaudier, D.: Physical and climatic parameters which influence the air content in polar ice, *Earth Planet. Sc. Lett.*, 112, 1–13, 1992.
- Mitchell, L. E., Buizert, C., Brook, E. J., Breton, D. J., Fegyveresi, J., Baggenstos, D., Orsi, A., Severinghaus, J., Alley, R. B., Albert, M., Rhodes, R. H., McConnell, J. R., Sigl, M., Maselli, O., Gregory, S., and Ahn, J.: Observing and modeling the influence of layering on bubble trapping in polar firn, *J. Geophys. Res.*, 120, 2558–2574, <https://doi.org/10.1002/2014JD022766>, 2015.
- Nguyen, T., Tran, T., Willemsz, T., Frijlink, H., Ervasti, T., Ketola, J., and Maarschalk, K.: A density based segmentation method to determine the coordination number of a particulate system, *Chem. Eng. Sci.*, 66, 6385–6392, <https://doi.org/10.1016/j.ces.2011.08.044>, 2011.
- Otsu, N.: A Threshold Selection Method from Gray-Level Histograms, *IEEE Trans. Syst. Man. Cybern.*, 9, 62–66, 1979.
- Parrenin, F., Remy, F., Ritz, C., Siegert, M. J., and Jouzel, J.: New modeling of the Vostok ice flow line and implication for the glaciological chronology of the Vostok ice core, *J. Geophys. Res.*, 109, D20102, <https://doi.org/10.1029/2004JD004561>, 2004.
- Parrenin, F., Barker, S., Blunier, T., Chappellaz, J., Jouzel, J., Landais, A., Masson-Delmotte, V., Schwander, J., and Veres, D.: On the gas-ice depth difference (Δ depth) along the EPICA Dome C ice core, *Clim. Past*, 8, 1239–1255, <https://doi.org/10.5194/cp-8-1239-2012>, 2012.
- Raynaud, D. and Lebel, B.: Total gas content and surface elevation of polar ice sheets, *Nature*, 281, 289–291, <https://doi.org/10.1038/281289a0>, 1979.
- Raynaud, D., Lipenkov, V., Lemieux-Dudon, B., Duval, P., Loutre, M.-F., and Lhomme, N.: The local insolation signature of air content in Antarctic ice, A new step toward an absolute dating of ice records, *Earth Planet. Sc. Lett.*, 261, 337–349, <https://doi.org/10.1016/j.epsl.2007.06.025>, 2007.
- Schaller, C. F., Freitag, J., and Eisen, O.: Firn microstructure in the lock-in zone for three polar ice cores, *PANGAEA*, <https://doi.org/10.1594/PANGAEA.879577>, 2017.
- Schneebeil, M. and Sokratov, S. A.: Tomography of temperature gradient metamorphism of snow and associated changes in heat conductivity, *Hydrol. Process.*, 18, 3655–3665, <https://doi.org/10.1002/hyp.5800>, 2004.
- Schwander, J.: The transformation of snow to ice and the occlusion of gases, in: *The Environmental Record in Glaciers and Ice Sheets*, edited by: Oeschger, H. and Langway, C. C., John Wiley & Sons, Chichester, 53–67, 1989.
- Schwander, J. and Stauffer, B.: Age difference between polar ice and the air trapped in its bubbles, *Nature*, 311, 45–47, <https://doi.org/10.1038/311045a0>, 1984.
- Schwander, J., Barnola, J.-M., Andrié, C., Leuenberger, M., Ludin, A., Raynaud, D., and Stauffer, B.: The age of the air in the firn and the ice at Summit, Greenland, *J. Geophys. Res.*, 98, 2831–2838, <https://doi.org/10.1029/92JD02383>, 1993.
- Schwander, J., Sowers, T., Barnola, J.-M., Blunier, T., Fuchs, A., and Malaizé, B.: Age scale of the air in the summit ice: Implication for glacial-interglacial temperature change, *J. Geophys. Res.*, 102, 19483–19493, <https://doi.org/10.1029/97JD01309>, 1997.
- Severinghaus, J. and Battle, M.: Fractionation of gases in polar ice during bubble close-off: New constraints from firn air Ne, Kr and Xe observations, *Earth Planet. Sc. Lett.*, 244, 474–500, <https://doi.org/10.1016/j.epsl.2006.01.032>, 2006.
- Sowers, T., Bender, M., Raynaud, D., and Korotkevich, Y. S.: $\delta^{15}\text{N}$ of N_2 in air trapped in polar ice: A tracer of gas transport in the firn and a possible constraint on ice age-gas age differences, *J. Geophys. Res.*, 97, 15683, <https://doi.org/10.1029/92JD01297>, 1992.
- Stauffer, B., Schwander, J., and Oeschger, H.: Enclosure of air during metamorphosis of dry firn to ice, *Ann. Glaciol.*, 6, 108–112, 1985.
- Stauffer, D.: Scaling theory of percolation clusters, *Phys. Rep.*, 54, 1–74, [https://doi.org/10.1016/0370-1573\(79\)90060-7](https://doi.org/10.1016/0370-1573(79)90060-7), 1979.

Clim. Past, 13, 1685–1693, 2017

www.clim-past.net/13/1685/2017/

C. F. Schaller et al.: Gas enclosure in polar firn

1693

- Trudinger, C. M., Enting, I. G., Etheridge, D. M., Francey, R. J., Levchenko, V. A., Steele, L. P., Raynaud, D., and Arnaud, L.: Modeling air movement and bubble trapping in firn, *J. Geophys. Res.*, 102, 6747–6763, <https://doi.org/10.1029/96JD03382>, 1997.
- van der Marck, S. C.: Percolation thresholds of the duals of the face-centered-cubic, hexagonal-close-packed, and diamond lattices, *Phys. Rev. E*, 55, 6593–6597, <https://doi.org/10.1103/PhysRevE.55.6593>, 1997.
- Vinther, B. M., Buchardt, S. L., Clausen, H. B., Dahl-Jensen, D., Johnsen, S. J., Fisher, D. A., Koerner, R. M., Raynaud, D., Lipenkov, V., Andersen, K. K., Blunier, T., Rasmussen, S. O., Steffensen, J. P., and Svensson, A. M.: Holocene thinning of the Greenland ice sheet, *Nature*, 461, 385–388, <https://doi.org/10.1038/nature08355>, 2009.
- Weiler, K.: On the composition of firn air and its dependence on seasonally varying atmospheric boundary conditions and the firn structure, Ph.D. thesis, University of Bern, 2008.
- Wierman, J. C. and Naor, D. P.: Desirable properties of universal formulas for percolation thresholds, *Congressus Numerantium*, 125–142, 2003.
- Witrant, E., Martinerie, P., Hogan, C., Laube, J. C., Kawamura, K., Capron, E., Montzka, S. A., Dlugokencky, E. J., Etheridge, D., Blunier, T., and Sturges, W. T.: A new multi-gas constrained model of trace gas non-homogeneous transport in firn: evaluation and behaviour at eleven polar sites, *Atmos. Chem. Phys.*, 12, 11465–11483, <https://doi.org/10.5194/acp-12-11465-2012>, 2012.

Publication III

Schaller, C. F., Kipfstuhl, S., Steen-Larsen, H. C., Freitag, J., and Eisen, O.: On the influence of polar snowpack stratigraphy on the interpretation of ice-core and altimetry data, *Journal of Geophysical Research: Earth Surface*, under review, 2017

Submitted for publication in *JGR-Earth Surface*. Not subject to U.S. copyright.

1 **On the influence of polar snowpack stratigraphy on the**
2 **interpretation of ice-core and altimetry data**

3 **Christoph Florian Schaller¹, Sepp Kipfstuhl¹, Hans Christian Steen-Larsen², Johannes**
4 **Freitag¹, Olaf Eisen^{1,3}**

5 ¹Alfred Wegener Institute, Helmholtz Centre for Polar and Marine Research, Bremerhaven, Germany

6 ²Centre for Ice and Climate, Niels Bohr Institute, University of Copenhagen, Denmark

7 ³Department of Geosciences, University of Bremen, Germany

8 **Key Points:**

- 9 • a single ice-core melt record is not necessarily representative due to the large spatial
10 heterogeneity of melt features
- 11 • stratigraphic variability is directionally dependent which complicates the interpretation
12 of spatial signals (e.g. from remote sensing)
- 13 • melt pipes indicate deep penetration of water in cold Greenlandic plateau firn (through
14 six years of accumulation)

Corresponding author: Christoph Florian Schaller, christoph.schaller@awi.de

Submitted for publication in *JGR-Earth Surface*. Not subject to U.S. copyright.

Abstract

Density is a fundamental property of polar snowpacks and of particular importance for various applications such as remote sensing, surface-mass-balance estimates and paleoclimatic ice-core studies. As a result, there is growing interest in quantifying and understanding the stratigraphy of the snowpack and its spatial variability. Melting and refreezing significantly impact the density layering. Melt frequencies observed in polar ice cores are commonly used as markers for extreme summer temperatures. Moreover, the evolution of a seasonal cycle in density with depth is not well-understood as all of these aspects require extensive field data. To provide a larger sample size, we analyzed snow cores up to 5 m depth from two sampling sites on the Greenlandic and East Antarctic plateaus and determined the spatial distribution of melt features along two orthogonal trench walls of 60 m length and 4 m depth for the Greenland site. We quantify how the observed variability of melt features is strongly influencing the ability to interpret single-core melt records. In particular, prominent vertical melt pipes indicate deep penetration of water in cold Greenlandic plateau firn. For the spatial variability in density, we find a much larger homogeneity of the snowpack along the main wind direction and an imprint of surface features orthogonal to it. Thus, within a certain area (such as the footprint of an altimeter) the stratigraphic variability is directionally dependent and estimation of a representative profile (e.g. from snow cores or modeling) is not straightforward.

1 Introduction

For altimetry-based estimates of ice-sheet mass changes, the largest uncertainty lies in the conversion of volume to mass [Shepherd *et al.*, 2012]. On the other hand, density as a physical parameter of the porous snow and firn influences air transport in the pore space [Colbeck, 1989; Severinghaus *et al.*, 2001] and its evolution with depth affects the storage of paleoclimatic information as the firn densifies [Herron and Langway, 1980; Breant *et al.*, 2017] and bubbles are sealed [Schwander and Stauffer, 1984; Schaller *et al.*, 2017a]. As a consequence, the density layering of the snow surface and, in particular, its spatial variability has been a focus of recent studies [Proksch *et al.*, 2015; Laepple *et al.*, 2016].

Stratigraphy is an important parameter for microwave transfer models and active remote sensing [Picard *et al.*, 2013; Rutter *et al.*, 2014] with the root mean square error in retrieved snow height approaching 50% when neglecting stratigraphy [Durand *et al.*, 2011]. Vertical density variability and firn stratigraphy have been observed to change with depth [Hoerhold *et al.*, 2011]. At the same time a correlation with impurity concentrations (particularly Ca^{2+}) develops as they imprint their seasonal cycle on the density in the firn [Hoerhold *et al.*, 2012; Freitag *et al.*, 2013a]. However, a seasonal cycle in density is present even in the first meter of snow in low accumulation regions but overprinted by strong stratigraphic noise [Laepple *et al.*, 2016]. The redistribution of surface snow due to wind-driven snow drift is known to strongly influence the spatial variability of the snowpack [Libois *et al.*, 2014]. In particular, the formation of dunes along the main wind direction, separating snowfields with lengths of the order of meters induces horizontal undulations of the snow surface [Birnbaum *et al.*, 2010]. Burial of these features has been identified as a main cause of lateral density variability [Proksch *et al.*, 2015; Laepple *et al.*, 2016].

As ice sheets are exposed to very warm conditions, particularly temperatures above the freezing point, the snowpack heats up and its surface can start to melt. This decreases the albedo of the surface and triggers a positive feedback [Box *et al.*, 2012]. The meltwater either runs off or is retained or refrozen in the snow and firn below. While between 2000 and 2008 the mass loss of the Greenland ice sheet (GrIS) was equally split between surface processes (mainly runoff) and calving [van den Broeke *et al.*, 2009], surface mass balance (SMB) has become the dominant component in the recent years [Enderlin *et al.*, 2014]. Regional climate models estimate that about half of the annual meltwater is refrozen in Greenland [Ettema *et al.*, 2009], nonetheless it is a big source of uncertainty for remote-sensing-based estimates of SMB. As a consequence, there have been several attempts to quantify refreezing by energy-

Submitted for publication in *JGR-Earth Surface*. Not subject to U.S. copyright.

66 balance-based models [Colbeck, 1975; Pfeffer *et al.*, 1990] but they both lack verification with
67 in-situ data [for a review see Reijmer *et al.*, 2012] and the complexity to represent the three-
68 dimensional percolation patterns observed in the field [e.g. Humphrey *et al.*, 2012].

69 In July and August 2012, a special weather pattern with low-level liquid clouds [Ben-
70 nartz *et al.*, 2013] and advection of warm air from the south [Fettweis *et al.*, 2013] resulted
71 in temperatures above the freezing point for 98.6% of the GrIS [Nghiem *et al.*, 2012]. Subse-
72 quent refreezing of meltwater caused the formation of substantial ice layers in the snowpack,
73 acting as reflectors for electromagnetic waves and thus strongly affecting remote measure-
74 ments such as radar altimetry [Nilsson *et al.*, 2015]. According to ice-core records, such
75 widespread melting last occurred in 1889 [Clausen *et al.*, 1988]. The influence of rain (as
76 observed at the NEEM field site in summer 2012 [Nghiem *et al.*, 2012]) on the surface energy
77 budget at higher elevations of the GrIS is unclear [Fausto *et al.*, 2016]. Moreover, 2012 holds
78 the record for the highest mass loss in the satellite era [McMillan *et al.*, 2016]. The likelihood
79 of such extreme melt events is expected to increase in the context of climate change [McGrath
80 *et al.*, 2013; Collins *et al.*, 2013].

81 With the recurrence of melt events over longer periods of time (decades to millenia), a
82 frequency record of extremely warm summers is created [Langway and Shoji, 1990; Alley and
83 Anandkrishnan, 1995]. Field observations have shown that depending on the temperature
84 and structure of the snowpack, not only continuous melt layers, but also features such as ice
85 lenses [Das and Alley, 2005] and melt pipes [Pfeffer and Humphrey, 1996] can form in differ-
86 ent depths. Analysis of melt records can indicate single events or changing regime conditions,
87 such as the warming of West Antarctica [Das and Alley, 2008] and the Canadian Arctic ice
88 caps [Fisher *et al.*, 2012]. For Southern Greenland, shallow-core data have been linked to
89 satellite-derived melt [Rowe *et al.*, 1995]. Several methods have been established to detect
90 snow melt on the GrIS from space-borne passive microwave data [Tedesco, 2007; Hall *et al.*,
91 2013]. Nevertheless, a robust interpretation requires further understanding of signal formation
92 in snow and firn.

93 In this study, we present the results of two extensive snowpack studies conducted at
94 Kohnen station, East Antarctica, and in the scope of the East Greenland ice core project
95 (EGRIP). Analyzing snow cores of 2 – 5 m depth, we investigate the small-scale spatial vari-
96 ability of the snowpack with a focus on the influence of the main wind direction and the
97 evolution of the density signal with depth. For EGRIP, a mapping of the melt features dating
98 to the summer of 2012 provides us with the rare opportunity to learn about the impact of such
99 extreme events in general.

100 2 Materials and Methods

101 In May 2016, two trenches of 4 m depth were excavated in the proximity of the EGRIP
102 field site (75.63°N, 35.98°W, 2663 m above sea level) using a Westa rotary plow mounted in
103 front of a Pistenbully. Both trenches (collectively referred to as LTX trenches) had a length of
104 about 60 m at full depth. The LTW trench followed the main wind direction as indicated by
105 dune orientation (232°, i.e. SW) while the LTO trench lied orthogonal to it. Between 19 and
106 27 May 2016, 22 five-meter snow cores were extracted from the outer walls of both trenches
107 (by manually excavating the fifth meter) at a sampling interval of 5 m starting about 15 m from
108 the common origin. Each core was named according to the respective trench and numbered
109 with increasing distance (starting from zero) as can be seen in Fig. 1a. As the top meter was
110 sampled within the first 24 hours after excavation, there was no significant alteration of the
111 surface snow. For the outer trench walls, the areal melt fraction was determined visually – a
112 reference horizon was marked using wooden sticks and the relative depth and extent of melt
113 features measured with a caliper and a tape.

114 In order to convert the areal melt fractions (visible on the wall surface) to a mass distribu-
115 tion of refrozen meltwater versus depth, we averaged the vertical profiles along both trenches.

Submitted for publication in *JGR-Earth Surface*. Not subject to U.S. copyright.

116 This implicitly assumes that the density of melt features (which is not necessarily the density
117 of pure ice due to enclosed snow and air) is independent of depth. In addition, vertically
118 summing up the melt layer thicknesses at a horizontal resolution of 0.1 m along both trenches
119 yields the probability distribution of finding a certain total melt layer thickness in an ice core
120 (diameter 0.1 m) drilled at the study site. We then conducted simple Monte Carlo simulations
121 (by repeatedly drawing from this distribution) to determine the number of cores that would be
122 necessary for their average total melt layer thickness to be within a certain range of the true
123 value with a confidence level of 95%.

124 Hourly automatic weather station (AWS) data for field sites NASA-E (75.00°N, 30.00°W,
125 182 km from EGRIP, 2584 m above sea level) and NEEM (77.44°N, 51.07°W, 438 km from
126 EGRIP, 2450 m above sea level) covering the complete 2012 melt event were obtained from
127 the Greenland Climate Network [Steffen *et al.*, 1996]. The AWS are equipped with four near-
128 surface air temperature sensors in passively ventilated solar radiation shields (two Type-E
129 Thermocouples and two Campbell Scientific CS-500), two surface height sensors (Campbell
130 Scientific SR-50) and one upward- and one downward-facing pyranometer (LI-COR 200 SZ).
131 As one of the CS-500 was partially non-operational at the NASA-E site, we averaged only
132 the other three sensors for both sites. Comparison of a similar dataset with satellite-derived
133 surface temperatures yielded a root mean square error of 2.1 K for temperatures ranging from
134 -40 to 0°C [Hall *et al.*, 2008]. For the change in surface height, we calculated daily mean
135 values from both available sensors. Surface albedo is computed automatically from the up-
136 ward and downward solar irradiance. An albedo accuracy of 0.035 for the daily mean values
137 has been determined by comparison with MODIS data [Stroeve *et al.*, 2006].

138 Between 23 and 27 January 2016, sixteen two-meter snow cores were taken in the prox-
139 imity of Kohlen station, East Antarctica (75.01°S, 0.08°E, 2885 m above sea level) within the
140 CoFi Liner Project (CLP). Sampling was conducted along three lines (parallel, diagonal and
141 orthogonal to the main wind direction of 57° , i.e. NE to ENE [Reijmer and van den Broeke,
142 2003]) at distances of 1, 5, 15, 35 and 75 m from the origin (see Fig. 1b and c). There was no
143 observation of significant alterations of the snow surface within the five days of sampling.

144 All snow cores were sampled using the liner technique [Schaller *et al.*, 2016], trans-
145 ported to the Alfred Wegener Institute in frozen condition and analyzed in the AWI-Ice-CT
146 for mm-resolution density [Freitag *et al.*, 2013b]. The results were matched using an adapted
147 version of the dynamic time warping (DTW) algorithm [Schaller *et al.*, 2016]. It yields the
148 shared variance R^2 between two density profiles, independent of the current surface height
149 and thickness variations of the same layer and allows stacking of the aligned signals. Spectral
150 analysis of the stacked profiles was conducted using the Cooley–Tukey fast Fourier transform
151 (FFT) algorithm [Cooley and Tukey, 1965]. Significance checking compared to white noise
152 has been carried out using Fisher’s g -statistic [Wichert *et al.*, 2004].

153 3 Results

154 3.1 Spatial melt record

155 As an example of the observed melt features dating to summer 2012, the affected section
156 of a snow core from the LTW trench is shown in Fig. 2. Throughout the analyzed trench walls
157 we find the uppermost occurrence of refrozen meltwater to be a very thin crust (less than 3 mm
158 for 88% of the trench lengths) at a mean depth of 1.62 ± 0.03 m (95% confidence). It is the only
159 spatially continuous melt feature. We use its upper edge as a reference horizon to determine the
160 percolation depths of the other observed melt features in the outer walls of the LTO and LTW
161 trenches (Fig. 3). Other prevalent features are a second thin crust (up to 5 mm thick) within
162 the first 0.05 m of the top crust and several distinct ice lenses 0.3–0.4 m below the reference
163 horizon (e.g. Fig. 2). Figure 4 shows the mass distribution of refrozen melt versus percolation
164 depth. The main fractions are found in the two uppermost ice crusts (top 0.05 m, 26%) and the
165 aforementioned ice lenses (0.3–0.4 m, 31%). The latter are present along 42% of the length of

Submitted for publication in *JGR-Earth Surface*. Not subject to U.S. copyright.

166 the two trench walls. Other ice lenses and crusts can appear anywhere up to 0.6 m below the
 167 reference layer. In both trenches we find prominent vertical melt pipes (average diameter up
 168 to 0.2 m), occasionally forming small ice lenses when penetrating horizontal crusts and thus
 169 having cascade-like shapes (58% of a total of 36 melt pipes). Within the first meter, these pipe
 170 features contain a mass fraction of approximately 25%. Below the percolation depth of 1 m
 171 displayed in Fig. 3 only some of the pipes continue, three of them (two for LTW, one for LTO)
 172 do exceed the bottom of the trench (about 4 m below the surface and thus 2.4 m below the
 173 reference horizon).

174 The AWS data show three periods with temperatures at or above freezing point, around
 175 11 July, 29 July and 5 August 2012 (Fig. 5). In all three cases the warming comes along with
 176 a significant decrease in snow albedo compared to the conventional (i.e. non-melt) values of
 177 0.82–0.86 [Box *et al.*, 2012]. A decrease of the snow surface height can be observed for both
 178 sites, in particular a lowering of about 0.15 m at the NEEM site between 11 July and 21 July.

179 Based on our spatial melt record, we calculated the probability of finding a certain total
 180 2012 melt layer thickness for an ice core drilled in the study area, shown in Fig. 6. We
 181 find an average ice-equivalent melt layer thickness of 29 mm, corresponding to 20% of the
 182 mean annual accumulation rate of about $140 \text{ kg m}^{-2} \text{ a}^{-1}$ for the recent years [Schaller *et al.*,
 183 2016]. By Monte Carlo sampling the probability distribution of total melt layer thicknesses at
 184 a confidence level of 95%, we find the necessary number of ice cores to be 15 and 60 in order
 185 to be within ± 10 mm or ± 5 mm of the mean value.

186 3.2 Snow cores

187 For the CLP cores, a decrease in shared variability R^2 of the two-meter density profiles
 188 with distance can be observed along each line in Fig. 7. Here, distance is given with respect
 189 to CLP_00 and the profiles along each line were compared to a stacked density profile of
 190 the four profiles within the first 1 m by 1 m square (CLP_00 ... CLP_03). Orthogonal and
 191 diagonal to the main wind direction, the shared variability strongly decreases within the first
 192 15–20 m before staying rather constant at around 0.67. Parallel to the main wind direction,
 193 however, a similar decline in shared variability within the first 5 m is followed by a much
 194 slower (approximately linear) decrease from 0.81 at 5 m to 0.73 at 75 m.

195 For the LTX cores, we first determined the shared variance after DTW matching of five-
 196 meter cores from the same trench with a certain distance (Fig. 8). Using linear regression,
 197 we find the average R^2 to be decreasing parallel to the main wind direction (i.e. the LTW
 198 trench) from about 0.79 at a distance of 5 m to 0.72 at 35 m. In contrast, for the orthogonal
 199 LTO trench the values vary around a constant level of 0.71 ± 0.01 for distances between 5
 200 and 35 m. At distances larger than 35 m, we find similar R^2 values of about 0.71 for both
 201 trenches. In a second step, we compared the decrease in R^2 along the LTW trench for three
 202 consecutive depth intervals of 1.5 m each (omitting the last 0.5 m). As can be observed in
 203 Fig. 9, all three intervals show the same trend but there are offsets with the highest correlations
 204 occurring for 3–4.5 m. In order to further investigate this, we conducted spectral analyses of
 205 stacked density profiles for the three depth intervals along the LTW trench (Fig. 10). We find
 206 a significant ($p < 0.05$) peak in the spectrum of the 3–4.5 m interval for wavelengths around
 207 0.6 m, while no such peak is present for the other intervals. Finally, we calculated the shared
 208 variance between density profiles of cores from the different trenches (Fig. 11). Along the
 209 LTO trench, we observe a significant decrease in R^2 with all LTW snow cores for positions 3–
 210 5. Subsequently, it increases back to the original values for LTO positions 6–8 and decreases
 211 again.

212 4 Interpretation and Discussion

213 4.1 Melt at EGRIP

214 For the EGRIP melt record, we interpret the continuous thin melt crust (e.g. Fig. 2) as a
215 July or August 2012 near-surface or surface crust. Thus, we will use it as a reference horizon
216 to determine percolation depths for the other melt features (Fig. 3). The frequent appearance
217 of a second melt layer 0.05 m below is in accordance with melt experiments conducted for the
218 snow surface at Siple Dome, West Antarctica [Das and Alley, 2005], where comparable accu-
219 mulation rates and temperatures occur. About half of the total meltwater from summer 2012
220 refroze above the next prevalent melt feature, the ice lenses 0.3–0.4 m below the reference
221 horizon (Fig. 4). As the depth difference corresponds to the accumulation of one year [Valle-
222 longa et al., 2014], approximately one third of the meltwater refroze in the summer snow of
223 2011 after percolating through the winter snow of 2011/12. This agrees with melt observa-
224 tions in West Greenland [Pfeffer and Humphrey, 1998] showing that ice layers preferentially
225 form along the previous summer surface, which acts as a strong boundary for the meltwater to
226 penetrate through.

227 The remaining meltwater (at least 15%) percolated through more than one year of pre-
228 viously deposited material, predominantly along vertical melt pipes. We observed several
229 prominent melt pipes (Fig. 3), three of them with percolation depths of more than 2.4 m (and
230 thus spanning at least six years of accumulation in depth). For the GrIS, heterogeneous in-
231 filtration of meltwater to several meters depth along such pipe structures has already been
232 documented in snow pits [Pfeffer and Humphrey, 1996], tracked thermally and observed in
233 dye tracing experiments [Humphrey et al., 2012]. In a new study, an upward-looking radar
234 deployed in the firn allowed the first quasi-continuous observation of melt-water infiltration
235 along similar patterns indicating a much larger fraction of liquid water percolating through
236 the previous summer surface in 2016 [Heilig et al., personnel communication, 2017]. While
237 homogenous wetting front migration is prevalent in snow and firn near the freezing point, het-
238 erogenous infiltration has been identified as dominant in subfreezing firn [Parry et al., 2007].
239 However, all of these studies focussed on the percolation zone of the GrIS, while our site is
240 located further up within the accumulation zone of the plateau where mean annual (and thus
241 snow and firn) temperatures are significantly lower and melt is scarce. Thus, even though
242 the snow and firn are initially subfreezing for the different sites, the interplay and transitions
243 between the two mechanisms are not necessarily similar.

244 Apart from small plate-like ice lenses around the melt pipes we found no signs of hori-
245 zontal meltwater redistribution (i.e. lateral flow) for percolation depths larger than 0.6 m. Even
246 strong crusts (such as previous summer surfaces) that correspond to ice layers in the first 0.6 m
247 are not significantly affecting the melt pipes deeper in the firn. Interestingly, snow pit observa-
248 tions at NEEM, an ice-coring site 438 km north-west of EGRIP with very comparable surface
249 conditions [Schaller et al., 2016] (see also Fig. 5a for air temperatures north-west and south-
250 east of EGRIP), showed that the top 0.6 m were around melting point in July 2012 with the
251 deepest melt feature being an ice layer in a depth of 0.7 m [Nilsson et al., 2015]. We suggest
252 a similar warming of the snowpack at EGRIP (causing a homogeneously advancing wetting
253 front) to explain the presence of melt features only in the top 0.6 m. Vertical water flow in the
254 firn was impeded by spatially extensive (newly formed) ice layers or strong crusts until break-
255 through events occurred, draining the accumulated water at certain "weak" points [as observed
256 in dye tracing experiments by Humphrey et al., 2012]. As the water percolated through the
257 underlying subfreezing firn, it refroze in the observed pipe structures.

258 Percolating water will be around freezing point within millimeters from the surface as
259 thermal equilibrium between sub-freezing snow or firn and inflowing water occurs on time
260 scales of seconds [Pfeffer et al., 1990]. The temperature of the inflowing water is expected
261 to be very close to freezing point (see Fig. 5a for air temperatures), so there is no significant
262 additional surface melting due to sensible heat transfer. As additional melting due to latent heat
263 release cannot exceed the amount of freezing inflowing water, the extent of the pipe structures

Submitted for publication in *JGR-Earth Surface*. Not subject to U.S. copyright.

264 corresponds to an equivalent water inflow of at least 10.5 mm of the total mapped 26.5 mm of
265 water-equivalent melt. There are two possible sources for this water inflow – rain or surface
266 melting. Rain on the Greenlandic plateau in summer 2012 is currently not represented in
267 regional climate models or reanalysis data [Tedesco *et al.*, 2013], but was observed at NEEM
268 on 11 July 2012 [Nghiem *et al.*, 2012]. As meltwater and (potential) rain will mix, we do not
269 terminologically distinguish between melt features and refrozen rainwater.

270 4.2 Insights from AWS data

271 At NEEM, temperatures were already around the freezing point on 10 July, but only
272 the rainfall on 11 July and the subsequent wetting of the snowpack caused the main decrease
273 of the snow albedo for this site (Fig. 5). On 13 July, sleet was recorded at NEEM [Nilsson
274 *et al.*, 2015], which caused the snow albedo to partially recover. Melt conditions prevailed
275 until 16 July and the snow albedo stayed below the pre-melt values (indicating the snowpack
276 was still wet) until there was new snow after 21 July. For the snow height (Fig. 5c), a steady
277 decrease was observed between 11 July and 21 July, which we interpret as a combination of
278 surface melting and settling of the snowpack after rain and meltwater percolated through it.
279 We consider the latter to be predominant as the decay in snow height continues even though
280 the temperatures stayed below freezing point after 16 July. For the second warm phase (around
281 29 July) there was only a two-day decrease in snow albedo and no change in snow height. As
282 there are no reports of rain we conclude that only minor surface melting was present. Then
283 again, after temperatures above freezing point on 5 and 6 August, snow albedo was lowered
284 for several days along with a significant decrease in snow height. This may potentially indicate
285 another minor rain event.

286 In the light of the observations at NEEM (438 km north-west of EGRIP) and due to
287 their similarity, the AWS data from the NASA-E site (180 km south-east of EGRIP) can be
288 interpreted as an indicator for the conditions at EGRIP in July and August 2012 (Fig. 5). While
289 the first warm period (10–16 July) had much less of an impact there and the snow albedo had
290 mostly recovered by 18 July, the decrease in albedo was much more persistent in late July
291 and prevailed until after 6 August. Throughout the whole period (11 July to 11 August) the
292 snow surface lowered slowly for a total loss of about 0.08–0.1 m. In agreement with our
293 field observations, we conclude that there was some melting and maybe minor rainfall during
294 the first warm period when the first melt crusts and ice lenses were formed. Then, after the
295 snowpack had refrozen, further melting or rainfall occurred during the second or third warm
296 period, leading to the formation of distinctive melt pipes.

297 4.3 Implications for single-core melt records

298 The probability distribution of finding a certain total 2012 melt layer thickness when
299 drilling an ice core in the EGRIP area (Fig. 6) shows more variability than desirable for the
300 interpretation of single ice-core melt records. This is due to the documented large heterogeneity
301 of melt features that was already suggested by ground-penetrating radar measurements [e.g.
302 Brown *et al.*, 2011]. Even though the absolute thickness values will decrease due to com-
303 paction and thinning (and thus only refer to drillings in the near future), the variability will
304 persist. 3% of cores drilled in the study area would contain more than 100 mm of refrozen wa-
305 ter. In order to obtain a value within ± 10 mm of the average total melt layer thickness (29 mm)
306 with a 95% confidence, it would be necessary to drill fifteen ice cores in the study area. For a
307 precision of ± 5 mm one would already need to drill 60 ice cores. Thus melt records from sin-
308 gle ice cores [e.g. Alley and Koci, 1988; Langway and Shoji, 1990] have to be interpreted with
309 great caution. Exemplarily, for an ice core drilled in the study area, there are significant proba-
310 bilities to find the 2012 event represented by only thin crusts as well as melt features covering
311 several years of accumulation. Thin melt crusts can no longer be detected with reasonable cer-
312 tainty in deep ice cores [Alley and Anandakrishnan, 1995; Orsi *et al.*, 2015], leading to melt
313 events being missed in single cores. Melt features that span several years may be interpreted as
314 multiple events. For sites with high melt frequencies, this uncertainty may be compensated by

Submitted for publication in *JGR-Earth Surface*. Not subject to U.S. copyright.

315 averaging over a sufficient amount of years (and thereby melt events) [e.g. Fisher *et al.*, 2012],
316 but for cold sites, i.e. where melt is scarce, the representativity of single-core melt records is
317 doubtful.

318 **4.4 Directional influence of the wind**

319 Even though previous studies did focus on the variability of the snowpack along a fixed
320 direction [e.g. Laepple *et al.*, 2016], a strong directional influence of the wind due to dune
321 formation and horizontal undulations was already suggested [Proksch *et al.*, 2015]. We can
322 confirm these assumptions for both study sites, Kohnen (East Antarctica) and EGRIP (Green-
323 land). For the shared variance of the two-meter density profiles at Kohnen station (Fig. 7), a
324 significantly higher R^2 is preserved with distance along the main wind direction (and thereby
325 parallel to the dunes), while for the other two (orthogonal and diagonal) the values decrease
326 to a constant level of about 0.68 within the first 10–15 m. For the five-meter density profiles
327 from EGRIP, R^2 is linearly decreasing along the main wind direction, i.e. the LTW trench,
328 until a constant level is reached at 35–40 m distance (Fig. 8). In contrast, the R^2 values for the
329 orthogonal trench have already decreased to the same constant level at 5–10 m. As we apply a
330 matching algorithm for the density layering, this proves that individual stratigraphic features
331 are more persistent parallel to the dunes for both study sites. Thus, wind-driven redistribu-
332 tion of snow causes the snowpack to be significantly more homogenous along the main wind
333 direction.

334 We observed (summer) surface roughnesses (i.e. dune heights) of 0.2–0.3 m at both
335 sites and there are no significant differences in density (similar ranges and standard devia-
336 tions), while the accumulation rates differ by a factor of approximately two ($62 \text{ kg m}^{-2} \text{ a}^{-1}$
337 at Kohnen [Oerter *et al.*, 2000] compared to $120 \text{ kg m}^{-2} \text{ a}^{-1}$ at EGRIP [Vallelonga *et al.*,
338 2014]). This may be the reason that we observe an even larger influence of wind-driven redistri-
339 bution at Kohnen, in the sense that even at a distance of 75 m an increased shared variability
340 prevails along the main wind direction, while the constant "local" level is reached after 35–
341 40 m at EGRIP. In turn, a higher local level in shared variability at EGRIP may result from a
342 larger fraction of snow being deposited evenly (without significant redistribution) due to the
343 higher accumulation rate while erosion (and the resulting decrease in the local shared variabil-
344 ity) plays a bigger role at Kohnen.

345 The shared variance values seem to oscillate at a wavelength of 15–20 m for the LTO
346 trench (Fig. 8). This corresponds to the observed snowfield sizes between dunes formed by
347 strong wind events in East Antarctica [Birnbaum *et al.*, 2010]. In order to quantify this ob-
348 servation, we determined the shared variance between snow cores from the different trenches
349 (Fig. 11). Our interpretation of the distinct wave pattern along the LTO direction is an imprint
350 of the average distance of surface dunes that are formed along the main wind direction [Bir-
351 nbaum *et al.*, 2010] and the snowfields between them. This further confirms the strong influence
352 of wind and its direction on the density stratigraphy of the snowpack.

353 **4.5 Density evolution with depth**

354 We then analyzed the influence of depth on the decrease in shared variance for the LTW
355 trench and do observe the same general trend, but significant offsets (Fig. 9). The lowest values
356 occur for the interval 1.5–3 m, which is a consequence of the various percolation features from
357 the 2012 melt event that are mostly limited to these depths. However, while the values for 0–
358 1.5 m are only slightly higher, we observe a positive offset of about 0.1 in R^2 for 3–4.5 m
359 depth. Thus, within the snowpack the shared variance seems to increase with depth. Notably,
360 for the majority of cases we also observe higher R^2 for the second meter in depth at Kohnen.
361 However, the picture is much less clear as there we only have one pair of snow cores for a
362 certain distance. In comparison, for EGRIP, Greenland, each data point is based on several
363 combinations due to the evenly spaced sampling.

Submitted for publication in *JGR-Earth Surface*. Not subject to U.S. copyright.

364 To investigate at which wavelength this increase in shared variance with depth occurs,
365 we conducted a FFT-based spectral analysis of the stacked 1.5 m density profiles (Fig. 10).
366 While most of the signals are indistinguishable from white noise, a significant ($p < 0.05$) peak
367 is present in the 3–4.5 m interval at a wavelength of about 0.6 m, which corresponds to the
368 accumulation of two years. The fact that we observe a bi-annual peak is probably caused by
369 interannual variations in the local deposition rates, that are often compensated in consecutive
370 years as the surface partially levels out [Muench *et al.*, 2016]. Thus, the seasonal cycle in
371 density [Schaller *et al.*, 2016; Laepple *et al.*, 2016] builds up within the snowpack while the
372 high variability at the surface due to roughness and wind-driven redistribution of snow is
373 steadily abating.

374 5 Conclusions

375 A trench study of the snowpack at EGRIP, Greenland of high spatial resolution and and
376 large horizontal and vertical extent allowed the first accurate determination of the local spatial
377 distribution of refrozen meltwater that resulted from the extremely high temperatures all over
378 Greenland in July and August 2012. We observe large variations in the spatial distribution of
379 total ice layer thickness that an ice core from the EGRIP area may contain. One would need
380 to drill fifteen ice cores in order for the average total melt thickness to be within ± 10 mm
381 of the average of 29 mm. The effect can be reduced for sites with large melt frequencies by
382 averaging multiple events, but there is no such remedy for low-melt sites. There, single melt
383 events will be significantly overestimated, while others will be missed completely. This raises
384 strong doubts about the representativity of single ice-core melt records from regions with low
385 melt frequencies. Furthermore, distinct melt pipes indicate deep heterogenous infiltration of
386 water in cold Greenlandic plateau firn through several years of accumulation with no signifi-
387 cant horizontal redistribution. One possible explanation is rainfall at the EGRIP field site (as
388 observed on other plateau sites in July 2012), a finding that is supported by AWS data. Neither
389 regional climate models nor reanalysis data do represent rainfall on the Greenlandic plateau
390 so far [Tedesco *et al.*, 2013]. Incorporation of our results in both climate and percolation
391 modeling may benefit the understanding of extreme summer melt events, whose frequency
392 is expected to increase in the context of climate change [McGrath *et al.*, 2013; Collins *et al.*,
393 2013].

394 By analyzing snow-core arrays from Greenland and East Antarctica, we showed a sig-
395 nificantly higher homogeneity of the snow density along the main wind direction, proving that
396 wind-driven snow redistribution causes stratigraphic features to be more persistent. Orthogo-
397 nal to the main wind direction, we find an oscillating behavior of the shared variance, strongly
398 suggesting that buried surface structures (i.e. dunes and the interjacent snowfields) dominate
399 the local variability of the snow stratigraphy. These findings are of particular importance for
400 very low-accumulation sites, today as well as under glacial conditions, where the height of
401 surface features can easily exceed the net annual accumulation and thus the interplay of the
402 underlying deposition mechanisms is not well-understood. Furthermore, the directional de-
403 pendence of the stratigraphic variability complicates the interpretation of areal signals (e.g.
404 from remote sensing). Estimation of representative profiles for such areas is not straightfor-
405 ward, but may require ground-based sampling.

406 For the EGRIP site, we find clear evidence of an increasing shared variability of snow
407 density with depth due to the developing seasonal cycle. Our data from East Antarctica indi-
408 cate the same behavior, but does not provide the statistical basis for a detailed investigation.
409 However, the observation of seasonal cycles evolving in East Antarctic firn [Hoerhold *et al.*,
410 2012; Laepple *et al.*, 2016] suggests a similar effect. As a consequence we plan further inves-
411 tigation of the stratigraphic variability and its directional dependence on the East Antarctic
412 plateau with a focus on regions with very low accumulation rates.

413 All of these aspects are of particular importance for altimetry-based SMB estimations.
414 The conversion of volume to mass requires representative density profiles of the snow and

Submitted for publication in *JGR-Earth Surface*. Not subject to U.S. copyright.

415 firn, which are the largest source of uncertainty to date [*Shepherd et al.*, 2012]. Improving
416 these profiles requires understanding both, the spatial variability of the density signal and its
417 evolution with depth (densification). Melt features act as reflectors for electromagnetic waves
418 and thus strongly affect remote-sensing signals by increasing the amount of volume scattering.
419 However, the necessary corrections cannot take into account their large spatial heterogeneity,
420 introducing an additional source of uncertainty.

421 **Acknowledgments**

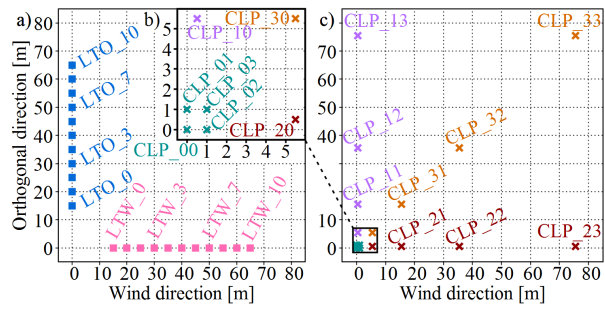
422 First and foremost, the authors acknowledge the support of all involved field personnel
423 both at EGRIP and Kohlen, in particular our mechanic Chris Jacobs. In addition, the authors
424 want to thank Konrad Steffen and his working group for making their AWS data available via
425 the Greenland Climate Network and Achim Heilig for insights into upGPR and his prelimi-
426 nary results. The main author wants to express his gratitude to Julia Goedecke and Alexander
427 Weinhart, who carried out most of the necessary CT measurements under his supervision. Fi-
428 nally, he thanks the German National Merit Foundation (Studienstiftung des deutschen Volkes
429 e.V.) for funding his PhD project.

430 EGRIP is directed and organized by the Center of Ice and Climate at the Niels Bohr
431 Institute. It is supported by funding agencies and institutions in Denmark (A. P. Moller Foun-
432 dation, University of Copenhagen), USA (US National Science Foundation, Office of Po-
433 lar Programs), Germany (Alfred Wegener Institute, Helmholtz Centre for Polar and Marine
434 Research), Japan (National Institute of Polar Research and Artic Challenge for Sustainabil-
435 ity), Norway (University of Bergen and Bergen Research Foundation), Switzerland (Swiss
436 National Science Foundation), France (French Polar Institute Paul-Emile Victor, Institute for
437 Geosciences and Environmental Research) and China (Chinese Academy of Sciences and Bei-
438 jing Normal University).

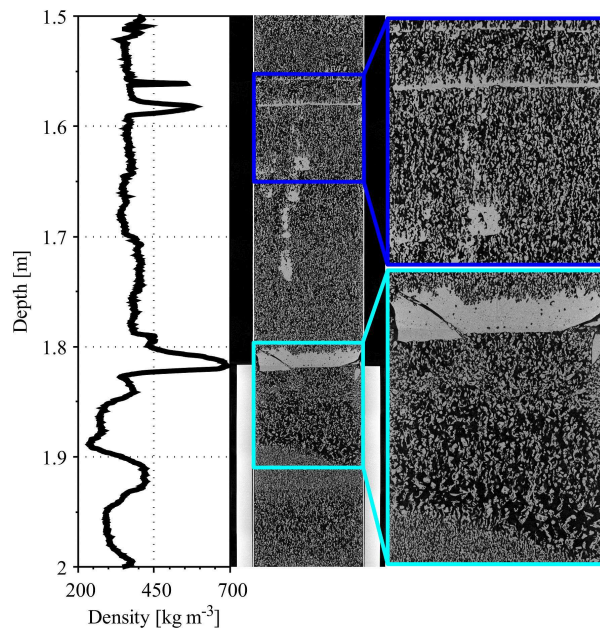
439 Data availability: All data presented in this study is available via the open-access library
440 PANGAEA® [*Schaller et al.*, 2017b].

441 Author contributions: This study was designed by JF, SK, HCSL and CS. Wall sampling
442 was conducted by SK and CS. CS took the snow cores, supervised the CT measurements,
443 evaluated the melt record, densities and AWS data as well as researched and programmed the
444 necessary algorithms. The results were discussed and related to the literature by all coauthors.
445 CS prepared the initial manuscript, which was improved by reviews from all coauthors.

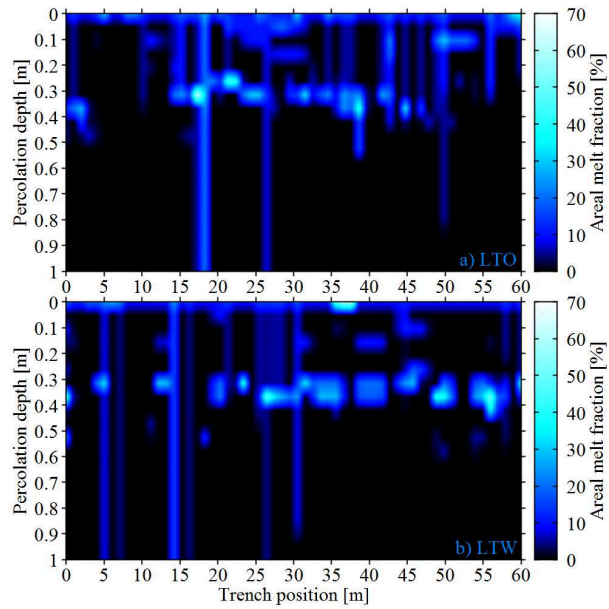
446 Competing interests: The authors declare that they have no conflict of interest.

Submitted for publication in *JGR-Earth Surface*. Not subject to U.S. copyright.

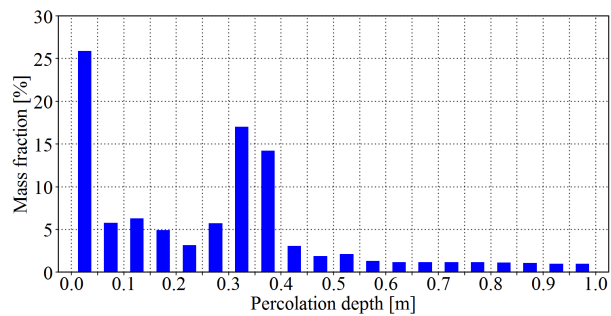
447 **Figure 1.** a) Map of the LTX trenches, sampled at EGRIP, Greenland, in May 2016. b) Zoomed section and
 448 c) overview of the CLP liners taken at Kohnen station, East Antarctica, in January 2016.



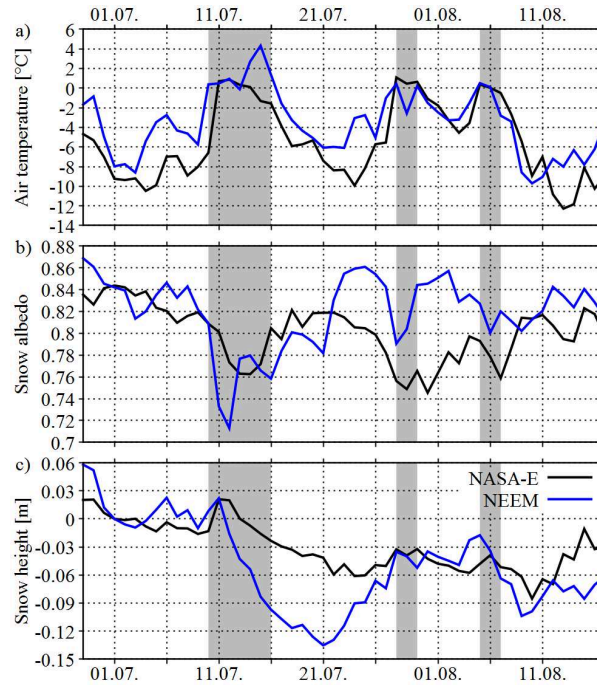
449 **Figure 2.** Example of the 2012 melt features in a snow core from the LTW trench. The density profile in
 450 the left panel has been aligned with the radioscopic image in the center, where ice is represented in white.
 451 Zoomed sections of two thin ice crusts (blue box) and an ice lense (cyan box) are displayed on the right.

Submitted for publication in *JGR-Earth Surface*. Not subject to U.S. copyright.

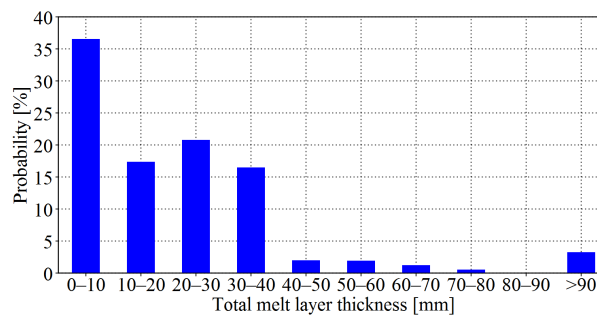
452 **Figure 3.** Areal melt fraction along the a) LTO and b) LTW trench walls. Percolation depths have been
 453 determined with respect to the upper edge of a reference horizon that we interpreted as a July or August 2012
 454 surface or near-surface crust.



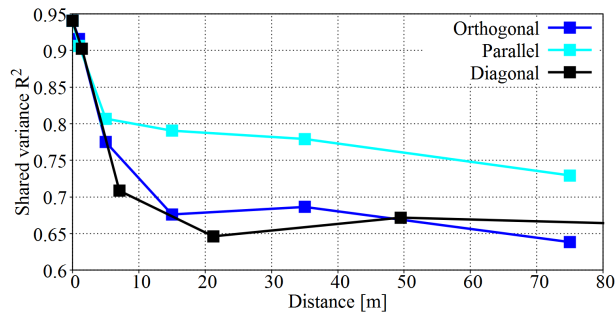
455 **Figure 4.** Mass distribution of refrozen meltwater versus percolation depth. The results for both trenches
 456 have been averaged.

Submitted for publication in *JGR-Earth Surface*. Not subject to U.S. copyright.

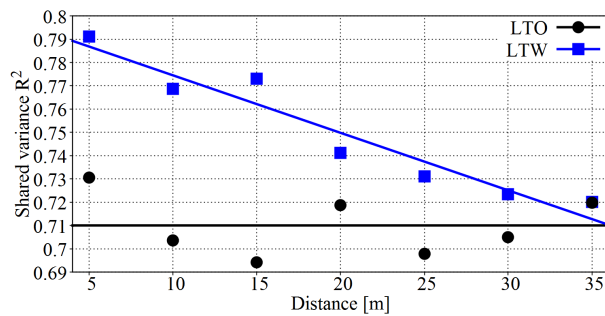
457 **Figure 5.** AWS data for the NEEM and NASA-E sites in summer 2012. Potential melt or rain conditions
 458 are indicated by gray boxes. a) Maximum hourly air temperature per day, b) daily average snow albedo and c)
 459 change in daily average snow height relative to July 1, 2012.



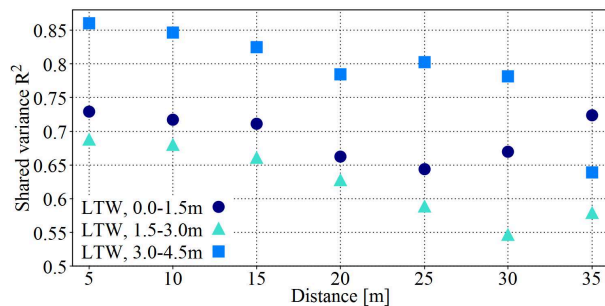
460 **Figure 6.** Probability (y-axis) to find a certain total melt layer thickness (x-axis) when drilling an ice core
 461 (diameter 0.1 m) in the EGRIP area. Notably, it is not possible to find no 2012 melt layer as the uppermost
 462 melt crust from 2012 is continuous.

Submitted for publication in *JGR-Earth Surface*. Not subject to U.S. copyright.

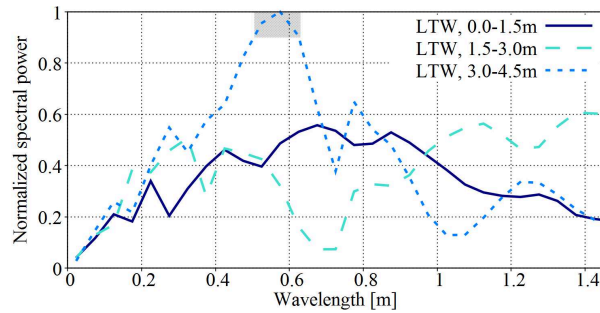
463 **Figure 7.** R^2 after matching the density profiles of two-meter CLP snow cores along the same direction
 464 using the Dynamic Time Warping algorithm. The respective core was compared with a stack of the four cores
 465 around the origin (see Fig. 1).



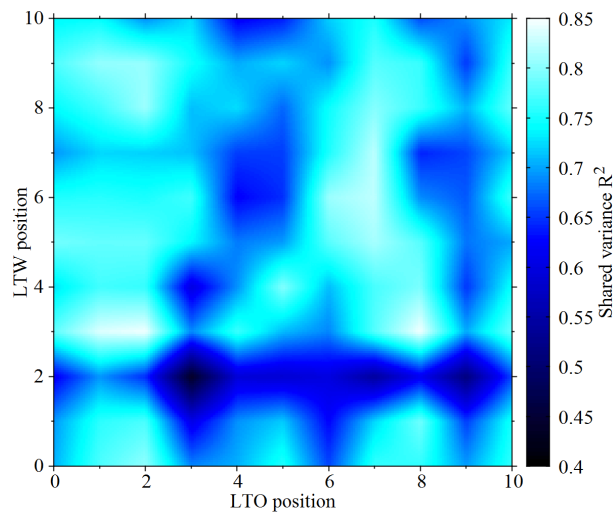
466 **Figure 8.** R^2 after DTW matching the density profiles of five-meter snow cores with a certain distance
 467 from the same LTX trench. The displayed values are averages of all combinations of two snow cores with the
 468 respective distance. The decrease for the LTW trench was fit by a linear regression with $R^2 = 0.93$ while the
 469 values for the LTO trench oscillate around the mean value of 0.71.



470 **Figure 9.** Average R^2 after DTW matching of 1.5 m density profiles versus distance for three consecutive
 471 depth intervals in the LTW trench.

Submitted for publication in *JGR-Earth Surface*. Not subject to U.S. copyright.

472 **Figure 10.** Spectral analysis of stacked 1.5 m density profiles from the LTW trench for three consecutive
 473 depth intervals. The spectral powers (cross-correlations with a complex sinusoid of the wavelength given on
 474 the x-axis) were normalized with respect to the absolute maximum. The eleven density profiles (LTW_0 to
 475 LTW_10) were cut in the given intervals and stacked using the DTW algorithm as described in [Schaller *et al.*,
 476 2016]. For the values within the gray box statistic significance ($p < 0.05$) has been checked by comparison to
 477 white noise using Fisher's g -statistic [Wichert *et al.*, 2004].



478 **Figure 11.** R^2 after DTW matching density profiles of five-meter snow cores from the LTX trenches. For a
 479 map of the positions see Fig. 1. Please note the first liners (LTW_0 and LTO_0) were both taken 15 m from the
 480 common origin in the respective trench.

Submitted for publication in *JGR-Earth Surface*. Not subject to U.S. copyright.481 **References**

- 482 Alley, R., and B. Koci (1988), Ice-Core Analysis at Site A, Greenland: Preliminary Results,
483 *Ann. Glaciol.*, *10*, 1–4, doi:10.1017/S0260305500004067.
- 484 Alley, R. B., and S. Anandkrishnan (1995), Variations in melt-layer frequency in the GISP2
485 ice core: implications for Holocene summer temperatures in central Greenland, *Ann.*
486 *Glaciol.*, *21*, 64–70, doi:10.1017/S0260305500015615.
- 487 Bennartz, R., M. D. Shupe, D. D. Turner, V. P. Walden, K. Steffen, C. J. Cox, M. S. Kulie,
488 N. B. Miller, and C. Pettersen (2013), July 2012 Greenland melt extent enhanced by low-
489 level liquid clouds, *Nature*, *496*(7443), 83–86, doi:10.1038/nature12002.
- 490 Birnbaum, G., J. Freitag, R. Brauner, G. Knig-Langlo, E. Schulz, S. Kipfstuhl, H. Oerter, C. H.
491 Reijmer, E. Schlosser, S. H. Faria, and others (2010), Strong-wind events and their influence
492 on the formation of snow dunes: observations from Kohlen station, Dronning Maud Land,
493 Antarctica, *J. Glaciol.*, *56*(199), 891–902, doi:10.3189/002214310794457272.
- 494 Box, J. E., X. Fettweis, J. C. Stroeve, M. Tedesco, D. K. Hall, and K. Steffen (2012), Greenland
495 ice sheet albedo feedback: thermodynamics and atmospheric drivers, *Cryosphere*, *6*(4),
496 821–839, doi:10.5194/tc-6-821-2012.
- 497 Breant, C., P. Martinerie, A. Orsi, L. Arnaud, and A. Landais (2017), Modelling firn thick-
498 ness evolution during the last deglaciation: constraints on sensitivity to temperature and
499 impurities, *Clim. Past*, *13*(7), 833–853, doi:10.5194/cp-13-833-2017.
- 500 Brown, J., J. Harper, W. T. Pfeffer, N. Humphrey, and J. Bradford (2011), High-resolution
501 study of layering within the percolation and soaked facies of the Greenland ice sheet, *Ann.*
502 *Glaciol.*, *52*(59), 35–42.
- 503 Clausen, H., N. Gundestrup, S. Johnsen, R. Bindshadler, and J. Zwally (1988), Glaciological
504 Investigations in the Crte Area, Central Greenland: A Search for a new Deep-Drilling Site,
505 *Ann. Glaciol.*, *10*, 10–15, doi:10.1017/S0260305500004080.
- 506 Colbeck, S. C. (1975), A theory for water flow through a layered snowpack, *Water Resour.*
507 *Res.*, *11*(2), 261–266, doi:10.1029/WR011i002p00261.
- 508 Colbeck, S. C. (1989), Air movement in snow due to windpumping, *J. Glaciol.*, *35*(120), 209–
509 213.
- 510 Collins, M., R. Knutti, J. Arblaster, J.-L. Dufresne, T. Fichet, P. Friedlingstein, X. Gao, W. J.
511 Gutowski, T. Johns, G. Krinner, M. Shongwe, C. Tebaldi, A. J. Weaver, and M. Wehner
512 (2013), Chapter 12 - Long-term climate change: Projections, commitments and irreversibil-
513 ity, in *Climate Change 2013: The Physical Science Basis. IPCC Working Group I Contri-*
514 *bution to AR5*, edited by IPCC, Cambridge University Press, Cambridge.
- 515 Cooley, J. W., and J. W. Tukey (1965), An algorithm for the machine calculation of complex
516 Fourier series, *Math. Comput.*, *19*(90), 297–301, doi:10.1090/S0025-5718-1965-0178586-
517 1.
- 518 Das, S. B., and R. B. Alley (2005), Characterization and formation of melt layers in polar
519 snow: observations and experiments from West Antarctica, *J. Glaciol.*, *51*(173), 307–312,
520 doi:10.3189/172756505781829395.
- 521 Das, S. B., and R. B. Alley (2008), Rise in frequency of surface melting at Siple Dome through
522 the Holocene: Evidence for increasing marine influence on the climate of West Antarctica,
523 *J. Geophys. Res.*, *113*(D2), doi:10.1029/2007JD008790.
- 524 Durand, M., E. J. Kim, S. A. Margulis, and N. P. Molotch (2011), A First-Order Char-
525 acterization of Errors From Neglecting Stratigraphy in Forward and Inverse Passive
526 Microwave Modeling of Snow, *IEEE Geosci. Remote Sens. Lett.*, *8*(4), 730–734, doi:
527 10.1109/LGRS.2011.2105243.
- 528 Enderlin, E. M., I. M. Howat, S. Jeong, M.-J. Noh, J. H. van Angelen, and M. R. van den
529 Broeke (2014), An improved mass budget for the Greenland ice sheet, *Geophys. Res. Lett.*,
530 *41*(3), 866–872, doi:10.1002/2013GL059010.
- 531 Ettema, J., M. R. van den Broeke, E. van Meijgaard, W. J. van de Berg, J. L. Bam-
532 ber, J. E. Box, and R. C. Bales (2009), Higher surface mass balance of the Greenland
533 ice sheet revealed by high-resolution climate modeling, *Geophys. Res. Lett.*, *36*(12), doi:

Submitted for publication in *JGR-Earth Surface*. Not subject to U.S. copyright.

- 534 10.1029/2009GL038110.
- 535 Fausto, R. S., D. van As, J. E. Box, W. Colgan, P. L. Langen, and R. H. Mottram (2016),
536 The implication of nonradiative energy fluxes dominating Greenland ice sheet excep-
537 tional ablation area surface melt in 2012, *Geophys. Res. Lett.*, *43*(6), 2649–2658, doi:
538 10.1002/2016GL067720.
- 539 Fettweis, X., E. Hanna, C. Lang, A. Belleflamme, M. Erpicum, and H. Galle (2013), Important
540 role of the mid-tropospheric atmospheric circulation in the recent surface melt increase over
541 the Greenland ice sheet, *Cryosphere*, *7*(1), 241–248, doi:10.5194/tc-7-241-2013.
- 542 Fisher, D., J. Zheng, D. Burgess, C. Zdanowicz, C. Kinnard, M. Sharp, and J. Bourgeois
543 (2012), Recent melt rates of Canadian arctic ice caps are the highest in four millennia,
544 *Global Planet. Change*, *8485*, 3–7, doi:10.1016/j.gloplacha.2011.06.005.
- 545 Freitag, J., S. Kipfstuhl, T. Laepple, and F. Wilhelms (2013a), Impurity-controlled den-
546 sification: a new model for stratified polar firn, *J. Glaciol.*, *59*(218), 1163–1169, doi:
547 10.3189/2013JG13J042.
- 548 Freitag, J., S. Kipfstuhl, and T. Laepple (2013b), Core-scale radioscopic imaging: a new
549 method reveals densitycalcium link in Antarctic firn, *J. Glaciol.*, *59*(218), 1009–1014, doi:
550 10.3189/2013JG13J028.
- 551 Hall, D., J. E. Box, K. Casey, S. Hook, C. Shuman, and K. Steffen (2008), Comparison of
552 satellite-derived and in-situ observations of ice and snow surface temperatures over Green-
553 land, *Remote Sens. Environ.*, *112*(10), 3739–3749, doi:10.1016/j.rse.2008.05.007.
- 554 Hall, D. K., J. C. Comiso, N. E. DiGirolamo, C. A. Shuman, J. E. Box, and L. S. Koenig
555 (2013), Variability in the surface temperature and melt extent of the Greenland ice sheet
556 from MODIS, *Geophys. Res. Lett.*, *40*(10), 2114–2120, doi:10.1002/grl.50240.
- 557 Herron, M. M., and C. C. Langway (1980), Firn Densification: An Empirical Model, *J.*
558 *Glaciol.*, *25*(93), 373–385, doi:10.1017/S0022143000015239.
- 559 Hoerhold, M., T. Laepple, J. Freitag, M. Bigler, H. Fischer, and S. Kipfstuhl (2012), On the
560 impact of impurities on the densification of polar firn, *Earth Planet. Sci. Lett.*, *325326*, 93–
561 99, doi:10.1016/j.epsl.2011.12.022.
- 562 Hoerhold, M. W., S. Kipfstuhl, F. Wilhelms, J. Freitag, and A. Frenzel (2011),
563 The densification of layered polar firn, *J. Geophys. Res. Earth Surf.*, *116*(F1001), doi:
564 10.1029/2009JF001630.
- 565 Humphrey, N. F., J. T. Harper, and W. T. Pfeffer (2012), Thermal tracking of melt-
566 water retention in Greenland’s accumulation area, *J. Geophys. Res.*, *117*(F01010), doi:
567 10.1029/2011JF002083.
- 568 Laepple, T., M. Hoerhold, T. Muench, J. Freitag, A. Wegner, and S. Kipfstuhl (2016), Lay-
569 ering of surface snow and firn at Kohlen Station, Antarctica: Noise or seasonal signal?, *J.*
570 *Geophys. Res. Earth Surf.*, *121*(10), 1849–1860, doi:10.1002/2016JF003919.
- 571 Langway, C. C., and H. Shoji (1990), Past Temperature Record From The Analysis of
572 Melt Features In The Dye 3, Greenland, Ice Core, *Ann. Glaciol.*, *14*, 343–344, doi:
573 10.1017/S0260305500009095.
- 574 Libois, Q., G. Picard, L. Arnaud, S. Morin, and E. Brun (2014), Modeling the impact of
575 snow drift on the decameter-scale variability of snow properties on the Antarctic Plateau, *J.*
576 *Geophys. Res.*, *119*(20), 11,662–11,681, doi:10.1002/2014JD022361.
- 577 McGrath, D., W. Colgan, N. Bayou, A. Muto, and K. Steffen (2013), Recent warming at
578 Summit, Greenland: Global context and implications, *Geophys. Res. Lett.*, *40*(10), 2091–
579 2096, doi:10.1002/grl.50456.
- 580 McMillan, M., A. Leeson, A. Shepherd, K. Briggs, T. W. K. Armitage, A. Hogg,
581 P. Kuipers Munneke, M. van den Broeke, B. Nol, W. J. van de Berg, S. Ligtenberg, M. Hor-
582 wath, A. Groh, A. Muir, and L. Gilbert (2016), A high-resolution record of Greenland mass
583 balance: High-Resolution Greenland Mass Balance, *Geophys. Res. Lett.*, *43*(13), 7002–
584 7010, doi:10.1002/2016GL069666.
- 585 Muench, T., S. Kipfstuhl, J. Freitag, H. Meyer, and T. Laepple (2016), Regional climate signal
586 vs. local noise: a two-dimensional view of water isotopes in Antarctic firn at Kohlen Sta-
587 tion, Dronning Maud Land, *Clim. Past*, *12*(7), 1565–1581, doi:10.5194/cp-12-1565-2016.

Submitted for publication in *JGR-Earth Surface*. Not subject to U.S. copyright.

- 588 Nghiem, S. V., D. K. Hall, T. L. Mote, M. Tedesco, M. R. Albert, K. Keegan, C. A. Shuman,
589 N. E. DiGirolamo, and G. Neumann (2012), The extreme melt across the Greenland ice
590 sheet in 2012, *Geophys. Res. Lett.*, *39*(20), doi:10.1029/2012GL053611.
- 591 Nilsson, J., P. Vallelonga, S. B. Simonsen, L. S. Srensen, R. Forsberg, D. Dahl-Jensen,
592 M. Hirabayashi, K. Goto-Azuma, C. S. Hvidberg, H. A. Kjaer, and K. Satow (2015), Green-
593 land 2012 melt event effects on CryoSat-2 radar altimetry, *Geophys. Res. Lett.*, *42*(10),
594 3919–3926, doi:10.1002/2015GL063296.
- 595 Oerter, H., F. Wilhelms, F. Jung-Rothenhusler, F. Gktas, H. Miller, W. Graf, and S. Sommer
596 (2000), Accumulation rates in Dronning Maud Land, Antarctica, as revealed by dielectric-
597 profiling measurements of shallow firn cores, *Ann. Glaciol.*, *30*(1), 27–34.
- 598 Orsi, A. J., K. Kawamura, J. M. Fegyveresi, M. A. Headly, R. B. Alley, and J. P. Severinghaus
599 (2015), Differentiating bubble-free layers from melt layers in ice cores using noble gases,
600 *J. Glaciol.*, *61*(227), 585–594, doi:10.3189/2015JoG14J237.
- 601 Parry, V., P. Nienow, D. Mair, J. Scott, B. Hubbard, K. Steffen, and D. Wingham (2007),
602 Investigations of meltwater refreezing and density variations in the snowpack and firn within
603 the percolation zone of the Greenland ice sheet, *Ann. Glaciol.*, *46*(1), 61–68.
- 604 Pfeffer, W. T., and N. F. Humphrey (1996), Determination of timing and location of water
605 movement and ice-layer formation by temperature measurements in sub-freezing snow, *J.*
606 *Glaciol.*, *42*(141), 292–304, doi:10.1017/S0022143000004159.
- 607 Pfeffer, W. T., and N. F. Humphrey (1998), Formation of ice layers by infiltration and refreez-
608 ing of meltwater, *Ann. Glaciol.*, *26*, 83–91, doi:10.1017/S0260305500014610.
- 609 Pfeffer, W. T., T. H. Illangasekare, and M. F. Meier (1990), Analysis and Mod-
610 eling of Melt-Water Refreezing in Dry Snow, *J. Glaciol.*, *36*(123), 238–246, doi:
611 10.3189/S0022143000009497.
- 612 Picard, G., L. Brucker, A. Roy, F. Dupont, M. Fily, A. Royer, and C. Harlow (2013), Sim-
613 ulation of the microwave emission of multi-layered snowpacks using the Dense Media
614 Radiative transfer theory: the DMRT-ML model, *Geosci. Model Dev.*, *6*(4), 1061–1078,
615 doi:10.5194/gmd-6-1061-2013.
- 616 Proksch, M., H. Loewe, and M. Schneebeli (2015), Density, specific surface area, and cor-
617 relation length of snow measured by high-resolution penetrometry, *J. Geophys. Res. Earth*
618 *Surf.*, *120*(2), 346–362, doi:10.1002/2014JF003266.
- 619 Reijmer, C. H., and M. R. van den Broeke (2003), Temporal and spatial variability of the sur-
620 face mass balance in Dronning Maud Land, Antarctica, as derived from automatic weather
621 stations, *J. Glaciol.*, *49*(167), 512–520, doi:10.3189/172756503781830494.
- 622 Reijmer, C. H., M. R. van den Broeke, X. Fettweis, J. Ettema, and L. B. Stap (2012), Re-
623 freezing on the Greenland ice sheet: a comparison of parameterizations, *Cryosphere*, *6*(4),
624 743–762, doi:10.5194/tc-6-743-2012.
- 625 Rowe, C. M., M. R. Anderson, T. L. Mote, and K. C. Kuivinen (1995), Indications of melt in
626 near-surface ice-core stratigraphy: comparisons with passive-microwave melt signals over
627 the Greenland ice sheet, *Ann. Glaciol.*, *21*, 59–63, doi:10.1017/S0260305500015603.
- 628 Rutter, N., M. Sandells, C. Derksen, P. Toose, A. Royer, B. Montpetit, A. Langlois, J. Lem-
629 metyinen, and J. Pulliainen (2014), Snow stratigraphic heterogeneity within ground-based
630 passive microwave radiometer footprints: Implications for emission modeling, *J. Geophys.*
631 *Res. Earth Surf.*, *119*(3), 550–565, doi:10.1002/2013JF003017.
- 632 Schaller, C. F., J. Freitag, S. Kipfstuhl, T. Laepple, H. C. Steen-Larsen, and O. Eisen (2016), A
633 representative density profile of the North Greenland snowpack, *Cryosphere*, *10*(5), 1991–
634 2002, doi:10.5194/tc-10-1991-2016.
- 635 Schaller, C. F., J. Freitag, and O. Eisen (2017a), Critical porosity of gas enclosure in polar firn
636 independent of climate, *Clim. Past*, *13*(11), 1685–1693, doi:10.5194/cp-13-1685-2017.
- 637 Schaller, C. F., S. Kipfstuhl, H. C. Steen-Larsen, J. Freitag, and O. Eisen (2017b), Spatial
638 variability of density stratigraphy and melt features for two polar snowpacks in Greenland
639 and East Antarctica, *PANGAEA*, doi:10.1594/PANGAEA.884003.
- 640 Schwander, J., and B. Stauffer (1984), Age difference between polar ice and the air trapped in
641 its bubbles, *Nature*, *311*(5981), 45–47, doi:10.1038/311045a0.

Submitted for publication in *JGR-Earth Surface*. Not subject to U.S. copyright.

- 642 Severinghaus, J. P., A. Grachev, and M. Battle (2001), Thermal fractionation of air in polar
643 firn by seasonal temperature gradients, *Geochem. Geophys.*, *2*(7).
- 644 Shepherd, A., E. R. Ivins, G. A. V. R. Barletta, M. J. Bentley, S. Bettadpur, K. H. Briggs,
645 D. H. Bromwich, R. Forsberg, N. Galin, M. Horwath, S. Jacobs, I. Joughin, M. A. King,
646 J. T. M. Lenaerts, J. Li, S. R. M. Ligtenberg, A. Luckman, S. B. Luthcke, M. McMillan,
647 R. Meister, G. Milne, J. Mouginot, A. Muir, J. P. Nicolas, J. Paden, A. J. Payne, H. Pritchard,
648 E. Rignot, H. Rott, L. S. Sorensen, T. A. Scambos, B. Scheuchl, E. J. O. Schrama, B. Smith,
649 A. V. Sundal, J. H. van Angelen, W. J. van de Berg, M. R. van den Broeke, D. G. Vaughan,
650 I. Velicogna, J. Wahr, P. L. Whitehouse, D. J. Wingham, D. Yi, D. Young, and H. J. Zwally
651 (2012), A Reconciled Estimate of Ice-Sheet Mass Balance, *Science*, *338*(6111), 1183–1189,
652 doi:10.1126/science.1228102.
- 653 Steffen, K., J. E. Box, and W. Abdalati (1996), Greenland Climate Network: GC-Net, in
654 *Glaciers, Ice Sheets and Volcanoes: A Tribute to Mark F. Meier*, edited by S. C. Colbeck,
655 pp. 98–103, US Army Cold Regions Research and Engineering Laboratory, Hanover, NH.
- 656 Stroeve, J. C., J. E. Box, and T. Haran (2006), Evaluation of the MODIS (MOD10a1) daily
657 snow albedo product over the Greenland ice sheet, *Remote Sens. Environ.*, *105*(2), 155–171,
658 doi:10.1016/j.rse.2006.06.009.
- 659 Tedesco, M. (2007), Snowmelt detection over the Greenland ice sheet from SSM/I brightness
660 temperature daily variations, *Geophys. Res. Lett.*, *34*(2), doi:10.1029/2006GL028466.
- 661 Tedesco, M., X. Fettweis, T. Mote, J. Wahr, P. Alexander, J. E. Box, and B. Wouters (2013),
662 Evidence and analysis of 2012 Greenland records from spaceborne observations, a regional
663 climate model and reanalysis data, *Cryosphere*, *7*(2), 615–630, doi:10.5194/tc-7-615-2013.
- 664 Vallelonga, P., K. Christianson, R. B. Alley, S. Anandakrishnan, J. E. M. Christian, D. Dahl-
665 Jensen, V. Gkinis, C. Holme, R. W. Jacobel, N. B. Karlsson, B. A. Keisling, S. Kipfstuhl,
666 H. A. Kjr, M. E. L. Kristensen, A. Muto, L. E. Peters, T. Popp, K. L. Riverman, A. M.
667 Svensson, C. Tibuleac, B. M. Vinther, Y. Weng, and M. Winstrup (2014), Initial results from
668 geophysical surveys and shallow coring of the Northeast Greenland Ice Stream (NEGIS),
669 *Cryosphere*, *8*(4), 1275–1287, doi:10.5194/tc-8-1275-2014.
- 670 van den Broeke, M., J. Bamber, J. Ettema, E. Rignot, E. Schrama, W. J. van de Berg, E. van
671 Meijgaard, I. Velicogna, and B. Wouters (2009), Partitioning Recent Greenland Mass Loss,
672 *Science*, *326*(5955), 984–986, doi:10.1126/science.1178176.
- 673 Wichert, S., K. Fokianos, and K. Strimmer (2004), Identifying periodically ex-
674 pressed transcripts in microarray time series data, *Bioinformatics*, *20*(1), 5–20, doi:
675 10.1093/bioinformatics/btg364.